



TECHNISCHE UNIVERSITÄT MÜNCHEN

Lehrstuhl für Technische Chemie II

Hydrogenation of model aromatic compounds on supported Ni-MoS₂ and Ni-WS₂ catalysts

Wanqiu Luo

Vollständiger Abdruck der von der Fakultät für Chemie der Technischen Universität München zur Erlangung des akademischen Grades eines

Doktors der Naturwissenschaften (Dr. rer. nat.)

genehmigten Dissertation.

Vorsitzender: Prof. Dr. Klaus Köhler

Prüfer der Dissertation: 1. Prof. Dr. Johannes A. Lercher

2. Prof. Dr. Roland A. Fischer

Die Dissertation wurde am 09.01.2019 bei der Technischen Universität München eingereicht und durch die Fakultät für Chemie am 18.02.2019 angenommen.

*"Life need not be easy,
provided only that it is not empty."*

Lise Meitner (1878 - 1968)

Acknowledgement

It has been a long and tough journey into the world of sulfide catalysts, and now I am close to the end of it. Many lovely people provided me countless support and encouragement along the way, only then can I finally walk it through. Therefore, I would like to take the opportunity to thank to some of them, although I realize that words could not convey all of my appreciation.

First and foremost, I owe my sincere gratitude to Prof. Dr. Johannes A. Lercher for providing me the opportunity to work in his international group, as well as for leading me into a challenging research topic. Johannes, thank you for your guidance, patience, insights, and for granting me the freedom in research. I have been always inspired by your passion for science, your perfectionism and expertise in research, and also your humor and wisdom in life. I can still recall how you encouraged me to explore the recreation area in California and to seize every single opportunity to experience the world. It turned out to be terrific for me, both the trip and my thesis under your guidance, which I deeply appreciate.

My sincere thanks further go to our industrial partner, Chevron Energy Technology Company, for the financial support and for inviting us to visit their site in San Francisco. In particular I want to mention our project partners, Dr. Alex Kuperman and Dr. Axel Brait. It was always a pleasure to join the project meeting and to share ideas with you, because of your input and your helpful suggestions.

Special gratitude I owe to my first supervisor, Dr. Oliver Y. Gutiérrez. I enjoyed the time working you in the first two years of my thesis, because you were so passionate and productive in scientific work. Thank you for guiding me, from the beginning of my thesis, to the right direction, for listening to me for all my troubles, and for teaching me how to be independent and confident. I still remember and treasure those days, sitting together with you for preparation of my first project meeting, group meeting, and conference talk, which was worth more than tons of tequila for me.

I am as well grateful to my second supervisor, Dr. Hui Shi, who has been taking over the responsibility for the sulfide team and has guided us to a new direction during last two years. It is always a pleasure to discuss experimental problems with you, to be impressed by your intelligence and scientific insights, and to recognize then delightfully admit my own ignorance. I could not accomplish this thesis so fast without your continuous support in writing and polishing my manuscripts. Thank you for all what you have

Acknowledgement

done for the whole sulfide team.

Now, I want to thank all of my colleagues at TCII. First of all, I would like to thank Prof. Dr. A. Jentys, Dr. Yue Liu for all the scientific suggestions. Many thanks to Xaver Hecht for saving me from enormous amount of troubles in the lab, to Martin Neumann for AAS measurement and to Andreas Marx for all the technical problems. Stefanie, Bettina, Uli and Kateryna, thank you for your kind helps in administration issue. I owe our sulfide team special gratitude: Dr. Eva Schachtl, Ferdinand Vogelgsang, Manual Wagenhofer, Manual Weber, Roland Weindl, Dr. Wenhao Luo and Dr. Lei Zhong. Thanks for creating such a nice atmosphere in the lab, including all the sulfur smells which indeed I would miss in the future. I felt really blessed to have Ferdi always backing me up for the reactor and Manual repairing every setup and the coffee machine. Thank you for sharing the knowledge about sulfides, as well as all the ups and downs in the lab. I would also like to mention my office mates, Dr. Moritz Schreiber, Dr. Jiayue He, Dr. Kai Sanwald, Dr. Bo Peng, Dr. Wenji Song, Ruixue and Dr. Ricardo Bermejo de Val. I enjoyed our talks and discussions, no matter scientific or non-scientific. I am very grateful to the other members of TCII group, Dr. Sebastian Grundner, Dr. Yu Lou, Dr. Guoju Yang, Dr. Yang Song, Dr. Yuanshuai Liu, Dr. Stanislav Kasakov, Dr. Erika Ember, Dr. Maricruz Sanchez-Sanchez, Dr. Ezter Baráth, Takaaki, Hui, Xi, Guanhua, Lingli, Andi, Edith, Christoph, Daniel, Verena, and other members who are not mentioned here, for their help and the great time we have shared in TCII.

Very special thanks go to my partner, Yilin, whom we call Dr. Li later. Thank you for your accompany and unconditional support during all these years in Munich, without which I might have already been lost. And last but not least, I want to thank my family. Mammy and Daddy, thank you for your understanding throughout my studies, from primary school till now. You've always been so proud of me, but indeed, all your love and sacrifice made up the best thing in my life.

Wanqiu

Garching, December 2018

Abbreviations

AAS	Atomic absorption spectroscopy
Al ₂ O ₃	Aluminium oxide, alumina
API gravity	The American Petroleum Institute gravity
ASA	Amorphous silica alumina
<i>asym</i> OHPhe	1,2,3,4,4a,9,10,10a-octahydrophenanthrene
BAS	Brønsted acid sites
BET	Brunauer-Emmett-Teller
CO	Carbon monoxide
DBT	Dibenzothiophene
DDS	Direct desulfurization
DFT	Density functional theory
DiHPhe	9,10-dihydrophenanthrene
4,6-DMDBT	4,6-dimethyldibenzothiophene
DMP	2,6-dimethylpyridine
E _g	Band gap
EXAFS	Extended x-ray absorption fine structure
f _m or f _w or f _m	Fraction of metal atoms(W or Mo) on the edge
FCC	Fluid catalytic cracking
FT-IR	Fourier-transform infrared spectroscopy
GC	Gas chromatography
HC	Hydrocarbon
H/C	Hydrogen-to-carbon
HDA	Hydrodearomatization
HDM	Hydrodemetallization
HDN	Hydrodenitrogenation
HDO	Hydrodeoxygenation
HDS	Hydrodesulfurization

Abbreviations

HYD	Hydrogenation
IR	Infrared
k_i	Reaction rate constant
K_c	Equilibrium concentration ratio
K_{eq}	Equilibrium constant
K_i	Adsorption constant
LAS	Lewis acid sites
L-H	Langmuir-Hinshelwood
LPG	Liquefied petroleum gas
MS	Mass spectrometry
N	Coordination number
Ni/(Me)	Molar ratio of Ni/(Ni+W+Mo)
NO	Nitric oxide
O_h	Octahedral coordination
PAH	Polycyclic aromatic hydrocarbon
PHE	Phenanthrene
PMs	Particulate matters
r_i	Reaction rate
rds	Rate determining step
SH	Sulfhydryl groups
STEM	Scanning transmission electron microscopy
STM	Scanning tunneling microscopy
<i>sym</i> OHPhe	1,2,3,4,5,6,7,8-octahydrophenanthrene
TEM	Transmission electron microscopy
TetHPhe	1,2,3,4-tetrahydrophenanthrene
T_{ex}	S-O exchange temperature
TMS	Transition metal sulfides
TOF	Turnover frequency
TPS	Temperature programmed sulfidation

Abbreviations

T _{red}	Reduction temperature
USY	Ultra-stable Y zeolite
UV-Vis DR	Ultraviolet-visible diffuse reflectance
vdW	Van der Waals
VGO	Vacuum gas oil
Vol.-%	Volume percentage
wt.-%	Weight percentage
XANES	X-ray absorption near edge structure
XAS	X-ray absorption spectroscopy
XRD	X-ray diffraction

Abstract

The rate of phenanthrene hydrogenation on Ni-Mo(W)S₂/Al₂O₃ is linearly correlated to the concentration of sulfhydryl (SH) groups vicinal to edge-decorated Ni. SH groups close to Mo and W show a much lower activity. The higher activity of Ni-WS₂ arises from a higher tendency of accessible Ni to stabilize more SH groups, compared to Ni-MoS₂. Removal of NiS_x clusters increases the activity of Ni-WS₂ by up to 5 times. This is attributed to a higher concentration of accessible Ni as well as SH groups.

Zusammenfassung

Die Rate der Phenanthrenhydrierung auf Ni-Mo(W)S₂/Al₂O₃ ist linear korreliert mit der Konzentration der Sulfhydryl(SH)-Gruppen, die vizinal zu kantendekorierendem Ni liegen. Sulfhydryl-Gruppen in der Nähe von Mo und W zeigen eine viel geringere Aktivität. Die höhere Aktivität von Ni-WS₂ ergibt sich aus einer höheren Tendenz zu zugänglichem Ni, das selbst auch mehr SH-Gruppen stabilisiert, als Ni-MoS₂. Das Entfernen von NiS_x-Clustern erhöht die Aktivität von Ni-WS₂ um das bis zu 5-fache. Dies ist auf eine höhere Konzentration an zugänglichem Ni und an SH-Gruppen zurückzuführen.

Table of Contents

Acknowledgement	i
Abbreviations	iii
Abstract	vi
Table Of Contents	vii
Chapter 1 Introduction	1
1.1 From Petroleum to Commercial Fuels: Hydrotreating Process	1
1.1.1 Crude Oil: Demands and Challenges	1
1.1.2 Hydrotreating Process	4
1.1.3 Hydrodesulfurization	5
1.1.4 Hydrodenitrogenation	8
1.1.5 Hydrodearomatization	9
1.2 Transition Metal Sulfides	12
1.2.1 Structure of Mo(W)S ₂	12
1.2.2 Proposed Models for Co Or Ni Promoted Mo(W)S ₂	13
1.2.3 Supported Catalysts and the Support Effect	16
1.2.4 Role Of Ni _x On Ni-Mo(W)S ₂ Catalysts	17
1.3 Scope Of The Thesis	17
1.4 References	19
Chapter 2 Active sites on Ni-promoted transition metal sulfides that catalyze aromatics hydrogenation	31
2.1 Introduction	32
2.2 Experimental Section	33
2.2.1 Catalysts Preparation	33
2.2.2 Characterization of Catalysts	34
2.2.3 Kinetic Measurements	36
2.3 Results and Discussion	37
2.4 Conclusion	44
2.5 References	45
2.6 Supporting Information	48
2.6.1 Characterization Results of the Oxide Precursors	48
2.6.2 Effects of the W-Ni Interactions on the Sulfidation of Oxide Precursors	52
2.6.3 Kinetic Data for Hydrogenation of Phenanthrene	54
2.6.4 Structural Characterization of WS ₂ -based Catalysts	57
2.6.4.1 XRD, TEM and Raman	57

Table of Contents

2.6.4.2 Adsorption of NO	60
2.6.5 Determination of Surface Brønsted and Lewis Acid Sites.....	63
2.6.5.1 DMP Adsorption Probed by IR Spectroscopy.....	63
2.6.5.2 Lewis Acid Sites Probed by Pyridine Adsorption.....	66
2.6.6 Estimation of Molar Extinction Coefficients and the Fraction of Ni at Slab Edges.....	68
2.7 Reference for Supporting Information	70
2.8 Associated Content	73
Chapter 3 Maximizing active site concentrations at Ni-substituted WS ₂ -edges for hydrogenation of polyaromatic	74
3.1 Introduction	75
3.2 Experimental Section	76
3.2.1 Catalysts Preparation.....	76
3.2.2 Catalysts Characterization	77
3.2.3 Kinetic Measurements.....	78
3.3 Results and Discussion.....	79
3.3.1 Textual Properties of Acid-Treated Sulfide Materials.....	79
3.3.2 CO-IR and NO-IR Spectra on Acid-Treated Materials and Chlorinated-Al ₂ O ₃ -Supported Ni-WS ₂	80
3.3.3 Characterization of Acid Sites on the Sulfide Materials.....	83
3.3.4 Hydrogenation of Phenanthrene over Leached and Chlorided-Al ₂ O ₃ Supported Ni-WS ₂	85
3.3.5 Effects from γ -Al ₂ O ₃ And Cl-Al ₂ O ₃ Supports.....	87
3.3.6 Effect of the Acid Treatment on Metal Sulfide Phase.....	88
3.4 Conclusion	89
3.5 Reference.....	90
3.6 Supporting Information.....	95
3.6.1 Elemental Analysis and Textual Properties of Parent Sulfides and Leached Sulfides	95
3.6.2 CO Adsorption on Parent and Leached Sulfides.....	98
3.6.3 NO Adsorption on Leached WS ₂ and Ni-Promoted WS ₂	101
3.6.4 DMP-H ₂ and Pyridine Adsorption Probed by IR Spectroscopy	103
3.6.5 Hydrogenation of Phenanthrene	107
3.7 References for Supporting Information	112
3.8 Associated Content	114
Chapter 4 Summary and Conclusions.....	115
List of Publications.....	119

Chapter 1

Introduction

1.1 From Petroleum to Commercial Fuels: Hydrotreating Process

1.1.1 Crude Oil: Demands and Challenges

Fossil fuels, including oil, coal and natural gas, have been representing the leading energy source in the world. In 2017, Oil remained as the world’s dominant fuel, accounting for roughly a third of global energy consumption (Figure 1.1).¹ Even though renewable power grew significantly by 69 million tonnes of oil equivalent (mtoe) in one year, oil still provided significant increment by 65 mtoe, to which China and US majorly contributed.¹

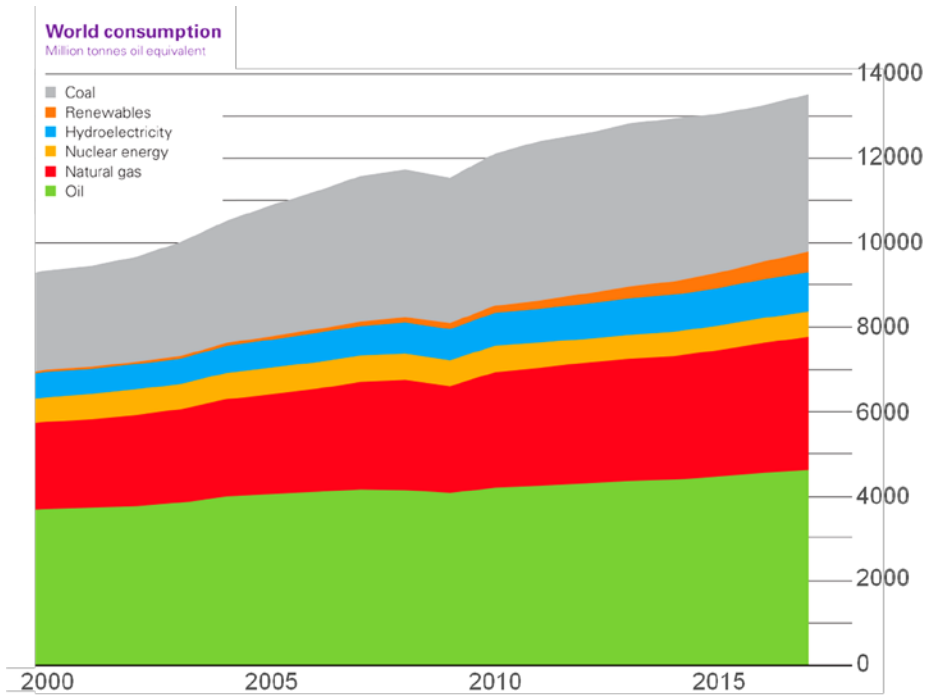


Figure 1.1. World consumption Million tonnes oil equivalent, graph adapted from ref.¹

The demand for petroleum products has been continuously increasing, while the quality of the crude oil reserves has been declining even since early 1960s.² Crude oil is a mixture of liquid hydrocarbons with considerable heteroatoms in the constituents, which contribute to a large variety of complex molecular structures and can differ significantly depending on its origin or geographical location of the refinery (Table 1.1).^{3–5} The main compositions can be further classified as asphaltene, resin, aromatic and saturate, of which the average elemental composition is analyzed as C (79.5-87.1%), H (11.5-14.8%), S (0.1-3.5%), N (0.1-2%) and O (0.1-0.5%) with a few trace metals (mostly V and Ni).^{6–9} Consequently, its physical properties (e.g., volatility, specific gravity, ignition point and viscosity) also vary widely. The specific gravity, i.e., the ratio of the weight of a crude oil and water per volume at standard conditions, is considered to be most important. API gravity is applied to evaluate the specific gravity, in which crude oils can be classified as heavy (10–20° API gravity), medium (20–25° API gravity), and light (above 25° API gravity).⁸

Table 1.1. Variations in the physical properties and compositions of different crude oils⁵

Origin	Specific gravity (water=1)	Approximate physical composition, %			
		Gasoline and gas	Kerosene	Gas oil	Residues(1000°F+)
California	0.858	36.6	4.4	3.6	23.0
Pennsylvania	0.800	47.4	17.0	14.3	1.3
Iraq	0.844	45.3	15.7	15.2	23.8
Iran	0.836	45.1	11.5	22.6	20.8
Kuwait	0.860	39.2	8.3	20.6	31.9
Bahrain	0.861	26.1	13.4	34.1	26.4
Saudi Arabia	0.840	34.5	8.7	29.3	27.5
Venezuela	0.950	15.4	7.4	77.3	-

The light and medium oils are the so-called “conventional oil”, as they are lighter and less dense with high percentage of hydrocarbons. Conventional oil is much more profitable as a fuel source, owing to the smallest amount of processing that it requires to create value-added products. On the contrary, the heavy and extra-heavy crude oils are classified into “unconventional oil”, and they are more expensive to process into commercial fuels because the containing hydrocarbons are less flammable with higher percentages of sulfur and nitrogen (Table 1.2).

Table 1.2. Typical elemental composition for heavy oil from Venezuela reserve¹⁰

Fraction	Weight percentage, %	Elementary composition based on C ₂₀ ⁺ fraction, wt. %				
		C	H	N	O	S
Asphaltene	14.1	83.8	7.5	1.3	1.7	4.8
Resin	37.3	82.8	8.9	1.5	2.0	4.3
Aromatic	37.2	84.3	10.0	<0.3	1.1	4.0
Saturate	11.4	86.6	13.0	<0.3	<0.2	<0.1

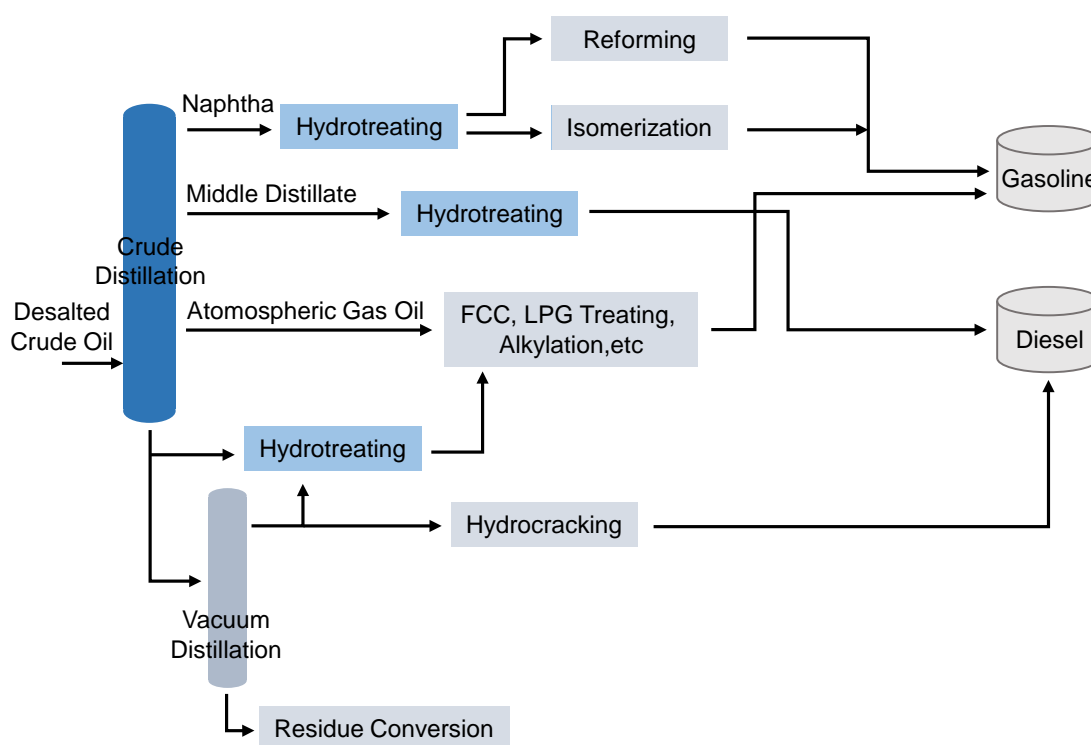
Unfortunately, the world's reserves of conventional oil have been dramatically depleted, and there are rarely new discoveries of those reserves such that it is increasingly more difficult to meet the increment in energy demand. The gap between reserves and demand requires the oil industry to exploit the unconventional reserves. To accomplish the transformation from heavy oil into gasoline, it must be refined, cracked to smaller hydrocarbons, and hydrotreated to remove heteroatoms, all of which demand high energy input.¹¹

The exploitation of heavy crude oil has significant environmental drawbacks, which raises many concerns and leads to stringent regulations for heavy crude oil. For one, crude oil and crude oil-derived chemicals are environmental pollutants, especially sulfur containing compounds (Table 1.2) which are responsible for acid rain.^{6,12,13} Sulfur, nitrogen, and heavy metals must be removed before converting the heavy oil fractions into lighter products, because they are potent poisons for catalytic refining processes.^{14–17} Another environmental impact is a much higher CO₂ emission (up to 3 times). Higher energy input is required to generate the same quantity of products compared to lighter crude hence the greater CO₂ emission. In addition, heavy crude has a lower H/C ratio than light crude, which means that when it is burned, more CO₂ is released.

Despite these environmental impacts, it is still inevitable to shift to heavy crude oil as the dominating energy source for the next decades and, therefore, the message is clear. The long-lasting challenge is, for the research institutes and refineries, to develop better scientific and technological concepts about hydrotreating catalysts and processes so as to achieve efficient and economical usage of crude oil with minimal environmental footprint.

1.1.2 Hydrotreating Process

In order to produce products with higher value from crude oil, the oil refinery applies different physical and chemical processes to different feedstock streams, for example distillation, extraction, reforming, isomerization, aromatization, alkylation, hydrogenation, cracking, blending, and hydrotreating (Scheme 1.1).⁹ The term hydroprocessing or hydroconversion processes, is the combination of hydrotreating and hydrocracking processes. Some of these processes are non-catalytic like hydrovisbreaking, but catalytic hydroprocessing plays a more important role in the conversion of heavy oil into cleaner automotive fuels. Depending on the distinct process, typical reaction conditions for hydrotreating are 300-400 °C and total pressures up to 15 MPa (Figure 1.2).^{5,9}



Scheme 1.1. Process flow from crude oil to final products involving hydrotreating, graph adapted from ref.¹⁸

In refinery, hydrotreating is mainly applied to obtain cleaner burning fuels, thus avoiding the poisoning of catalysts placed downstream and reducing air pollution. During hydrotreating, several classes of reactions occur simultaneously in the presence of catalysts (e.g., supported or self-supported CoMoS_2 , NiMoS_2 , or NiWS_2) and H_2 , such as hydrogenation, hydrodearomatization (HDA), removal of S by hydrodesulfurization (HDS), removal of N by hydrodenitrogenation (HDN), removal of O by hydrodeoxygenation (HDO), and hydrodemetallization (HDM) from different petroleum streams.⁹

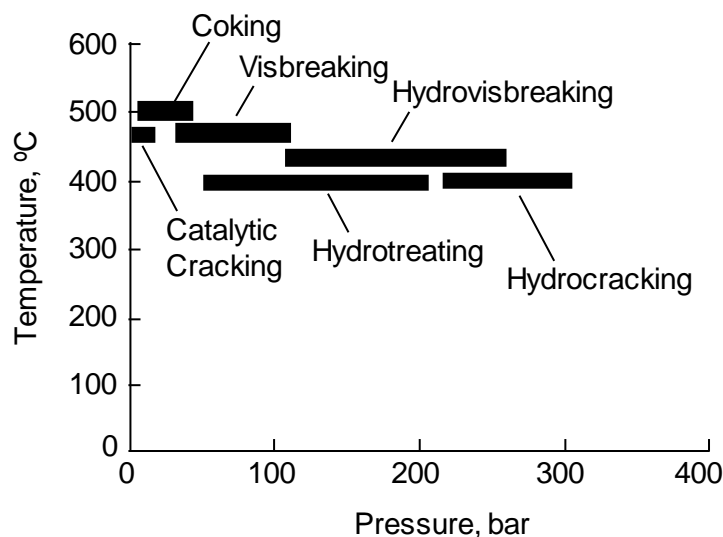


Figure 1.2. Temperature and pressure parameters for various process.⁵ Republished with permission of TAYLOR & FRANCIS GROUP LLC - BOOKS, from Petroleum refining processes, Speight James and Ozum Baki, 2001; permission conveyed through Copyright Clearance Center, Inc.

1.1.3 Hydrodesulfurization

In 2012, the EU transport sector demanded up to 70% of total diesel fuel to be consumed in the whole European Union (2.5 Mt),¹⁹ and concomitant exhaust emissions are important sources of environment pollution.²⁰⁻²² Figure 1.3 is a pie chart showing the typical emission of a diesel engine, where N₂ is the dominant part (67%) and CO₂ contributes to 12% in the total emission. Pollutant gases combine for 1%, including CO, hydrocarbons, NO_x, SO₂ and particulate matters (PMs),²³ which could lead to respiratory disease, neurodegenerative disorders and cancer.^{24,25} Nitrogen removal by HDN is required to maintain NO_x emissions below regulatory levels, while sulfur removal by HDS can ultimately reduce the SO₂ emissions.

HDS process could be simplistically described as follows: H₂ is added to organosulfur compounds over certain catalysts at high temperatures and pressures, releasing the sulfur as H₂S. However, the reactivity of the organosulfur compounds depends largely on the molecular structure.²⁶⁻²⁸ The most abundant classes of organosulfur compounds are benzothiophenes (BTs) and dibenzothiophenes (DBTs). Sulfur can be relatively easily removed from BTs, whereas DBTs (called refractory S-compounds) with alkyl groups at position 4 or/and 6 demand significantly harsher reaction conditions (Figure 1.4).

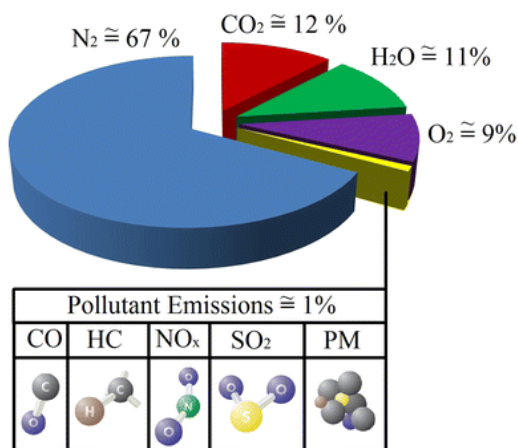


Figure 1.3. The typical emission of a diesel engine.²³ Republished with permission of Springer Science and Bus Media B V, from The pollutant emissions from diesel-engine vehicles and exhaust after treatment systems, Reşitoğlu, İbrahim Aslan; Kemal Altinişik; Ali Keskin, 17, 1, 2015; permission conveyed through Copyright Clearance Center, Inc.

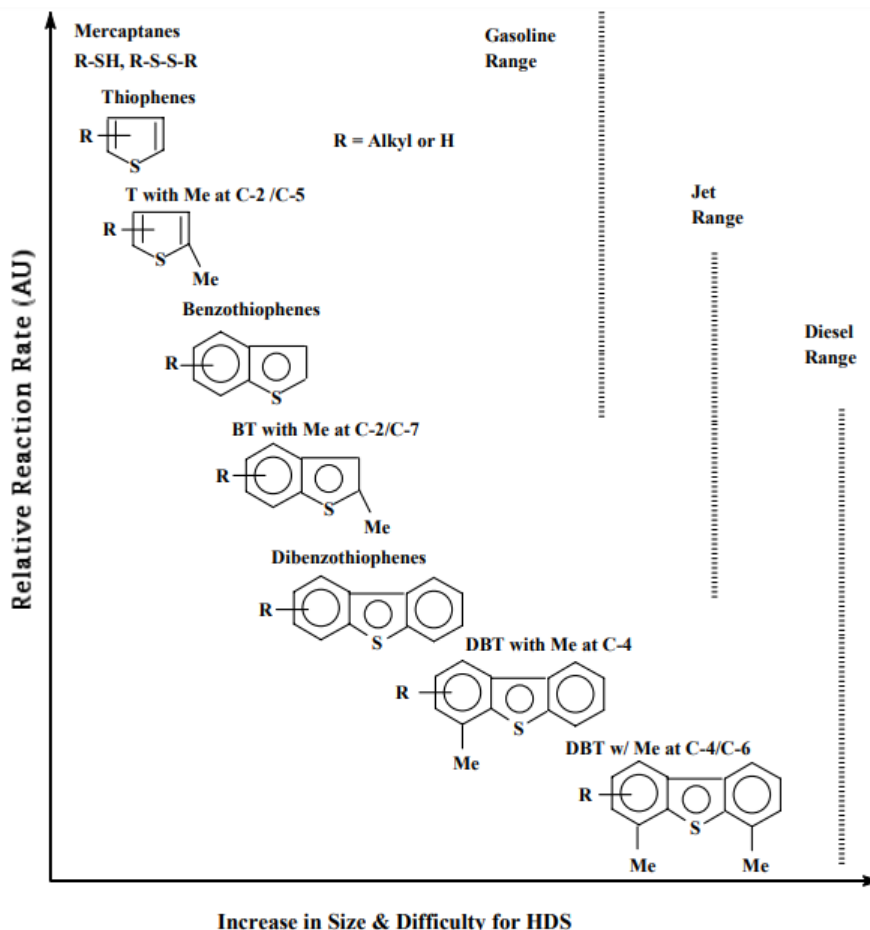
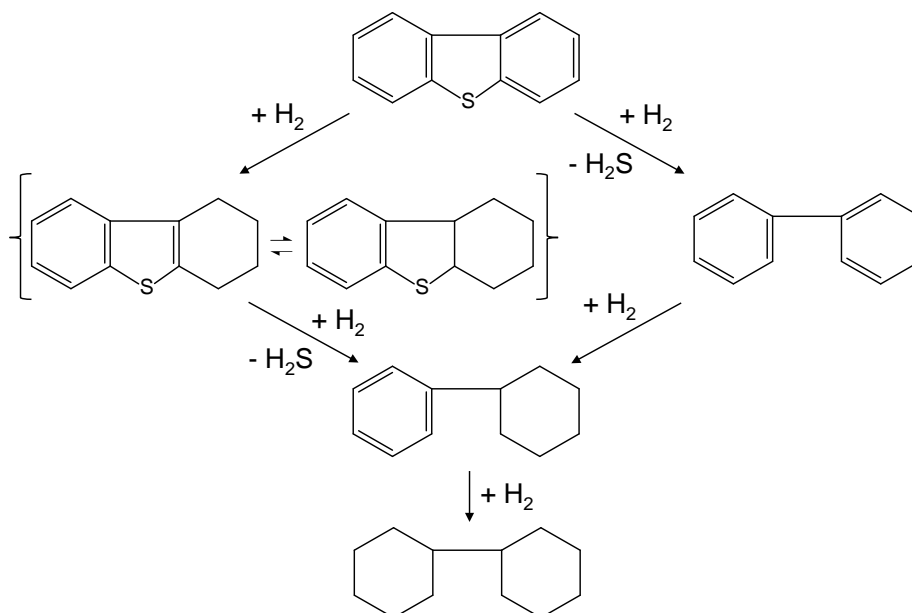


Figure 1.4. Reactivities of various organic sulfur compounds in HDS.^{29,30} Republished with permission of Elsevier Science and Technology Journals, from An overview of new approaches to deep desulfurization for ultra-clean gasoline, diesel fuel and jet fuel, Chunshan Song, 86, 1-4, 2003; permission conveyed through Copyright Clearance Center, Inc.

Even though the individual activity and selectivity depends on several parameters (e.g., temperature, substrate, catalyst, and $\text{H}_2\text{S}/\text{H}_2$ ratio), similar elementary steps can be used to describe the reaction network of the HDS: adsorption of the substrate onto the active site with S-coordination, activation of hydrogen on the catalyst by dissociative adsorption, cleavage of the C–S bonds, hydrogenation of unsaturated C=C bonds, addition of hydrogen to the broken bond at both S- and C- ends, and release of the hydrocarbon product as well as H_2S from the active site.

For example, the HDS of dibenzothiophene consists of two routes: the DDS and the HYD pathway (Figure 1.4). The DDS pathway (hydrogenolysis) produces cyclohexylbenzene,³¹ where S atom is removed without hydrogenating the aromatic rings. On the other hand, HYD is to hydrogenate one aromatic ring followed by extraction of the S atom. The ratio between DDS and HYD depends on the molecule structure, types of catalysts and actual reaction conditions. In the case of dibenzothiophene, DDS route is typically favored on transition metal sulfide catalysts. But when there are alkyl substituents at the carbon atoms adjacent to the sulfur atom, e.g., 4,6-dimethyldibenzothiophene (4,6-DMDBT), the rate of DDS is dramatically inhibited whereas the rate of HYD is relatively unaffected.^{26,31–33} The main reason is that for DDS the S atom usually adsorbs at coordinatively unsaturated sites at the edges of the catalyst, while steric hindrance due to the presence of alkyl substituents retards this adsorption,^{33,34} which increases with increasing size of the alkyl groups (from methyl to ethyl to propyl).



Scheme 1.2. Reaction mechanism for HDS of dibenzothiophene.³⁵

HDS is important for all countries to obtain ultra-low sulfur content in gasoline and diesel fuels, which is the fundamental prerequisite for the efficient operation of exhaust after

treatment devices in vehicles, e.g., diesel particulate filter, lean NO_x trap, and selective catalytic reduction. In this context, the sulfur content of gasoline and diesel fuels in Europe has therefore been regulated to 50 ppm by 2005, while Europe began the phase-in of virtually sulfur-free gasoline and diesel fuels (<10 ppm sulfur), until 2009.²⁶ Consequently, the required reduction in sulfur have compelled refineries to devote more resources into improving the processes and developing more active catalysts.

1.1.4 Hydrodenitrogenation

Catalytic hydrodenitrogenation (HDN) occurs simultaneously with HDS during hydroprocessing, in which organonitrogen compounds are removed from feedstocks with the presence of H₂ to produce processible and stable liquid fuels.³⁶ The N-containing molecules, as the second most abundant impurity in crude oil, inhibit HDS and other reactions because of their preferential adsorption on catalytic sites,³⁷ and they also affect the stability of fuels.

Two types of organonitrogen compounds, i.e. heterocyclic or non-heterocyclic, are mainly found in petroleum. The latter type comprises aliphatic amines and anilines which undergo HDN rapidly. Heterocyclic nitrogen compounds, in comparison, are more difficult to react,^{38,39} and they consist of six-membered pyridinic ring (basic N-compounds) or five-membered pyrrolic ring (non-basic N-compounds).⁴⁰ The typical N-ring structures are shown in Figure 1.5.

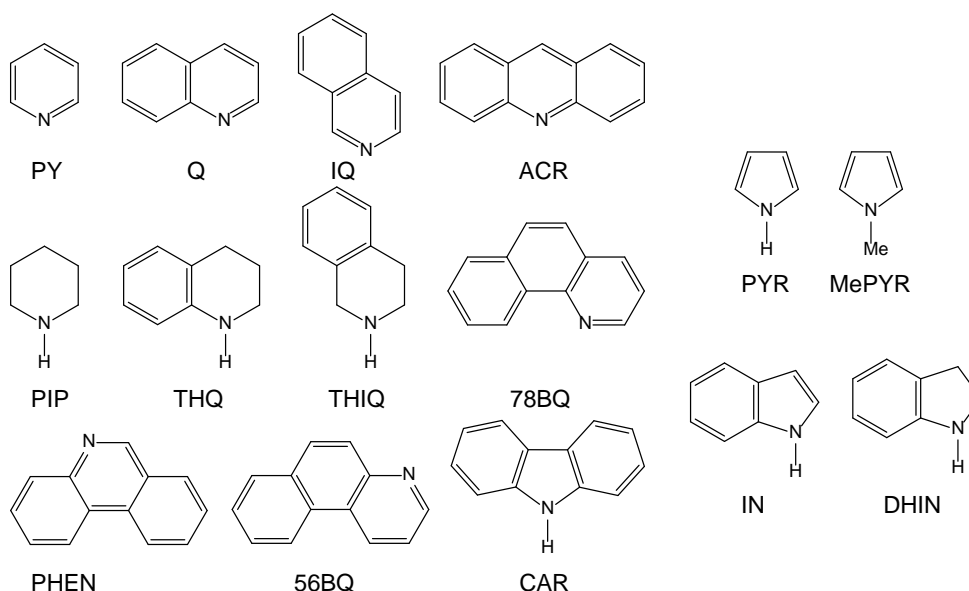


Figure 1.5. Model N-heterocyclic substrates subjected to HDN reactions⁴¹

Hydrogenation of the N-ring and hydrogenolysis of the C-N bond are the essential reactions occurring during HDN, before the final release of NH₃ to yield the N-free hydro

carbons. Some of the observations made during the HDN of amines, as the final intermediates of the overall HDN, can be interpreted in terms of the classical Hoffmann elimination and nucleophilic substitution.^{33,42–46}

Comparable to HDS, the overall HDN conversions depend on the reactivity of N-compounds. Important parameters influencing HDN include alkyl substitution, particularly in the N-ring, temperature, H₂ pressure, contact time, type of catalyst, H₂S/H₂ ratio, etc.^{36,47}

1.1.5 Hydrodearomatization

In a diesel fuel, it is more favorable to have straight-chain hydrocarbon molecules with a minimum amount of aromatic and side-chain hydrocarbon molecules, due to the fact that high aromatic content in diesel fuel can lower the cetane index in the fuel and contributes significantly to the formation of undesired emissions in exhaust gases.^{48–50} Consequently, Europe has already tightened the aromatics specifications prior to Euro-4 standard, requiring a minimum cetane index of 51 as well as limiting the aromatic content to as low as 5 vol.%.^{50–52}

Despite the environmental and legislative aspects, aromatics hydrogenation is inevitable in refinery industry.^{53–56} The HYD of aromatic hydrocarbons and alkenes is also part of the overall HDS or HDN chemistry, particularly at high conversion levels where hydrogenation of aromatic rings is approaching thermodynamic equilibrium, preventing the reaction steps in HDS or HDN from attaining full conversions.⁵⁷ Therefore, it is essential to understand the kinetic, thermodynamic and mechanistic aspects of aromatic hydrogenation reactions over typical hydrotreating catalysts.

Aromatics found in petroleum and synthetic middle distillates mainly fall into four groups: monoaromatics, diaromatics, triaromatics, and polycyclic aromatics.^{58–62} The composition of the aromatics fraction depends largely on the origin of the feedstock, and their hydrogenation reactivities are considerably different. Typical aromatic compounds present in untreated gas oil fractions are shown in Table 1.3.

Aromatic hydrogenation is usually a reversible reaction which can be catalyzed by a variety of heterogeneous catalysts. For the reactions are catalyzed by transition metal sulfides,^{63–65} severe conditions, such as high temperatures and pressures as well as low space velocities, are needed to achieve acceptable conversions. It is highly exothermic with heats of reaction in the range of 63-71 kJ per mole of H₂,^{66,67} therefore, higher temperatures lead to lower equilibrium concentrations of more saturated compounds (Table 1.4). In addition, high pressures are always needed to shift the equilibrium to higher conversion of aromatics.^{50,51,57}

Table 1.3. Typical Structure of Aromatics in Petroleum Fraction⁵¹

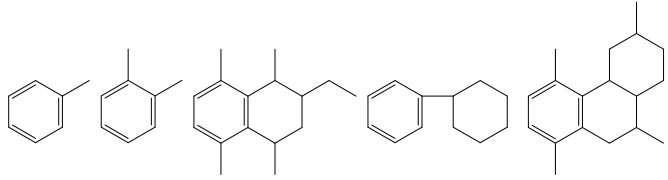
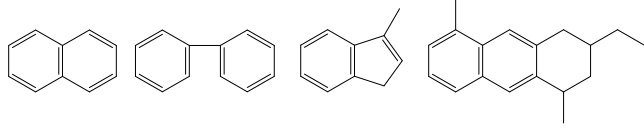
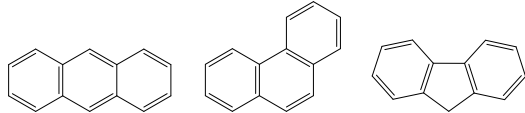
Aromatic Compound Type	Typical structure
2.1 Monoaromatics (Alkyl benzenes, benzocycloparaffins, and benzodicycloparaffins)	
2.2 Diaromatics (Naphthalenes, biphenyls, indenenes, and naphthocycloparaffins)	
2.3 Triaromatics (Anthracenes, phenanthrenes, and fluorenes)	

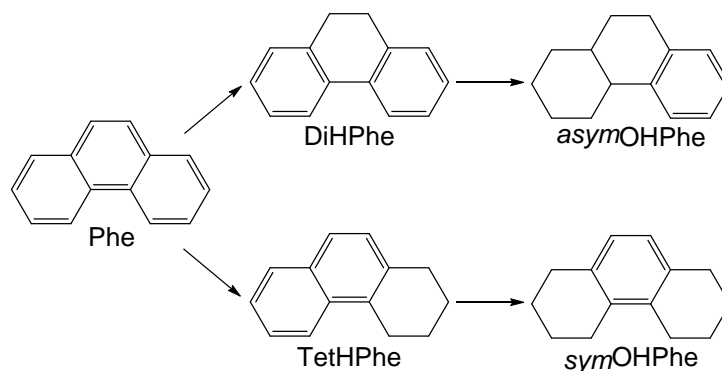
Table 1.4. Equilibrium constants for hydrogenation of polyaromatic compounds at different temperatures^{68,69}

	Log K _a at			ΔH ^o , ^a kcal/mol
	300°C	350°C	400°C	
Naphthalene + 2H ₂ → tetralin	-1.13	-2.03	-2.80	-30
Phenanthrene + H ₂ → 9,10-dihydrophenanthrene	-1.57	-1.94	-2.25	-12
Fluorene + 3H ₂ → cis-hexahydrofluorene	-2.88	-4.17	-5.27	-42

^aThe enthalpies are derived from the slopes of the van't Hoff plots and are assumed to be standard enthalpies of reaction, although they are not listed as such by the authors.

The hydrogenation reactivity of the aromatic compounds followed the order: polyaromatics ≥ diaromatics > monoaromatics.^{70,71} First-ring hydrogenation of condensed polyaromatic hydrocarbons is kinetically favored and occurs at relatively low temperatures and pressures. The rates of hydrogenation of subsequent rings tend to become lower, and hydrogenation of the last ring proceeds with considerable difficulty compared to the initial hydrogenation steps. It is generally found that the reaction on sulfided Co/Ni-Mo/W catalysts is around first order in the reactant hydrocarbon and in H₂.^{51,72-77}

The polyaromatic hydrogenation occurs ring by ring in successive steps which are all reversible. Phenanthrene, for example, is a polycyclic aromatic with three fused benzene rings, and its structure is very stable.⁷⁸ Already in 1940s, Linstead *et al.*⁷⁹ studied the catalytic hydrogenation of phenanthrene for stereochemistry. Later on, the kinetic models for this reaction have been developed using Langmuir-Hinshelwood-type rate equations,^{70,76} where adsorption and desorption of reactants and products is quasi-equilibrated. This process has several different pathways due to the different primary products, secondary products and the different properties of catalysts. Scheme 1.3 shows a typical reaction scheme of phenanthrene hydrogenation over Ni-MoS₂/Al₂O₃.^{76,80} Phenanthrene is first hydrogenated to dihydro-phenanthrene (DiHPhe) and tetrahydro-phenanthrene (TetHPhe) which are usually the two primary products. Then, DiHPhe reacts to form asymOHPhe and TetHPhe can be hydrogenated to symOHPhe and asymOHPhe as two secondary products.



Scheme 1.3. Reaction network derived from hydrogenation of Phenanthrene. ^{76,81–83}

It was reported that during hydrogenation, polyaromatic compounds first adsorb on the basal plane of MoS₂ with strong van der Waals interactions according to DFT and STM studies.^{84,85} The orientation of the adsorption of phenanthrene is affected by steric factors associated with the catalyst surface as well as the molecule itself, and the addition of hydrogen atoms to one side of the molecule was typically assumed.⁷⁹ The presence of Ni on MoS₂ edges, in addition, promotes faster hydrogenation of the adsorbed phenanthrene, which is attributed to lower activation energies for hydrogen addition and better stabilization of the partially hydrogenated intermediates.⁷⁶ Consequently, Ni-decorated MoS₂ edge have much higher intrinsic hydrogenation activity in comparison to the unpromoted edge, and with distinct selectivity towards deeply hydrogenated products.

1.2 Transition Metal Sulfides

Although noble metal catalysts exhibit extraordinary performance in hydrogenation reactions compared to transition metal sulfides (TMS), they are far from practical materials for applications in hydroprocessing of crude oil due to catalyst poisoning and prohibitively high costs.⁸⁶ TMS catalysts have been therefore used extensively. The beginning of their success dates back to 1920s when Germany started research on catalytic coal liquefaction and coal liquids upgrading, which initiated the development of Mo-based or W-based catalysts with Ni or Co promoters.^{87–89} Until today, such basic compositions have been retained with various modifications by using additives, alternate promoters, or optimized preparation methods. Consequently, the catalytic performance of TMS catalysts has been continuously improved, owing to research efforts from institutions and petroleum industries over the last decades.

1.2.1 Structure of Mo(W)S₂

MoS₂, as the most important TMS, is usually a semiconductor (indirect band gap $E_g \approx 1.3$ eV) with layered, anisotropic and two-dimensional crystal structures.^{9,90,91} Despite the differences in activity, WS₂ shares a similar crystalline structure as MoS₂. The crystallographic representation of MoS₂ is illustrated in Figure 1.6, as it naturally occurs as 2H-MoS₂ (hexagonal symmetry, two layers per unit cell).^{91–94} Figure 1.6 shows the coordination of Mo to S, with the Mo atoms sitting in a trigonal prismatic configuration with six S atoms and MoS₆ polyhedra sharing edges within the slabs. Layers are stacking along the c-axis with a sequence of ABAB, and they are held together by weak van der Waals forces with the interlayer distance of ca. 6.5 Å,^{90,91} which explains why MoS₂ and WS₂ can serve as lubricants even at high temperature.⁹⁵ The (0 0 0 1) surface of MoS₂ crystallites is the so-called basal plane which is often considered to be catalytically inert (or much less active), while coordinatively unsaturated S and Mo atoms can form at the step edge of the basal plane. As with other solid catalysts, the catalytic activity of MoS₂ originates from these defects known as coordinatively unsaturated sites (CUS).

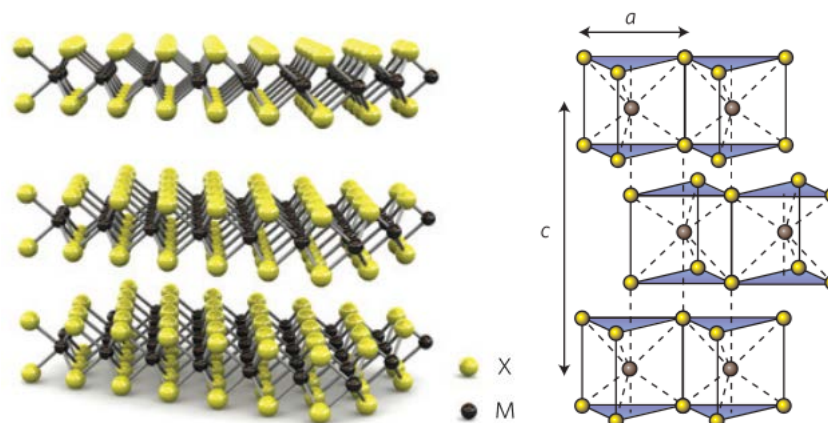


Figure 1.6. Three-dimensional schematic representation of a typical MX_2 structure⁹⁶ and crystal structure of 2H-MX_2 ,⁹¹ in which $\text{M}=\text{Mo}$ or W , and $\text{X}=\text{S}$ or Se . Reprinted by permission from Macmillan Publishers Ltd: Nature nanotechnology, ref⁹⁶ and ref⁹¹, copyright 2011 and 2012.

1.2.2 Proposed Models for Co or Ni Promoted Mo(W)S_2

TMS catalysts, used in refineries, are usually CoMo , NiMo , or NiW supported on $\gamma\text{-Al}_2\text{O}_3$ with $\text{Co(Ni)}/[\text{Co(Ni)} + \text{Mo(W)}]$ molar ratios of 0.2-0.4.⁹⁷ CoMo -based catalysts are very efficient in the HDS but are less active for HDN or aromatic hydrogenation. Conversely, NiMo and NiW based catalyst are better HDN and hydrogenation catalysts and are preferred when hydrotreating feedstocks with higher concentrations of aromatics. During the application of TMS materials in petroleum industry, various models and theories were developed for the structure and function of the promoted MoS_2 or WS_2 , with the purpose to understand the intrinsic catalytic activities of the sulfide phase.^{9,32,98}

Lipsch and Schuit⁹⁹ first suggested the monolayer structure for Co-promoted $\text{MoS}_2/\gamma\text{-Al}_2\text{O}_3$ at the early state of research on TMS catalysts. In this model, Mo^{6+} ion combines with O^{2-} in the form of a Mo-O-Al bridge and develops into a MoO_3 monolayer in the oxide precursor. Co replaces the Al^{3+} adjoining the Mo monolayer and stabilizes the structure. During sulfidation, S^{2-} replaces O^{2-} . In hydrogenation, some S^{2-} is removed and Mo^{6+} is reduced to Mo^{3+} which is considered as the active sites. However, this model cannot properly explain the promotion effect of Ni or Co.

The intercalation model, which was later proposed by Voorhoeve *et al.*,^{100,101} assumes that Co/Ni atoms occupy octahedral sites in the van der Waals gaps between the MoS_2 or WS_2 layers and form a sandwich structure. But Farragher *et al.*¹⁰² pointed out that ion insertion into MoS_2 or WS_2 slabs is energetically unfavorable. Instead, they proposed a pseudo-intercalation model that Co or Ni is inserted into the edge of S-Mo-S

octahedra. However, this model cannot explain the improved activity of a well-mixed Ni_3S_2 and MoS_2 mixture.

The contact synergy model, also called remote control model, assumes the presence of layered MoS_2 as well.^{37,103–105} In this model, Ni or Co are as separated phases which are in intimate contact with the layered structure of MoS_2 or WS_2 . All phases can activate H_2 by spill-over and can synergistically contribute to different activity and selectivity in catalytic reaction.^{103,104} H_2 spillover reduces the sulfide phase and gives rise to two kinds of active sites: M^{n+} which is formed by removing sulfur and M-SH which is formed at highly reducing conditions (M stands for transition metals). However, this model lacks evidence to prove the dispersion of the active hydrogen on surface.

The rim-edge model proposed by Daage and Chianelli¹⁰⁶ aimed at explaining the reaction selectivity of DBT with steric impact over unsupported sulfide catalysts. As Figure 1.7 shows, this model proposes that two kinds of active sites are located at the rim and edge positions on MoS_2 . The rim position is related to a hydrogenation center, and the edge is a hydrogenolysis center. The increased stacking of MoS_2 crystals results in the loss of rim sites, thereby favoring hydrogenolysis.

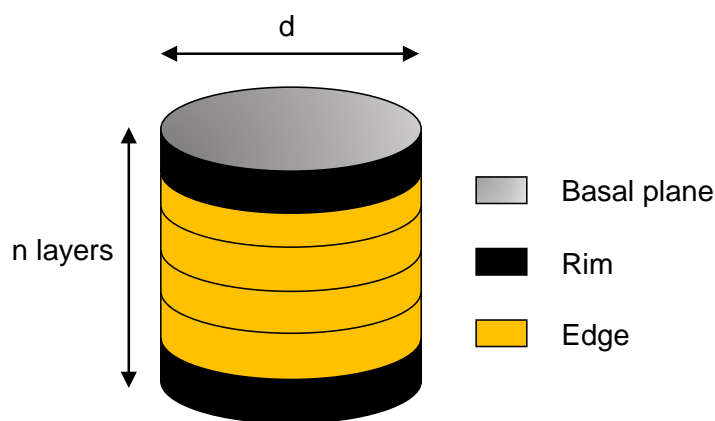


Figure 1.7. Rim-edge model.¹⁰⁶

During the last decades, Co(Ni)-Mo-S model has been developed by Topsøe *et al.*,^{107–112} with a detailed picture of the CoMoS phase on the atomic scale shown by extended X-ray-absorption fine structure (EXAFS), high-resolution scanning tunneling microscopy (STM) and density functional theory (DFT), as shown in Figure 1.8a-b. It describes a model in which nano-sized hexagonal MoS_2 particles are decorated with Co at the edges to form the catalytically highly active Co-Mo-S phase. Co exists in three different phases in the catalyst (Figure 1.8a). One is inside Al_2O_3 forming a spinel structure and is not active. The second phase is Co-sulfide on the surface of the support. In the third phase, Co is incorporated into MoS_2 and forms a Co-Mo-S phase. In this phase, Co is

placed at the edges of the MoS₂ hexagonal plane, and the phase is not formed with a well-defined ratio, but it is a cluster structure.

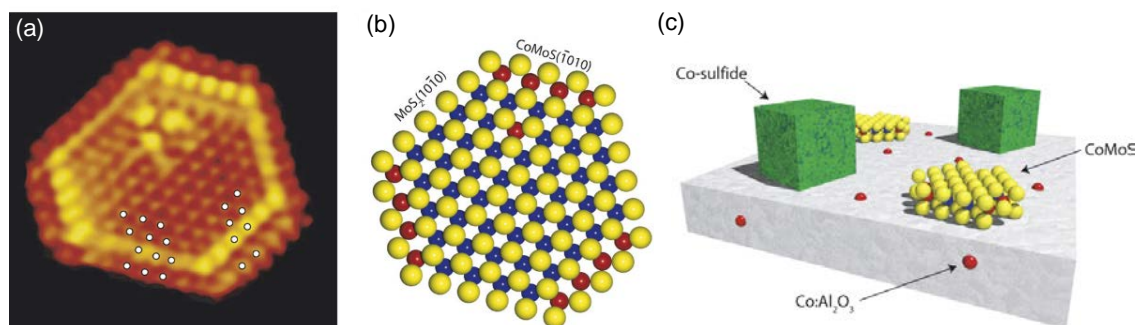


Figure 1.8. (a) Atom-resolved STM image of Co–Mo–S, (b) the ball model of Ni–Mo–S, (c) illustrative picture of three phases in a CoMoS catalyst.^{108,110} Republished with permission of Elsevier Science and Technology Journals, from Location and coordination of promoter atoms in Co- and Ni-promoted MoS₂-based hydrotreating catalysts, Jeppe V. Lauritsen, Jakob Kibsgaard, Georg H. Olesen, Poul G. Moses, Berit Hinnemann, Stig Helveg, Jens K.Nørskov, BjerneS. Clausen, Henrik Topsøe, Erik Lægsgaard, Flemming Besenbacher, 249, 2, 2007; permission conveyed through Copyright Clearance Center, Inc.

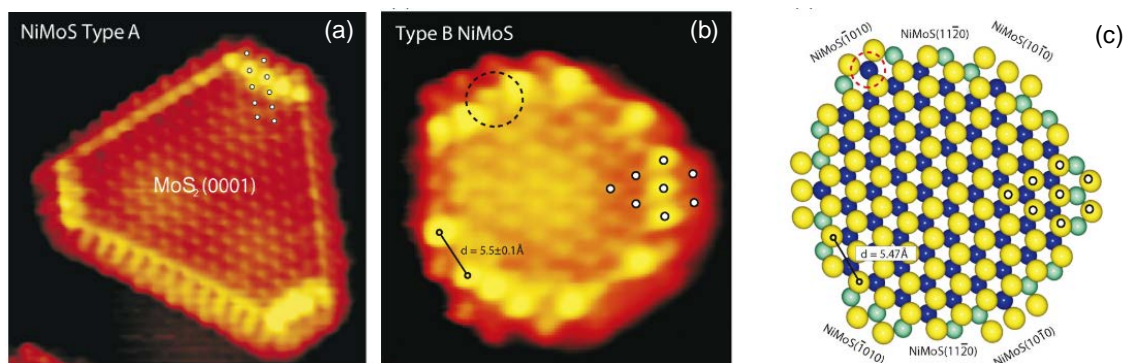


Figure 1.9. (a) Atom-resolved STM image of Type A and (b) Type B Ni–Mo–S, and (c) ball model of Type B Ni–Mo–S.¹⁰⁸ Republished with permission of Elsevier Science and Technology Journals, from Location and coordination of promoter atoms in Co- and Ni-promoted MoS₂-based hydrotreating catalysts, Jeppe V. Lauritsen, Jakob Kibsgaard, Georg H. Olesen, Poul G. Moses, Berit Hinnemann, Stig Helveg, Jens K.Nørskov, BjerneS.Clausen, Henrik Topsøe, Erik Lægsgaard, Flemming Besenbacher, 249, 2, 2007; permission conveyed through Copyright Clearance Center, Inc.

Similar investigation by STM has been undertaken for the structure of the Ni-promoted system, showing that the Ni-Mo-S phase also exists with a similar structure to Co-Mo-S.^{111,113–115} The STM image in Figure 1.9 shows that Ni atoms are incorporated at the S edges of the particle and lead to a cluster on both Ni-promoted S edges and unpromoted

Mo edges. Different annealing temperatures yielded two configurations of Ni-Mo-S clusters, as shown in Figure 1.9a-b where type A is a truncated triangular and type B is a complex dodecagonal-like structure. Ni is located at different sites in the two types of structures, which represents the active site at the edges and corners. However, this model is based on an idealized condition, i.e., only on single crystals under high vacuum. The actual structure of the catalysts under reaction conditions still lacks direct evidence.

1.2.3 Supported Catalysts and the Support Effect

Industrial hydrotreating catalysts usually use γ - Al_2O_3 to disperse TMS compounds due to its outstanding textural and mechanical properties and its relatively low cost.¹¹⁶ The high specific surface area (200-350 $\text{m}^2 \text{g}^{-1}$), controllable pore size, and its affinity with sulfide can yield a high dispersion of the sulfide phase. Besides, its acidic nature has been found to have a profound impact on the catalytic properties of the whole material, which provides opportunities for further modifications.

Due to the strong interaction between TMS and γ - Al_2O_3 , two kinds of Co(Ni)-Mo(W)-S sites were proposed by Topsøe and Clausen¹¹⁷: Type I sites for monolayer slabs and Type II sites occur on multilayered slabs. Type I sites exhibit lower activity than Type II sites in HDS reactions, which can be attributed to either electronic or geometric factors induced by γ - Al_2O_3 . Therefore, many studies were focused on weakening the catalyst-support interaction toward the formation of Type II structures, while maintaining high dispersion and a good decoration of Mo(W) S_2 with promoters.

Several support candidates such as carbon, SiO_2 , TiO_2 , ZrO_2 , zeolites, amorphous silica alumina(ASA), mesoporous silica, and their mixtures have been used during the development of TMS catalysts.^{98,113,115,118–129} Further strategies include modifying γ - Al_2O_3 by adding additives such as P, F, B, Si, Mg and Zn to tune the acidity of γ - Al_2O_3 .^{130–140} Such modifications changed the interaction between the impregnation solution and the support, thus affecting the dispersion of the active phase and the reducibility of the oxidic precursor.^{130,133,141} For example, the impregnation of Cl or F on γ - Al_2O_3 support was reported to improve the acid strength of the Lewis acid sites and Brønsted acid sites^{134–137,140,142,143} due to the electron-withdrawing effects induced by Cl or F ion. The resulted F- Al_2O_3 support facilitated the transformation of tungsten oxy-sulfides to tungsten sulfides, enhanced the acidity of SH species, and greatly promoted the HDS and HDN activities.^{133,141} It was also observed by Gutiérrez *et al.*¹²⁶ that the promotion effect of Ni on MoS_2 varied on SBA-15 (no Lewis acid site) and γ - Al_2O_3 , owing to different acid properties and morphology of the active sulfide phase. An electron deficient character of the RuS_2 supported on Y-zeolite was observed,^{138,139} together with

an enhancement in the hydrogenation ability compared to a conventional Ni-MoS₂/γ-Al₂O₃ catalyst. Li et al.¹²⁰ reported the encapsulation of Ni-Mo-S clusters in the super-cavity of ultra-stable Y zeolite(USY), the synergy between these clusters and Brønsted acid sites enables HDS of DBT with high activity.

1.2.4 Role of NiS_x on Ni-Mo(W)S₂ Catalysts

The formation of the active Ni-Mo(W)-S phase on Ni-promoted MoS₂ or WS₂ has gained more interests from research institutes and refineries, as the need for deep hydrogenation grows. A maximum concentration of this active phase on NiMo(W)S₂ was reported to be at a Ni metal molar fraction (Ni/Metal) of ca. 1:3 at the edge.^{80,144–146} Thus, any Ni that can no longer be accommodated into the Ni-Mo(W)-S phase will segregate in the form of NiS_x crystals. This is a thermodynamically favored process^{145,147–150} which happens during sulfidation or in spent catalysts after long periods of utilization.^{147,151–153} The segregated NiS_x crystals inevitably exist on Ni-containing TMS catalysts and are associated with a rather low activity for HDS, HDN and HYD.^{80,145,154–156} Depending on the actual reaction conditions, various type of NiS_x were observed, including Ni₃S₂,^{154,157} Ni₇S₆,¹⁵⁸ Ni₉S₈,^{120,157,159} NiS,¹⁵⁸ and/or Ni₃S₄,¹⁵⁷ due to the complexity of the Ni-S phase diagram.^{160–162} Experimental results and theoretical calculations show that the sintering of Ni to form Ni₃S₂ (heazlewoodite) is mostly common.^{113,115,150,152,154,160,163,164} The crystal size varies from 5 nm to few hundreds of nm in diameter, and to some extent such NiS_x particles decrease surface area and pore volume,^{145,165} hence decreasing the activities of the catalysts in hydrotreating reactions.⁸⁰ The formation of NiS_x can be slowed down by having a higher initial MoS₂(WS₂) dispersion and/or good Ni-Mo(W) mixing.¹⁴⁵

1.3 Scope of the Thesis

The catalytic properties of MoS₂ and WS₂ are a major research topic owing to their extensive application in hydrotreating to produce high-quality fuels from heavy crudes. Among all the TMS catalysts, Ni promoted WS₂ is considered to be more active in hydrogenation, compared to Ni- or Co-promoted MoS₂.^{9,37,51,100,166–178} However, the origin of the outstanding hydrogenation functionality of the Ni-W-S phase has not been rationalized beyond empirical observations.^{173,178} Another weak spot in the literature is that the disorder of the Ni-Mo(W)S₂ phase and formation of NiS_x crystals have always obscured the quantitative structure–activity relationship of the Ni promoters at the MoS₂ or WS₂ edge. Hence, revealing the intrinsic activity of each Ni promoting site is still a challenging task.

HDS and HDN reactions on TMS catalysts, mostly on MoS₂ based catalysts, have been extensively studied over decades, while HDA is gaining more attention as the need of heavy oil conversion grows. However, neither the hydrogenation activity of the TMS catalysts in the absence of desulfurization route nor the hydrogen activation on the Ni-Mo(W)-S phase has been investigated in detail. Therefore, the objective of this thesis is to gain a deeper understanding of aromatic hydrogenation reactions over Ni-MoS₂/γ-Al₂O₃ and Ni-WS₂/γ-Al₂O₃ catalysts on a molecular level.

In the first part of the thesis, the origin of the higher hydrogenation activity of the Ni-W-S, compared to its counterpart Ni-Mo-S, is explored using a series of Ni-Mo(W)S₂/γ-Al₂O₃ catalysts. To this end, oxide precursors with varying Ni molar metal fractions, Ni/(W+Ni), from 0 to 0.67 were synthesized by incipient wetness impregnation using γ-Al₂O₃ as the support. Sulfidation of the materials was conducted in H₂S/H₂, which was followed by temperature programmed sulfidation. Structural information was gathered by X-ray diffraction (XRD), transmission electron microscopy (TEM), and Raman spectroscopy. Infrared spectra of the adsorbed probe molecules, including NO, CO, pyridine and 2,6-dimethylpyridine (DMP), provided information about acid sites and exposed metal sites on sulfide materials. Phenanthrene (PHE) was chosen as the model compound to study the aromatic hydrogenation activity of Ni-WS₂/γ-Al₂O₃ catalysts, in the absence of defunctionalization route. The results show that the rate of PHE hydrogenation on Ni-Mo(W)S₂/Al₂O₃ is linearly correlated to the concentration of sulfhydryl (SH) groups vicinal to the edge-decorated Ni. In comparison, SH groups close to Mo and W show a much lower activity. The higher activity of Ni-WS₂ arises from a higher tendency of the accessible Ni to stabilize more SH groups, compared to Ni-MoS₂.

In the second part of the thesis, large NiS_x particles on Ni-WS₂/γ-Al₂O₃ are removed by a post-synthetic method with concentrated hydrochloric acid solution, according to the report from Duchet et al.^{179,180}. This procedure could minimize the hindrance from the catalytically inactive NiS_x, while leaving the structural integrity of the Mo(W)S₂ phase unaffected. The structure-activity relation was therefore qualitatively and quantitatively elucidated. The impacts from the acid treatment on Ni-WS₂/γ-Al₂O₃ were also investigated using IR spectroscopy with adsorption of CO, NO, pyridine, and DMP. The rate for hydrogenation of PHE increased by up to 5 times, apparently owing to the removal of NiS_x clusters over Ni-WS₂/γ-Al₂O₃, which was, in turn, attributed to a higher concentration of accessible edge-decorated Ni as well as a higher concentration of SH groups upon H₂ and H₂S dissociation.

1.4 References

- (1) Dudley, B. London, UK 2018.
- (2) Campbell, C. J.; Laherrère, J. H. *Sci. Am.* **1998**, 278 (3), 78–83.
- (3) Speight, J. G. *Knovel*. Online version available at:
<http://www.knovel.com/web/portal/browse/display> **2012**.
- (4) Energy Information Administration. *Crude oils have different quality characteristics*; Washington, DC, 2012.
- (5) Speight, J. G.; Ozum, B. *Petroleum refining processes*; CRC Press, 2001.
- (6) Speight, J. G. *The chemistry and technology of petroleum*; CRC press, 2014.
- (7) Petroleum.co.uk. Petroleum Composition
<http://www.petroleum.co.uk/composition>.
- (8) Demirbas, A.; Alidrisi, H.; Balubaid, M. A. *Pet. Sci. Technol.* **2015**, 33 (1), 93–101.
- (9) Bensch, W. *Hydrotreating: Removal of Sulfur from Crude Oil Fractions with Sulfide Catalysts*; Elsevier Ltd., 2013; Vol. 7.
- (10) Gateau, P.; Hénaut, I.; Barré, L.; Argillier, J. F. *Oil gas Sci. Technol.* **2004**, 59 (5), 503–509.
- (11) Suslick, S. B.; Schiozer, D. J.; Nepomuceno, F.; Furtado, R. In *SPE Hydrocarbon Economics and Evaluation Symposium*; Society of Petroleum Engineers, 2003.
- (12) Speight, J. G. *Handbook of petroleum product analysis*; John Wiley & Sons, 2015; Vol. 182.
- (13) Speight, J. G. *Environmental analysis and technology for the refining industry*; John Wiley & Sons, 2005; Vol. 167.
- (14) Akhmetov, A. F.; Krasil'nikova, Y. V. *Khim. Zh* **2011**, 18 (2), 93–98.
- (15) Dechaine, G. P.; Gray, M. R. *Energy & Fuels* **2010**, 24 (5), 2795–2808.

- (16) Liu, T.; Lu, J.; Zhao, X.; Zhou, Y.; Wei, Q.; Xu, C.; Zhang, Y.; Ding, S.; Zhang, T.; Tao, X. *Energy & Fuels* **2015**, 29 (4), 2089–2096.
- (17) Liu, H.; Wang, Z.; Guo, A.; Lin, C.; Chen, K. *Pet. Sci. Technol.* **2015**, 33 (2), 203–210.
- (18) UOP-Honeywell. Refining Process Flow <https://www.uop.com/refining-process-flow/>.
- (19) EIA. *International Energy Agency. Statistics European Union-28.*; 2012.
- (20) Imran, A.; Varman, M.; Masjuki, H. H.; Kalam, M. A. *Renew. Sustain. Energy Rev.* **2013**, 26, 739–751.
- (21) Lim, M. C. H.; Ayoko, G. A.; Morawska, L.; Ristovski, Z. D.; Jayaratne, E. R. *Atmos. Environ.* **2005**, 39 (40), 7836–7848.
- (22) Borrás, E.; Tortajada-Genaro, L. A.; Vázquez, M.; Zielinska, B. *Atmos. Environ.* **2009**, 43 (37), 5944–5952.
- (23) Reşitoğlu, İ. A. K. A. A. K. *Clean Technol. Environ. Policy* **2015**, 17 (1), 15–27.
- (24) Lloyd, A. C.; Cackette, T. A. *J. Air Waste Manage. Assoc.* **2001**, 51 (6), 809–847.
- (25) Gauderman, W. J.; Avol, E.; Gilliland, F.; Vora, H.; Thomas, D.; Berhane, K.; McConnell, R.; Kuenzli, N.; Lurmann, F.; Rappaport, E. *N. Engl. J. Med.* **2004**, 351 (11), 1057–1067.
- (26) Knudsen, K. G.; Cooper, B. H.; Topsøe, H. *Appl. Catal. A Gen.* **1999**, 189 (2), 205–215.
- (27) ISODA, D. *Adv. Catal.* **1998**, 42, 345.
- (28) Song, C. *Chemistry of diesel fuels*; CRC Press, 2000.
- (29) Song, C. *Prepr Pap. Am Chem Soc Div Fuel Chem* **2002**, 47, 438–444.
- (30) Song, C. *Catal. Today* **2003**, 86 (1–4), 211–263.
- (31) Gates, B. C.; Topsøe, H. *Polyhedron* **1997**, 16 (18), 3213–3217.
- (32) Topsøe, H.; Clausen, B. S.; Massoth, F. E.; Anderson, J. R.; Boudart, M. *by*

- Anderson, JR, Boudard, M., Springer, Berlin 1996, 11.*
- (33) Cattenot, M.; Portefaix, J.-L.; Afonso, J.; Breysse, M.; Lacroix, M.; Perot, G. *J. Catal.* **1998**, *173* (2), 366–373.
- (34) Ma, X.; Sakanishi, K.; Mochida, I. *Ind. Eng. Chem. Res.* **1996**, *35* (8), 2487–2494.
- (35) Babich, I. .; Moulijn, J. . *Fuel* **2003**, *82* (6), 607–631.
- (36) Ho, T. C. *Catal. Rev. Sci. Eng.* **1988**, *30* (1), 117–160.
- (37) Grange, P. *Catal. Rev.* **1980**, *21* (777306419), 135–181.
- (38) Chorkendorff, I.; Niemantsverdriet, J. W. *Concepts of modern catalysis and kinetics*; John Wiley & Sons, 2017.
- (39) Hrabar, A. Technische Universität München 2011.
- (40) Katritzky, A. R.; Ramsden, C. A.; Joule, J. A.; Zhdankin, V. V. *Handbook of heterocyclic chemistry*; Elsevier, 2010.
- (41) Shin, S.; Sakanishi, K.; Mochida, I.; Grudoski, D. A.; Shinn, J. H. *Energy & Fuels* **2000**, *14* (3), 539–544.
- (42) Zhao, Y.; Kukula, P.; Prins, R. *J. Catal.* **2004**, *221* (2), 441–454.
- (43) Zhao, Y.; Prins, R. *J. Catal.* **2004**, *222* (2), 532–544.
- (44) Schwartz, V.; da Silva, V. T.; Oyama, S. T. *J. Mol. Catal. A Chem.* **2000**, *163* (1–2), 251–268.
- (45) Clark, P.; Wang, X.; Deck, P.; Oyama, S. T. *J. Catal.* **2002**, *210* (1), 116–126.
- (46) Portefaix, J. L.; Cattenot, M.; Guerriche, M.; Breysse, M. *Catal. Letters* **1991**, *9* (1–2), 127–132.
- (47) Furimsky, E.; Massoth, F. E. *Catal. Rev.* **2005**, *47* (3), 297–489.
- (48) Ullman, T. L. *SAE Trans.* **1989**, 833–851.
- (49) Ullman, T. L. *Investigation of the effects of fuel composition and injection and combustion system type on heavy-duty diesel exhaust emissions. Final report*,

Southwest Research Inst., San Antonio, TX (USA), 1989.

- (50) Cooper, B. H.; Donnis, B. B. L. *Appl. Catal. A Gen.* **1996**, 137 (2), 203–223.
- (51) Stanislaus, a.; Cooper, B. *Catal. Rev.* **1994**, 36 (May 2013), 75–123.
- (52) *Regulation (EC) No. 715/2007 of the European Parliament and of the Council*; 2007.
- (53) Wang, H.; Dai, F.; Li, Z.; Li, C. *Energy & Fuels* **2015**, 29 (8), 4902–4910.
- (54) Romero, C. M. C.; Thybaut, J. W.; Marin, G. B. *Catal. Today* **2008**, 130 (1), 231–242.
- (55) Shin, J.; Oh, Y.; Choi, Y.; Lee, J.; Lee, J. K. *Appl. Catal. A Gen.* **2017**, 547, 12–21.
- (56) Choi, Y.; Lee, J.; Shin, J.; Lee, S.; Kim, D.; Lee, J. K. *Appl. Catal. A Gen.* **2015**, 492, 140–150.
- (57) Girgis, M. J.; Gates, B. C. *Ind. Eng. Chem. Res* **1991**, 30, 2021–2058.
- (58) Wilson, M. F.; Fisher, I. P.; Kriz, J. F. *J. Catal.* **1985**, 95 (1), 155–166.
- (59) Matsunaga, A. *Anal. Chem.* **1983**, 55 (8), 1375–1379.
- (60) Grizzle, P. L.; Thomson, J. S. *Anal. Chem.* **1982**, 54 (7), 1071–1078.
- (61) Chasey, K. L.; Aczel, T. *Energy & fuels* **1991**, 5 (3), 386–394.
- (62) Ijam, M. J.; Al-Qatami, S. Y.; Arif, S. F. *Am. Chem. Soc. Div. Pet. Chem. Prepr. States* **1990**, 35 (CONF-900802--).
- (63) Weisser, O.; Landa, S. *Sulphide catalysts, their properties and applications*; Elsevier, 2013.
- (64) Chianelli, R. R.; Daage, M.; Ledoux, M. J. *Adv. Catal.* **1994**, 40, 177–232.
- (65) Chianelli, R. R. *Catal. Rev.* **1984**, 26 (3–4), 361–393.
- (66) Reid, R. C.; Prausnitz, J. M.; Poling, B. E. **1987**.
- (67) Jaffe, S. B. *Ind. Eng. Chem. Process Des. Dev.* **1974**, 13 (1), 34–39.

- (68) Frye, C. G. *J. Chem. Eng. Data* **1962**, 7 (4), 592–595.
- (69) Frye, C. G.; Weitkamp, A. W. *J. Chem. Eng. Data* **1969**, 14 (3), 372–376.
- (70) Beltramone, a. R.; Resasco, D. E.; Alvarez, W. E.; Choudhary, T. V. *Ind. Eng. Chem. Res.* **2008**, 47, 7161–7166.
- (71) Kokayeff, P. *Decker, New York* **1994**, 315.
- (72) Ahuja, S. P.; Derrien, M. L.; Le Page, J. F. *Ind. Eng. Chem. Prod. Res. Dev.* **1970**, 9 (3), 272–281.
- (73) van Meerten, R. Z. C.; Coenen, J. W. E. *J. Catal.* **1975**, 37 (1), 37–43.
- (74) Le Page, A. J. F. **1988**.
- (75) Sapre, A. V; Gates, B. C. **1981**.
- (76) Schachtl, E.; Yoo, J. S.; Gutiérrez, O. Y.; Studt, F.; Lercher, J. A. *J. Catal.* **2017**, 352, 171–181.
- (77) Yui, S. M.; Sanford, E. C. *Am. Chem. Soc. Div. Pet. Chem. Prepr.* **1987**, 32 (CONF-8704347--).
- (78) Gutman, I.; Stanković, S. *Maced. J. Chem. Chem. Eng.* **2007**, 26 (2), 111–114.
- (79) Linstead, R. P.; Doering, W. E.; Davis, S. B.; Levine, P.; Whetstone, R. R. *J. Am. Chem. Soc.* **1942**, 64 (9), 1985–1991.
- (80) Schachtl, E.; Zhong, L.; Kondratieva, E.; Hein, J.; Gutiérrez, O. Y.; Jentys, A.; Lercher, J. A. *ChemCatChem* **2015**, 7 (24), 4118–4130.
- (81) Korre, S. C.; Klein, M. T.; Quann, R. J. *Ind. Eng. Chem. Res.* **1995**, 34 (1), 101–117.
- (82) Shabtai, J.; Veluswamy, L.; Oblad, A. G. *Am. Chem. Soc. Div. Fuel Chem, Prepr.* **1978**, 23 (1), 107.
- (83) Lemberon, J.-L.; Guisnet, M. *Appl. Catal.* **1984**, 13 (1), 181–192.
- (84) Moses, P. G.; Mortensen, J. J.; Lundqvist, B. I.; Nørskov, J. K. *J. Chem. Phys.* **2009**, 130 (10), 104709.

- (85) Lauritsen, J. V.; Besenbacher, F. *J. Catal.* **2015**, *328*, 49–58.
- (86) Mohanty, S.; Kunzru, D.; Saraf, D. N. *Fuel* **1990**, *69* (12), 1467–1473.
- (87) Donath, E. E.; Hoering, M. *Fuel Process. Technol.* **1977**, *1* (1), 3–20.
- (88) Derbyshire, F. J. *Catalysis in coal liquefaction: new directions for research*; IEA Coal Research London, 1988.
- (89) Donath, E. E. In *Catalysis*; Springer, 1982; pp 1–38.
- (90) Wang, Z. M. *MoS₂: materials, physics, and devices*; Springer Science & Business Media, 2013; Vol. 21.
- (91) Wang, Q. H.; Kalantar-Zadeh, K.; Kis, A.; Coleman, J. N.; Strano, M. S. *Nat. Nanotechnol.* **2012**, *7* (11), 699.
- (92) Wildervanck, J. C.; Jellinek, F. *Zeitschrift für Anorg. und Allg. Chemie* **1964**, *328* (5–6), 309–318.
- (93) Schutte, W. J. J.; De Boer, J. L. L.; Jellinek, F. *J. Solid State Chem.* **1987**, *70* (2), 207–209.
- (94) Dickinson, R. G.; Pauling, L. *J. Am. Chem. Soc.* **1923**, *45* (6), 1466–1471.
- (95) Weber, T.; Prins, H.; van Santen, R. A. *Transition metal sulphides: chemistry and catalysis*; Springer Science & Business Media, 2013; Vol. 60.
- (96) Radisavljevic, B.; Radenovic, A.; Brivio, J.; Giacometti, i V; Kis, A. *Nat. Nanotechnol.* **2011**, *6* (3), 147.
- (97) Chianelli, R. R.; Berhault, G.; Torres, B. *Catal. Today* **2009**, *147* (3–4), 275–286.
- (98) Vissers, J. P. R.; de Beer, V. H. J.; Prins, R. *J. Chem. Soc. Faraday Trans. 1 Phys. Chem. Condens. Phases* **1987**, *83* (7), 2145–2155.
- (99) Lipsch, J. M. J. G.; Schuit, G. C. A. *J. Catal.* **1969**, *15* (2), 179–189.
- (100) Voorhoeve, R. J. H.; Stuiver, J. C. M. *J. Catal.* **1971**, *23* (2), 228–235.
- (101) Voorhoeve, R. J. H. *J. Catal.* **1971**, *23* (2), 236–242.

- (102) Farragher, A. L.; Cossee, P. *JW Hightower, Ed* **1973**, 1301.
- (103) Delmon, B.; Matralis, H. In *Unsteady State Processes in Catalysis: Proceedings of the International Conference, 5-8 June, 1990, Novosibirsk, USSR; VSP, 1990*; p 25.
- (104) Delmon, B.; FROMENT, G. F. *Catal. Rev.* **1996**, 38 (1), 69–100.
- (105) Delmon, B. *Bull. des Soc. Chim. Belges* **1979**, 88 (12), 979–987.
- (106) Daage, M. *Journal of Catalysis*. 1994, pp 414–427.
- (107) Lauritsen, J. V.; Helveg, S.; Lægsgaard, E.; Stensgaard, I.; Clausen, B. S.; Topsøe, H.; Besenbacher, F. *J. Catal.* **2001**, 197 (1), 1–5.
- (108) Lauritsen, J. V.; Kibsgaard, J.; Olesen, G. H.; Moses, P. G.; Hinnemann, B.; Helveg, S.; Nørskov, J. K.; Clausen, B. S.; Topsøe, H.; Lægsgaard, E.; Besenbacher, F. *J. Catal.* **2007**, 249 (2), 220–233.
- (109) Helveg, S.; Lauritsen, J. V.; Lægsgaard, E.; Stensgaard, I.; Nørskov, J. K.; Clausen, B. S.; Topsøe, H.; Besenbacher, F. *Phys. Rev. Lett.* **2000**, 84 (5), 951–954.
- (110) Topsoe, H. *Appl. Catal. A Gen.* **2007**, 322 (SUPPL.), 3–8.
- (111) Topsøe, H.; Candia, R.; Topsøe, N.; Clausen, B. S.; Topsøe, H. *Bull. des Sociétés Chim. Belges* **1984**, 93 (8-9), 783–806.
- (112) Shuxian, Z.; Hall, W. K.; Ertl, G.; Knözinger, H. *J. Catal.* **1986**, 100 (1), 167–175.
- (113) Louwers, S. P. A.; Prins, R. *J. Catal.* **1992**, 133 (1), 94–111.
- (114) Niemann, W.; Clausen, B. S.; Topsøe, H. *Catal. Letters* **1990**, 4 (4–6), 355–363.
- (115) Louwers, S. P. A.; Prins, R. *J. Catal.* **1993**, 139 (2), 525–539.
- (116) Patrick, E.; Pascal, R.; Xénophon, K.; Hervé, T.; Jean-Luc, L. L.; Jean-Pierre, J.; Cédric, F. *Handbook of Porous Solids*. April 25, 2008.
- (117) Topsøe, H.; Clausen, B. S. *Appl. Catal.* **1986**, 25 (1–2), 273–293.

- (118) Dzwigaj, S.; Louis, C.; Breysse, M.; Cattenot, M.; Bellière, V.; Geantet, C.; Vrinat, M.; Blanchard, P.; Payen, E.; Inoue, S. *Appl. Catal. B Environ.* **2003**, *41* (1–2), 181–191.
- (119) Breysse, M.; Afanasiev, P.; Geantet, C.; Vrinat, M. *Catalysis Today*. Elsevier November 1, 2003, pp 5–16.
- (120) Li, D.; Xu, H.; Guthrie, G. D. *J. Catal.* **2000**, *189* (2), 281–296.
- (121) Van Der Meer, Y.; Hensen, E. J. M.; Van Veen, J. A. R.; Van Der Kraan, A. M. *J. Catal.* **2004**.
- (122) Van Der Meer, Y.; Vissenberg, M. J.; De Beer, V. H. J.; Van Veen, J. A. R.; Van Der Kraan, A. M. In *Industrial Applications of the Mössbauer Effect*, Cook, D. C., Hoy, G. R., Eds.; Springer Netherlands: Dordrecht, 2002; pp 51–57.
- (123) Li, D.; Nishijima, A.; Morris, D. E.; Guthrie, G. D. *J. Catal.* **1999**.
- (124) Eijsbouts, S.; De Beer, V. H. J.; Prins, R. *J. Catal.* **1991**.
- (125) Leglise, J.; Manoli, J. M.; Potvin, C.; Djega-Mariadassou, G.; Cornet, D. *J. Catal.* **1995**.
- (126) Gutiérrez, O. Y.; Singh, S.; Schachtl, E.; Kim, J.; Kondratieva, E.; Hein, J.; Lercher, J. A.; Han, W.; Nie, H.; Long, X.; Li, M.; Yang, Q.; Li, D. *ACS Catal.* **2014**, *4* (5), 1487–1499.
- (127) Li, Y.; Pan, D.; Yu, C.; Fan, Y.; Bao, X. *J. Catal.* **2012**, *286*, 124–136.
- (128) Ramírez, J.; Gutiérrez-Alejandre, A. *Catal. today* **1998**, *43* (1–2), 123–133.
- (129) Ramirez, J.; Gutiérrez-Alejandre, A. *J. Catal.* **1997**, *170* (1), 108–122.
- (130) Saih, Y.; Segawa, K. *Appl. Catal. A Gen.* **2009**, *353* (2), 258–265.
- (131) Chen, W.; Nie, H.; Li, D.; Long, X.; van Gestel, J.; Maugé, F. *J. Catal.* **2016**, *344*, 420–433.
- (132) Cervantes-Gaxiola, M. E.; Arroyo-Albiter, M.; Pérez-Larios, A.; Balbuena, P. B.; Espino-Valencia, J. *Fuel* **2013**, *113*, 733–743.
- (133) Sun, M.; Urgi, T.; Cattaneo, R.; van Langeveld, D.; Prins, R.; Bürgi, T.;

- Cattaneo, R.; van Langeveld, D.; Prins, R. *J. Catal.* **2001**, *201* (2), 258–269.
- (134) Corma, a.; Fornés, V.; Ortega, E. *J. Catal.* **1985**, *92* (2), 284–290.
- (135) Sharma, L. D.; Sinhamahapatra, P. K.; Sharma, H. R.; Mehrotra, R. P.; Balamalliah, G. *J. Catal.* **1977**, *48* (1–3), 404–407.
- (136) M., G. J.; L., J. E.; L., P. C.; J., V. R.; M., P. J. *J. Chem. Technol. Biotechnol.* **2007**, *38* (2), 105–113.
- (137) Guillaume, D.; Gautier, S.; Despujol, I.; Alario, F.; Beccat, P. *Catal. Letters* **1997**, *43* (3), 213–218.
- (138) Breysse, M.; Cattenot, M.; Kougonas, V.; Lavalley, J. C.; Mauge, F.; Portefaix, J. L.; Zotin, J. L. *J. Catal.* **1997**, *168* (2), 143–153.
- (139) Moraweck, B.; Bergeret, G.; Cattenot, M.; Kougonas, V.; Geantet, C.; Portefaix, J.-L.; Zotin, J. L.; Breysse, M. *J. Catal.* **1997**, *165* (1), 45–56.
- (140) Melchor, A.; Garbowski, E.; Mathieu, M.-V.; Primet, M. *J. Chem. Soc. {,} Faraday Trans. 1* **1986**, *82* (6), 1893–1901.
- (141) Han, W.; Nie, H.; Long, X.; Li, M.; Yang, Q.; Li, D. *Catal. Today* **2017**, *292*, 58–66.
- (142) Clet, G.; Goupil, J.-M.; Cornet, D. *Bull. Soc. Chim. Fr.* **1997**, *134* (2), 223–233.
- (143) Peri, J. B. *J. Phys. Chem.* **1966**, *70* (5), 1482–1491.
- (144) Gao, Q.; Ofosu, T. N. K.; Ma, S. G.; Komvokis, V. G.; Williams, C. T.; Segawa, K. In *Catalysis Today*; Elsevier, 2011; Vol. 164, pp 538–543.
- (145) Eijsbouts, S.; Li, X.; Bergwerff, J.; Louwen, J.; Woning, L.; Loos, J. *Catal. Today* **2017**, *292*, 38–50.
- (146) Alphazan, T.; Bonduelle-Skrzypczak, A.; Legens, C.; Boudene, Z.; Taleb, A.-L.; Gay, A.-S.; Ersen, O.; Copéret, C.; Raybaud, P. *J. Catal.* **2016**, *340*, 60–65.
- (147) Guichard, B.; Roy-Auberger, M.; Devers, E.; Pichon, C.; Legens, C.; Lecour, P. *Catal. Today* **2010**, *149* (1–2), 2–10.
- (148) Guichard, B.; Roy-Auberger, M.; Devers, E.; Legens, C.; Raybaud, P. *Catal.*

Today **2008**, 130 (1), 97–108.

- (149) Krebs, E.; Silvi, B.; Raybaud, P. *Catal. Today* **2008**, 130 (1), 160–169.
- (150) Schweiger, H.; Raybaud, P.; Toulhoat, H. *J. Catal.* **2002**, 212 (1), 33–38.
- (151) Eijsbouts, S.; Van Den Oetelaar, L. C. A.; Van Puijenbroek, R. R. *J. Catal.* **2005**, 229 (2), 352–364.
- (152) Karroua, M.; Matralis, H.; Grange, P.; Delmon, B. *Bull. des Sociétés Chim. Belges* **2010**, 104 (1), 11–18.
- (153) Eijsbouts, S. *Appl. Catal. A Gen.* **1997**, 158 (1), 53–92.
- (154) Kuriki, Y.; Yumura, M.; Ohshima, S.; Uchida, K.; Ikazaki, F. *Coal Sci. Technol.* **1995**, 24, 1347–1350.
- (155) Eijsbouts, S.; Anderson, G. H.; Bergwerff, J. A.; Jacobi, S. *Appl. Catal. A Gen.* **2013**, 458, 169–182.
- (156) Eijsbouts, S.; H.J. de Beer, V.; Prins, R. *J. Catal.* **1988**, 109 (1), 217–220.
- (157) Hein, J.; Gutiérrez, O. Y.; Schachtl, E.; Xu, P.; Browning, N. D.; Jentys, A.; Lercher, J. a. *ChemCatChem* **2015**, 7 (22), 3692–3704.
- (158) Zhao, X. J.; Wei, J. *J. Catal.* **1994**, 147 (2), 429–440.
- (159) Bocarando, J.; Huirache-Acuña, R.; Bensch, W.; Huang, Z.-D.; Petranovskii, V.; Fuentes, S.; Alonso-Núñez, G. *Appl. Catal. A Gen.* **2009**, 363 (1–2), 45–51.
- (160) Seim, H.; Fjellvåg, H.; Grønvold, F.; Stølen, S. *J. Solid State Chem.* **1996**, 121 (2), 400–407.
- (161) Parthé, E.; Gmelin, L. *Gmelin Handbook of inorganic and organometallic chemistry: TYPIX.. Standardized data and crystal chemical characterization of inorganic structure types*; Springer, 1993; Vol. 1.
- (162) Stølen, S.; Grønvold, F.; Westrum, E. F.; Kolonin, G. R. *J. Chem. Thermodyn.* **1991**, 23 (1), 77–93.
- (163) Matsubayashi, N.; Sato, T.; Shimada, H.; Imamura, M.; Yoshimura, Y.; Nishijima, A.; Kameoka, T.; Masuda, K. *Coal Sci. Technol.* **1995**, 24, 1495–

1498.

- (164) Eijsbouts, S.; Van Gestel, J. N. M.; Van Veen, J. A. R.; De Beer, V. H. J.; Prins, R. *J. Catal.* **1991**, *131* (2), 412–432.
- (165) Yoosuk, B.; Kim, J. H.; Song, C.; Ngamcharussrivichai, C.; Prasassarakich, P. *Catal. Today* **2008**, *130* (1), 14–23.
- (166) Kim, C.-H.; Yoon, W. L.; Lee, I. C.; Woo, S. I. *Appl. Catal. A Gen.* **1996**, *144* (1–2), 159–175.
- (167) Scheffer, B.; Mangnus, P. J.; Moulijn, J. a. *J. Catal.* **1990**, *121* (1), 18–30.
- (168) Reinhoudt, H. R.; van Langeveld, a. D.; Kooyman, P. J.; Stockmann, R. M.; Prins, R.; Zandbergen, H. W.; Moulijn, J. a. *J. Catal.* **1998**, *179* (2), 443–450.
- (169) Frank, J. P.; LePage, J. F. **1981**.
- (170) Reinhoudt, H. R.; Troost, R.; van Schalkwijk, S.; van Langeveld, A. D.; Sie, S. T.; Schulz, H.; Chadwick, D.; Cambra, J.; de Beer, V. H. J.; van Veen, J. A. R.; Fierro, J. L. G.; Moulijn, J. A. *Stud. Surf. Sci. Catal.* **1997**, *106*, 237–244.
- (171) Navalikhina, M. D.; Krylov, O. V. *Russ. Chem. Rev.* **1998**, *67* (7), 587–616.
- (172) Kameoka, T.; Yanase, H.; Nishijima, A.; Sato, T.; Yoshimura, Y.; Shimada, H.; Matsubayashi, N. *Appl. Catal. A Gen.* **1995**, *123* (2), 217–228.
- (173) Hensen, E. J. M.; van der Meer, Y.; van Veen, J. A. R.; Niemantsverdriet, J. W. *Appl. Catal. A Gen.* **2007**, *322* (0), 16–32.
- (174) Topsøe, H.; Clausen, B. S.; Massoth, F. E. *Hydrotreating catalysis*; Springer, 1996.
- (175) Zuo, D.; Vrinat, M.; Nie, H.; Maugé, F.; Shi, Y.; Lacroix, M.; Li, D. *Catal. today* **2004**, *93*, 751–760.
- (176) Yoshimura, Y.; Sato, T.; Shimada, H.; Matsubayashi, N.; Imamura, M.; Nishijima, A.; Higo, M.; Yoshitomi, S. *Catal. Today* **1996**, *29* (1–4), 221–228.
- (177) Sizova, I. A.; Serdyukov, S. I.; Maksimov, A. L.; Sinikova, N. A. *Pet. Chem.* **2015**, *55* (1), 38–44.

(178) Kelly, S. D.; Yang, N.; Mickelson, G. E.; Greenlay, N.; Karapetrova, E.; Sinkler, W.; Bare, S. R. *J. Catal.* **2009**, 263 (1), 16–33.

(179) J.C. Duchet, D. C. J. B. *Bull. Soc. Chim. Fr.* **1978**, 112–118.

(180) J.C. Duchet, D. C. J. B. *Bull. Soc. Chim. Fr.* **1979**, 221–228.

Chapter 2

Active sites on Ni-promoted transition metal sulfides that catalyze aromatics hydrogenation

This chapter is based on:

Luo, W., Shi, H., Schachtl, E., Gutiérrez, O. Y. & Lercher, J. A. Active Sites on Nickel-Promoted Transition-Metal Sulfides That Catalyze Hydrogenation of Aromatic Compounds. *Angew. Chemie - Int. Ed.* (2018). doi:10.1002/anie.201808428

Reprinted with permission from John Wiley and Sons, Copyright 2018.

Abstract: Hydrogenation on transition metal sulfides occurs at the edges of the sulfide slabs. The rate of hydrogen addition is directly proportional to the concentration of sulfhydryl (SH) groups at the slab edge and the metal atom attached to it. Sulfhydryl groups vicinal to edge-decorated Ni hydrogenate with much higher rates than SH close to Mo and W. Each subset of SH groups, however, exhibits nearly identical intrinsic activity and selectivity, independent of the sulfide composition. The higher activity of Ni-WS₂ compared to Ni-MoS₂ stems from a higher concentration of SH groups associated with a greater surface reducibility (i.e., a higher tendency of its surface vacancies to react with H₂) on the former sulfide.

2.1 Introduction

Co- and Ni-containing MoS₂ and WS₂ catalyze both hydrogenation of aromatic rings and hydrogenolysis of carbon-heteroatom linkages. Co-containing MoS₂ is preferentially applied for removal of sulfur with minimum hydrogenation, whereas the presence of Ni is used to achieve higher hydrogenation rates compared to Co-containing counterparts,^{1–5} and Ni-containing WS₂ catalyzes hydrogenation with even higher rates than Ni-MoS₂.^{1,6–14} The hydrogenation of aromatic rings is needed to adjust the quality of the hydroprocessed product (e.g., improve the cetane number) and is also a conversion route parallel to the direct hydrogenolysis of C-S and C-N bonds. Indeed, for the most refractory heterocompounds in crude oils, aromatics hydrogenation prior to defunctionalization is the only pathway with relevant rates.^{6–13} Thus, the hydrogenation of aromatic rings is a key reaction toward the efficient conversion of heavy feedstocks.^{15–18}

The Ni(Co)-Mo-S model, where Ni and Co cations substitute Mo at the edges of sulfide crystals, is widely accepted for describing the principal structure of the active mixed sulfide phase.^{4,7,19–21} The presence of promoter atoms with lower oxidation states than Mo at the edges of the sulfide slab has been thought to increase the concentration of S-vacancies, i.e., active sites and/or precursors to active sites for hydrodesulfurization (HDS). Studies have shown that similar active site structures exist on Ni-WS₂-based catalysts.^{6–13} However, it is unclear whether or not the high activity of Ni-WS₂ catalysts for hydrogenation is caused by differences in the strength of the metal-sulfur bonding or by different active sites.

To connect the chemical structure and concentration of active sites to their steady-state activity, we characterized the quality and quantity of functional sites on γ -Al₂O₃-supported transition metal sulfides with varying concentrations of Ni. This approach allowed identifying two subsets of surface SH groups, with each subset showing a characteristic activity and regioselectivity toward the hydrogenation of phenanthrene (PHE).; this reaction was chosen as the model for hydrogen addition reactions to polyaromatic molecules for three main reasons: (i) the absence of heteroatoms allows studying the conversion of aromatic rings alone, i.e., without confounding defunctionalization pathways; (ii) PHE contains two kinds of aromatic rings for us to analyze regioselectivity variations with Ni substitution, and (iii) it is PHE is a C₁₄ polycyclic aromatic hydrocarbon representative of those present in heavy oil fractions, whose reaction pathway and mechanism has been extensively studied.^{22,23}

Thus, the aim of this work was twofold. As a first target, we linked the physicochemical properties with the hydrogenation rates on WS₂-based catalysts by correlating the concentration of Ni-W-S sites with rates of hydrogenation of polyaromatic compounds. For the second target, we compared the properties of Ni-MoS₂ and Ni-WS₂ in order to better understand the superior properties of Ni-WS₂.

A series of γ -Al₂O₃-supported WS₂ catalysts with varying concentrations of Ni were synthesized, characterized, and were studied for the hydrogenation of phenanthrene (as a model for polyaromatic compounds) in the absence of defunctionalization pathways. The study reports on the relations between oxide precursors and sulfide catalysts, proposes structural models for the Ni-W-S phases in selected catalysts, and describes the consequences of the Ni-decoration degrees for the concentration of active sites for hydrogenation. It is shown that the rate of phenanthrene hydrogenation depended only on the concentration of SH groups on the surface of Ni-promoted phases, but not on the nature of the majority phase, be it MoS₂ or WS₂.

2.2 Experimental Section

2.2.1 Catalysts Preparation

The oxide precursors were prepared by incipient wetness impregnation of γ -Al₂O₃ (surface area of 248 m² g⁻¹, pore volume of 0.67 cm³ g⁻¹, and mesh size of 100-150 μ m), which was previously treated in 100 ml min⁻¹ synthetic air at 833 K for 2 h. The first impregnation was performed with aqueous solutions of ammonium metatungstate hydrate (Aldrich, \geq 99.0%) while the second was performed with aqueous solutions of nickel nitrate (Aldrich, \geq 98.5%). A trimetallic catalyst, Ni(2.5)MoWO₃/ γ -Al₂O₃ was prepared by the same procedure with aqueous solution of ammonium metatungstate hydrate and ammonium heptamolybdate (Aldrich, \geq 99.0%) for the first impregnation step. The impregnated materials were treated at 393 K for 4 h and 773 K for 4 h in 100 ml min⁻¹ synthetic air after each impregnation step. The W loading was 1.0-1.1 mmol per gram of catalyst for Ni-containing WO₃/ γ -Al₂O₃, while the Ni loading was varied between 0.05 and 1.89 mmol per gram of catalyst. Besides the major set of catalysts compiled in Table 2.2, two additional WO₃/ γ -Al₂O₃ samples were synthesized, containing 0.4 and 0.9 mmol W per gram of catalyst, respectively; the corresponding sulfided catalysts (WS₂/ γ -Al₂O₃-a and -b) were not characterized with respect to the slab characteristics and CUS concentration (NO adsorption). For Ni(2.5)MoWO₃/ γ -Al₂O₃, the W and Mo loadings were 0.4 mmol g⁻¹ each while the Ni loading was 0.42 mmol g⁻¹.

The oxide precursors were sulfided in a H₂S/H₂ gas mixture (20 ml min⁻¹, 10 vol. % H₂S) at 20 bar and 673 K with the temperature ramp of 5 K min⁻¹. Oxide precursors and sulfide catalysts are denoted hereafter as Ni(x)WO₃/γ-Al₂O₃ and Ni(x)WS₂/γ-Al₂O₃, respectively, where x is the measured Ni loading in wt.%. Non-promoted oxide and sulfided materials are denoted as WO₃/γ-Al₂O₃ and WS₂/γ-Al₂O₃, respectively. Non-promoted and Ni-promoted MoO₃/γ-Al₂O₃ and MoS₂/γ-Al₂O₃ materials, which had been used in a previous study,²⁴ were also employed in this work for comparison. In addition, an oxide precursor containing 0.43 mmol (2.5 wt.%) of Ni per gram of γ-Al₂O₃ was prepared by impregnation with an aqueous solution of Ni(NO₃)₂, followed by thermal treatment described above. After sulfidation, this sample is denoted as NiS_x/γ-Al₂O₃.

2.2.2 Characterization of Catalysts

N₂ adsorption-desorption isotherms, obtained at 77 K using a Thermo Finnigan Sorptomatic 1990 series instrument, were used to determine the specific surface areas and pore volumes. The samples were heated in vacuum at 573 K for 2 h before measurements. The **elemental analyses** of the oxide precursors were performed with fast sequential atomic absorption spectrometry at the Microanalytical Laboratory at Technische Universität München.

Transmission electron microscopy (TEM) measurements were performed on a JEOL JEM-2011 instrument operating at an acceleration voltage of 120 kV. Freshly sulfided catalysts were dispersed in ethanol and deposited on copper grids with supporting carbon films. At least 350 WS₂ slabs in the micrographs of each sample were included for the statistical analysis of the length and stacking height. The fraction of atoms at the edges was calculated with the assumption of a perfect hexagonal geometry²⁵ for the WS₂ slabs with interatomic distance $d_{W-W} = 3.2 \text{ \AA}$.

Temperature programmed sulfidation (TPS) was performed in a quartz flow reactor enclosed in a ceramic oven. The reactor was loaded with 0.1 g of the oxide precursor with particle size 250-355 μm and pretreated for 2 h at 393 K in 10 ml min⁻¹ He flow. After cooling to room temperature, the samples were sulfided in flowing H₂S/H₂ (10 ml min⁻¹, 10 vol.% H₂S), while heating to 923 K with a temperature increment of 5 K min⁻¹. The evolution and consumption of H₂S and H₂ was monitored with a mass spectrometer (Pfeiffer Vacuum QME 200).

NO adsorption on sulfide catalysts was determined by applying pulses of NO (10 vol.% NO/He) at 300 K. The concentration of NO at the exit of the reactor was monitored by a mass spectrometer (m/e=30). The total amount of NO adsorbed on the sample was

determined as the sum of NO uptake per pulse. The reproducibility of the amount of NO adsorption was better than $\pm 5\%$.

Powder X-ray diffraction (XRD) patterns were acquired in a Phillips X'Pert PRO system (Cu K_{α} , wavelength = 0.154056 nm) operating at 40 kV and 45 mA. The samples were measured with a scan rate of $1^{\circ} \text{ min}^{-1}$ (2θ).

UV-vis diffuse-reflectance (DR) spectra of the oxide precursors were collected with an Avantes Avaspec 2048 spectrometer equipped with an optical fiber (Avantes FCR-7UV400-2ME-HTX UV-Vis reflection probe). At room temperature, UV light illuminated the sample powders on a PTFE sample holder. The UV-Vis DR spectra were collected with an integration time of 33 ms, and 50 scans were accumulated. All spectra were normalized with the Kubelka-Munk function (defined as $F(R) = (1-R)^2/(2R)$, R = reflectance).

Raman spectra were collected with a Renishaw Raman system (Type 1000, dispersive spectrometer) equipped with CCD detector and a Leica microscope DM LM. The excitation wavelength of 514 nm was generated by a multi-line Ar-ion gas laser (Stellar-Pro Select 150 of MODU-Laser) operating at 20 mW. The wavenumber accuracy was within 1 cm^{-1} . Materials sulfided at 20 bar were transferred to a flow quartz cell and treated in situ under flowing $\text{H}_2\text{S}/\text{H}_2$ (10 vol.% H_2S) at 523 K for 1 h. The spectra were recorded after cooling to 303 K. After recording the Raman spectra of the freshly sulfided materials, 10 vol.% NO/He was admitted into the cell and additional spectra were recorded under in situ conditions for selected samples.

Infrared spectroscopy with adsorption of probe molecules was performed on a Nicolet 6700 FT-IR spectrometer with a resolution of 4 cm^{-1} . Prior to the adsorption experiments, the oxide precursors were diluted with $\gamma\text{-Al}_2\text{O}_3$ (weight ratio of 1:3), ground, and pressed into self-supporting wafers (ca. 4 mg cm^{-2}). Each wafer was placed into an IR cell and treated at 573 K for 1 h (temperature ramp of 5 K min^{-1}) under vacuum (10^{-8} mbar). Afterwards, in situ sulfidation of the sample was performed at 20 bar and 673 K for 2 h in a flow of 10 vol.% H_2S in H_2 (20 ml min^{-1}). The sulfidation was followed by flushing with a He flow (20 ml min^{-1}) for 10 min and evacuation at 10^{-8} mbar .

After the thermal treatment and sulfidation of the pellet, NO adsorption was performed at 303 K by dosing NO (10 vol.% NO/He) into the IR cell up to an equilibrium pressure of 1 mbar. A series of spectra were recorded while NO was being admitted into the cell. The spectra were background subtracted and analyzed by deconvolution with the software GRAMS.

The adsorption of 2,6-dimethylpyridine (DMP, Aldrich, $\geq 99.0\%$) on the Ni-WS₂/ γ -Al₂O₃ catalysts was followed by IR spectroscopy after the sulfidation procedure described above. Small doses of DMP were admitted to the cell at 323 K, up to the equilibrium pressure of 0.5 mbar. Evacuation under 10^{-3} mbar was performed for 10 min before recording the spectra. 1 mbar of H₂S or 1 bar of H₂ was dosed to the cell and another set of spectra was collected. The intensities of the bands were quantitatively determined using the software OMNIC while the concentrations of protonated DMP were calculated using the molar extinction coefficient $\epsilon_{\nu_{8a}} = 6.5 \text{ cm} \mu\text{mol}^{-1}$ for the band at around 1625 cm⁻¹.²⁶

Adsorption of pyridine (Aldrich, $\geq 99.0\%$) on the sulfide catalysts was followed by IR spectroscopy. At 323 K, pyridine was admitted to the cell at an equilibrium pressure of up to 0.5 mbar for 30 min (after in situ sulfidation). Evacuation was applied under 10^{-7} mbar for 30 min, and a spectrum was recorded. Desorption of pyridine was performed by increasing temperature (up to 623 K with 50 K per step) with evacuation after each step before a spectrum was taken. The obtained spectra were analyzed by OMNIC software to quantify the intensities of the bands. The concentrations of coordinating pyridine were calculated using the molar extinction coefficient $0.73 \text{ cm} \mu\text{mol}^{-1}$ determined for the characteristic band at ca. 1450 cm⁻¹.

2.2.3 Kinetic Measurements

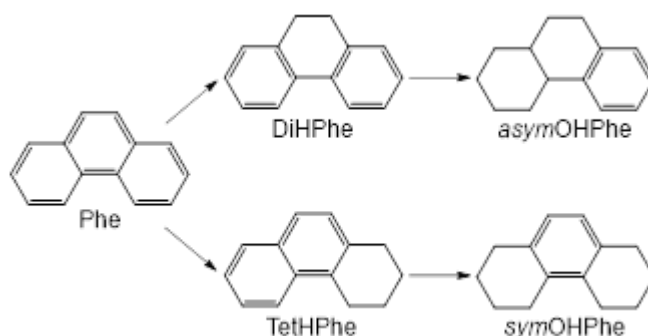
The hydrogenation of phenanthrene was performed in a continuous-flow trickle bed reactor (glass-coated stainless-steel tube with 6 mm inner diameter) with gas and liquid feeds supplied by high-pressure mass flow controllers (Bronkhorst EL-FLOW) and a HPLC pump (Gilson 307), respectively. Prior to each run, the catalyst precursor (30 mg, 250-355 μm) was diluted with SiC (600 mg, 63-90 μm) and placed in the isothermal region of the reactor. The catalyst bed was held in place by filling the reactor volume with SiC. Sulfidation of the oxide precursor was performed in a H₂S/H₂ gas mixture (20 ml min⁻¹, 10 vol.% H₂S) at 20 bar and 673 K. Catalytic tests were performed at 573 K, 60 bar, and a H₂/hydrocarbon volumetric ratio of 300. The space time, defined as $m_{\text{cat}}/F_{\text{Phe}}$ (m_{cat} : weight of the catalyst; F_{Phe} : molar flow of phenanthrene), was varied by changing the flow rates of gas and liquid feeds. The reactant solution was prepared with 1 wt.% of phenanthrene (Alfa Aesar, 98%), 1000 ppm of S (as dimethyl disulfide, Aldrich $\geq 99.0\%$), and 2 wt.% of n-tetradecane (Alfa Aesar, $\geq 99\%$) in decahydronaphthalene (Merck Millipore, 98%). Liquid samples were collected with a multiport sampling valve and analyzed offline by a Shimadzu 2010 GC equipped with a HP-5 capillary column. Kinetic analysis was performed for data acquired after 20 h time on stream when steady

state had been reached. Preliminary tests using varying particle sizes and catalyst amounts allowed ruling out transport artifacts at the applied conditions.

2.3 Results and Discussion

All catalysts used in this study were prepared by incipient wetness impregnation followed by consecutive thermal treatment in synthetic air and sulfiding the oxidic catalyst precursor with H₂S/H₂ mixtures in a continuous flow trickle bed reactor (results from elemental analysis are provided in Table 2.2 in Supporting Information). The as-sulfided samples are denoted as **MS**₂/γ-Al₂O₃ and Ni(*x*)**MS**₂/γ-Al₂O₃ with **M** being Mo, W or a mix of Mo and W, and *x* being the measured concentration of Ni in wt. %. Extensive characterization data for WS₂/Al₂O₃, the corresponding Ni-promoted series and the trimetallic sulfide are presented in the Supporting Information, while those for Ni-MoS₂/γ-Al₂O₃ samples have been previously published.²⁴ Importantly, the dimensions and characteristic properties of these γ-Al₂O₃-supported sulfides were largely similar. The most significant trend is a 10-40% decrease in average slab diameter with increasing Ni concentrations (0.5-11.1 wt.%) compared to the unpromoted catalysts (see slab diameter, stacking degree and dispersion factor *f*_W or *f*_{Mo} in Table 2.2 in SI). Overall, these samples span a wide range of Ni (0.05-1.9 mmol g⁻¹), Mo (0.4-1.0 mmol g⁻¹) and W loadings (0.4-1.1 mmol g⁻¹).

Only four products were detected with all studied sulfide catalysts at low to moderate conversions of PHE (1-25%), i.e., 9,10-dihydrophenanthrene (DiHPhe), 1,2,3,4-tetrahydrophenanthrene (TetHPhe), 1,2,3,4,5,6,7,8-octahydrophenanthrene (symOHPhe), and 1,2,3,4,4a,9,10,10a-octahydrophenanthrene (asymOHPhe). The latter two products are nearly absent on WS₂/γ-Al₂O₃ (Figure 2.11 in SI) and MoS₂/γ-Al₂O₃^{23,24} under these operating conditions. The PHE conversion as a function of space time, as well as the yields and selectivities of the four products as a function of PHE conversion, are shown in Figure 2.10 and Figure 2.11 in SI. With Ni-promoted catalysts, the decrease in the selectivities to DiHPhe and TetHPhe mirrored the increase in selectivities to asymOHPhe and symOHPhe as the contact time increased. Thus, these data point to a reaction network which is composed of two parallel routes, i.e., initial hydrogenation at the middle ring (PHE → DiHPHE → asymOHPHE) and initial hydrogenation at a lateral ring (PHE → TetHPhe → symOHPhe), as shown in Scheme 2.1. The dehydrogenation of DiHPhe to PHE and its hydrogenation to TetHPhe are not evident, but were demonstrated for the same reaction catalyzed by Ni-MoS₂/γ-Al₂O₃.^{23,24} At low conversions, both DiHPhe reactions can be neglected.²⁴



Scheme 2.1. Reaction network for hydrogenation of Phenanthrene. ^{22,23,27,28}

Table 2.1. Mass specific rates (extrapolated to zero contact time) of PHE conversion via initial hydrogenation at the middle ring and at a lateral ring (denoted in the Table as r_1 and r_2 , respectively) on γ - Al_2O_3 -supported sulfide catalysts. All catalysts are supported on γ - Al_2O_3 . Data for MoS_2 -based catalysts are taken from ref.²⁴.

Catalyst	Ni/(Ni+M) molar ratio	r_1 ($10^{-3} \text{ mol h}^{-1} \text{ g}_{\text{cat}}^{-1}$)	r_2 ($10^{-3} \text{ mol h}^{-1} \text{ g}_{\text{cat}}^{-1}$)
WS_2	0	0.40	0.06
Ni(0.3) WS_2	0.05	0.67	0.16
Ni(1.1) WS_2	0.14	1.48	1.47
Ni(2.2) WS_2	0.25	1.78	1.78
Ni(3.2) WS_2	0.33	1.66	1.66
Ni(4.5) WS_2	0.41	1.61	1.61
Ni(7.8) WS_2	0.55	1.39	1.55
Ni(11.1) WS_2	0.67	1.21	1.35
WS_2 -a	0	0.20	0.04
WS_2 -b	0	0.30	0.05
Ni(2.5) MoWS_2	0.34	1.53	1.57
MoS_2	0	0.52	0.06
Ni(1.3) MoS_2	0.19	0.66	0.47
Ni(2.7) MoS_2	0.33	0.78	0.76
Ni(8.8) MoS_2	0.62	0.55	0.53

Compared to $\text{WS}_2/\gamma\text{-Al}_2\text{O}_3$, the mass specific rates of PHE hydrogenation increased by a factor of 4.4 for the $\text{PHE} \rightarrow \text{DiHPhe} \rightarrow \text{asymOHPhe}$ route (r_1), and 32 for the $\text{PHE} \rightarrow \text{TethPhe} \rightarrow \text{symOHPhe}$ route (r_2) on the most active Ni(2.2) $\text{WS}_2/\gamma\text{-Al}_2\text{O}_3$ with a

Ni/(Ni+W) ratio of 0.25 (Table 2.1). Higher Ni contents led to reduced promotional effects, which is attributed to the increasing presence of catalytically inactive NiS_x (the mass specific activity of $\text{NiS}_x/\gamma\text{-Al}_2\text{O}_3$ was at least two orders of magnitude lower than the unpromoted $\text{MoS}_2/\gamma\text{-Al}_2\text{O}_3$ and $\text{WS}_2/\gamma\text{-Al}_2\text{O}_3$ under identical conditions). The ratios of the initial rates along the two reaction routes changed drastically with the addition of Ni, from hydrogenation at the middle ring being the dominant route on $\text{WS}_2/\gamma\text{-Al}_2\text{O}_3$ to equivalent middle and lateral ring hydrogenation, on all Ni-promoted catalysts except $\text{Ni}(0.3)\text{WS}_2/\gamma\text{-Al}_2\text{O}_3$ (Table 2.1). The product distribution and residence time effects hardly changed at Ni/(Ni+W) atomic ratios ≥ 0.14 (Figure 2.12 in SI).

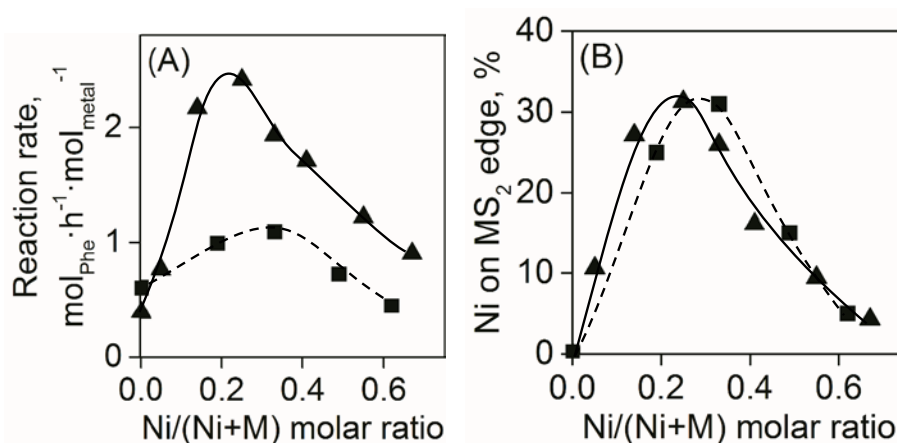


Figure 2.1. (A) Rates of phenanthrene (PHE) hydrogenation on unpromoted and Ni-promoted WS_2 - (▲) and MoS_2 -based (■) catalysts as a function of Ni/(M+Ni) ratio where M = Mo or W. Reaction conditions: 573 K, 60 bar total pressure, and a H_2/HC ratio (v/v) of 300. Note that the rates reported have been normalized to the total metal content. (B) Percentage of Ni substitution at the slab edge of $\text{Ni-WS}_2/\gamma\text{-Al}_2\text{O}_3$ (▲) and $\text{Ni-MoS}_2/\gamma\text{-Al}_2\text{O}_3$ (■) with increasing Ni content. The data of MoS_2 -based catalysts are taken from ref.²⁴. See details for the calculation of Ni substitution degree in the SI.

It is instructive to compare the impact of Ni promotion on the hydrogenation rates on WS_2 - and MoS_2 -based catalysts. Noting that non-promoted $\text{WS}_2/\gamma\text{-Al}_2\text{O}_3$ and $\text{MoS}_2/\gamma\text{-Al}_2\text{O}_3$ have similar hydrogenation activities (normalized to metal content), Figure 2.1(A) clearly shows that the effect of Ni promotion is significantly more pronounced on WS_2 -based catalysts. For example, a Ni-promoted $\text{WS}_2/\gamma\text{-Al}_2\text{O}_3$ catalyst with the greatest promotion effect (Ni/(Ni+W) ~ 0.25) was 2.2 times as active as the most active Ni- $\text{MoS}_2/\gamma\text{-Al}_2\text{O}_3$ catalyst (Ni/(Ni+Mo) ~ 0.3). Despite the difference in rates, the selectivities towards different products were very similar over most sulfide catalysts with the notable exception of the lowest Ni-loaded sample. The ratio of the two hydrogenation routes decreased as the Ni/(Ni+M) ratio increased and approached unity at higher ratios on both series of catalysts. Additionally, the apparent activation energy measured on

Ni(2.2)WS₂/γ-Al₂O₃ was 127 kJ mol⁻¹, identical to that (126 kJ mol⁻¹) obtained on Ni(2.7)MoS₂/γ-Al₂O₃ under the same conditions (Figure 2.13 in SI). Together, these observations point to variations in the concentrations of active sites having identical intrinsic activity for PHE hydrogenation on the two series of materials, reminiscent of that suggested for thiophene HDS on carbon-supported Ni-W and Ni-Mo catalysts.²²

Establishing structure-function relations requires reliable quantification of the accessible functional sites (e.g., edge vacancies and SH groups). In particular, NO adsorption has been used to estimate the concentration of active metal sulfide edges.^{5,29–32} Since NO is adsorbed on both unpromoted and promoted edges (those exposing S-vacancies), spectroscopic discrimination of the adsorption sites is necessary.²⁹ NO adsorbed on NiS_x/γ-Al₂O₃ produced a main IR band at ~1830 cm⁻¹ (Figure 2.2(A)), which was attributed to NO on Ni²⁺ in NiS_x.²⁹ For NO on WS₂/γ-Al₂O₃, the two main bands at 1695 and 1775 cm⁻¹ are attributed to the symmetric and asymmetric stretching vibrations of dinitrosyl species on W⁴⁺ at the edges of WS₂ (Figure 2.2(A)).²⁹ In addition to the bands associated with WS₂ and NiS_x (see Figure 2.18 for more spectra at NO pressures of 10⁻³–1 mbar and Figure 2.19 for the corresponding deconvoluted spectra, both in SI), a shoulder at 1875 cm⁻¹ emerged in the spectra of the Ni-promoted WS₂ catalysts. This band has been attributed either to partially sulfided Ni vicinal to an oxidic W phase,³³ or to dispersed Ni²⁺ ions in the sulfide.³⁴ Taking into account the rapid oxidation-reconstruction^{35–38} of the Ni-promoted phase by NO (but not the unpromoted WS₂, see Figure 2.15 in SI) and the IR bands of NO adsorbed on the oxide precursors (Figure 2.7 in SI) and sulfide catalysts, we attribute the band at 1875 cm⁻¹ to NO adsorbed on Ni²⁺ cations embedded in the perimeter of the WS₂ slab. It appears that these sites are transformed to oxidic W species formed upon the interaction of NO. The integrated area of this band increased first with Ni concentration, reaching a maximum on Ni(2.2)WS₂/γ-Al₂O₃ with a Ni/(Ni+W) ratio of 0.22, whereas the integrated areas of the bands at 1695 and 1775 cm⁻¹ (NO on WS₂) steadily decreased (Figure 2.2). The band at 1830 cm⁻¹ (NO on NiS_x) also increased with the Ni concentration, suggesting that the concentration of NiS_x increased (Figure 2.20 in SI). Because the intensity at 1875 cm⁻¹ dropped rapidly after reaching the maximum (Figure 2.2(B)), NiS_x clusters are speculated to form at edge sites and block the access to Ni²⁺. This implies that the maximum absorbance observed here was already attenuated from the real maximum, attained only if the site-blocking NiS_x were entirely absent.

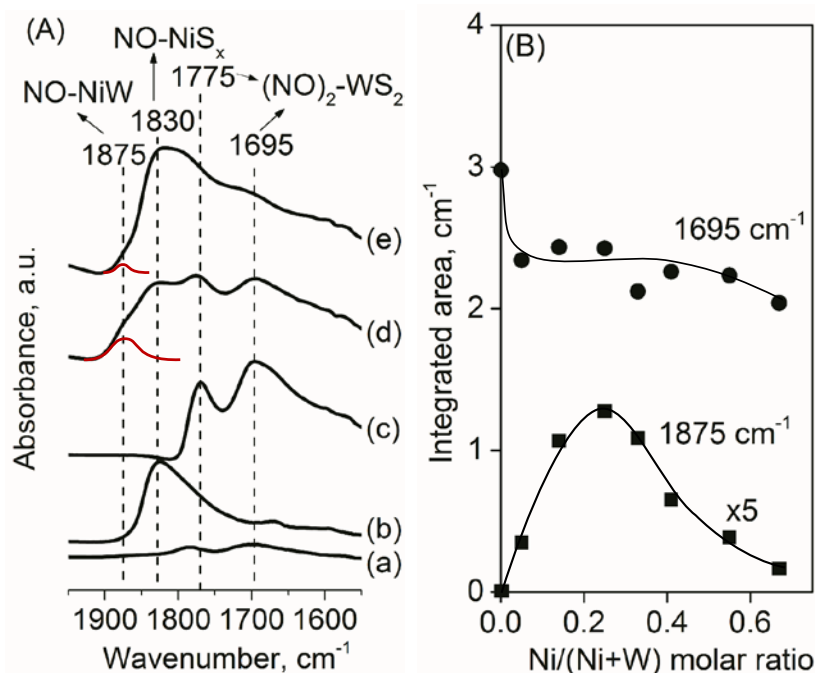


Figure 2.2. (A) Background-corrected infrared spectra of NO adsorbed on (a) $\gamma\text{-Al}_2\text{O}_3$, (b) $\text{NiS}_x/\gamma\text{-Al}_2\text{O}_3$, (c) $\text{WS}_2/\gamma\text{-Al}_2\text{O}_3$, (d) $\text{Ni}(2.2)\text{WS}_2/\gamma\text{-Al}_2\text{O}_3$, (e) $\text{Ni}(11.1)\text{WS}_2/\gamma\text{-Al}_2\text{O}_3$. (B) Integrated areas of the deconvoluted bands at 1875 cm^{-1} (i.e., NO adsorbed on oxidized Ni-promoted edge sites; the deconvoluted band is marked in red in (A)) and at 1695 cm^{-1} (i.e., NO adsorbed on non-promoted sites) as a function of the molar ratio of Ni/(Ni+W). The continuous line in (B) represents a trend. See Figure 2.18 for a full set of IR spectra and Figure 2.20 for the changes of integrated areas of other bands as a function of Ni/(Ni+W) ratio.

Figure 2.1(B) shows the percentage of Ni substitution at the WS_2 edge (e.g., Ni-S-W), calculated from the integrated area of 1875 cm^{-1} band and the estimated molar extinction coefficient ($\sim 1.0 \text{ cm } \mu\text{mol}^{-1}$) of NO adsorbed at the Ni-substituted W-edge sites (see Section 2.6.6, Supporting Information, for details of calculation and assumptions made). Also presented is the percentage of Ni substitution as a function of the bulk Ni/(Ni+Mo) ratio for MoS_2 -based samples as determined previously.²⁴ Interestingly, the degree of Ni substitution at both MoS_2 and WS_2 slab edges was quite similar for any given Ni/(Ni+M) ratio. Consequently, the similar slab sizes and dispersions as well as the similar Ni substitution degrees for WS_2 - and MoS_2 -based catalysts would imply similar concentrations of such Ni-associated edge sites for the two sets of catalysts.

Sulfhydryl groups can be formed at or near edge vacancies by dissociative adsorption of H_2 and H_2S . While these SH groups are Brønsted acidic, they are involved in hydrogen addition reactions.¹¹ In order to quantify the concentration of Brønsted (BAS) and Lewis acid sites (LAS), we studied the IR spectra of adsorbed pyridine and 2,6-dimethylpyridine (DMP). Pyridine adsorption on BAS of a sulfide surface generates rather

unstable pyridinium ions,^{39–41} often making their concentration undetectably low and unreliable for quantification. In contrast, the higher base strength of DMP suffices to probe the weak BAS, but produces bands that do not correspond solely to adsorption on LAS (i.e., bands overlap those of physisorbed DMP and H-bonded species). Thus, for quantification of BAS and LAS we combined information from DMP and pyridine, respectively (Section 2.6.5, Supporting Information).

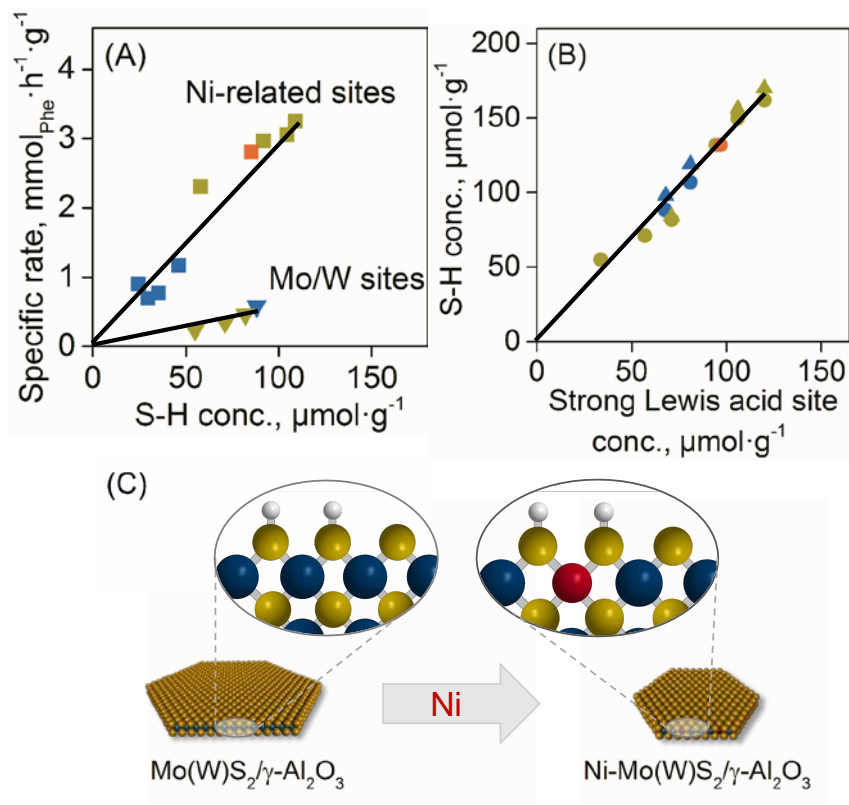


Figure 2.3. (A) Correlation between corrected reaction rates and SH concentrations (see Table 2.5 for tabulated values), with non-promoted MoS₂ or WS₂ labelled by ▼, and ■ for Ni-promoted phases. (B) Correlation between total SH concentration (associated with both Mo/W and Ni sites at the slab edge) and concentration of pyridine adsorbed on strong Lewis acid sites (10⁻⁷ mbar and 623 K). Blue: MoS₂-based catalysts; Orange: Ni-MoWS₂; green: WS₂-based catalysts (▲: SH concentration measured after adsorption of H₂S, ●: SH concentration measured after adsorption of H₂). Lines represent trends. The data measured for MoS₂-based catalysts are taken from Refs.^{24,26}. (C) Illustration of the proposed site structure after H₂ or H₂S dissociation for Mo(W)S₂ and Ni-Mo(W)S₂ slabs (note the size reduction after Ni incorporation based on our experimental data). Grey: H; yellow: S; blue: Mo or W; red: Ni.

DMP adsorbed and protonated on SH groups give rise to bands at 1650 and 1627 cm⁻¹.^{42,43} Deconvoluted spectra of DMP adsorbed on WS₂/γ-Al₂O₃ and Ni(x)WS₂/γ-Al₂O₃ are shown in Figures 2.21 and 2.22 in SI. Exposing the DMP-saturated catalyst to H₂S

and H₂ (1 mbar or 1 bar at equilibrium, respectively) increased the intensity of the bands of protonated DMP and concomitantly decreased the intensity of the bands at 1615 and 1580 cm⁻¹ for DMP on LAS. For both adsorbates, the increase in the SH group concentration (ΔC_{SH}) was most pronounced for Ni(2.2)WS₂/ γ -Al₂O₃. This sample also showed the highest concentration of accessible Ni-substituted edge sites. On Ni(11.1)WS₂/ γ -Al₂O₃, the increase in the concentration of SH was the smallest ($\Delta C_{\text{SH}} = 11$ and 7 $\mu\text{mol g}^{-1}$ for the two adsorbates), in parallel with the lowest concentration of accessible edge-embedded Ni (Figure 2.2(B)).

In comparison to WS₂-based catalysts, the Ni-MoS₂ series showed much smaller increase in SH concentration after adsorption/dissociation of H₂S or H₂ at the same conditions as applied here, but the trend with respect to Ni loading was similar. For example, after co-adsorption of H₂S, Ni(2.2)WS₂/ γ -Al₂O₃ showed a SH concentration of 170 $\mu\text{mol g}_{\text{cat}}^{-1}$, which was higher than that of Ni(2.7)MoS₂/ γ -Al₂O₃ (119 $\mu\text{mol g}_{\text{cat}}^{-1}$).²⁶ Similarly, after co-adsorption of H₂, Ni(2.2)WS₂/ γ -Al₂O₃ showed a SH concentration of 162 $\mu\text{mol g}_{\text{cat}}^{-1}$, also higher than that of Ni(2.7)MoS₂/ γ -Al₂O₃ (107 $\mu\text{mol g}_{\text{cat}}^{-1}$).²⁶ The much higher concentration of sulfhydryl groups with the Ni-WS₂ (than for Ni-MoS₂) is hypothesized to reflect a higher concentration of CUS (which are LAS by definition) responsible for the formation of SH groups upon H₂ and H₂S dissociative adsorption. Indeed, a linear correlation is observed between the concentration of SH groups and that the concentration of strong LAS (Figure 2.3(B)). The higher the concentration of strong LAS, the higher the SH concentration at the edges of Ni-WS₂ than Ni-MoS₂. This shows a relation between (a fraction of) accessible cations and the SH at the edge of the sulfide slab, pointing to a well-defined site, rather than to two independent variables, i.e., the LAS and the SH concentration. An illustration of the proposed site structure is shown in Figure 2.3(C).

The observed difference in SH concentration parallels the higher hydrogenation activity of supported Ni-WS₂ than Ni-MoS₂. To characterize the intrinsic activity of the Ni-promoted edge sites, the reaction rate of the Ni-promoted **MS**₂ phase was corrected by subtracting the contribution of non-promoted **MS**₂ sites. Similarly, the concentration of SH groups on the promoted phases was corrected by subtracting those associated with unpromoted **MS**₂.

A linear correlation between the reaction rates and SH concentrations was observed (Figure 2.3(A)), including SH groups on mono-, bi- and trimetallic sulfides. Non-promoted WS₂ and MoS₂ exhibit a similar rate dependence on the SH concentration (or

the strong LAS concentration), yet significantly lower than that measured on the corresponding promoted series (square symbols). These interdependencies indicate that the rate of PHE hydrogenation depends only on the concentration of LAS, which in turn determine the SH group concentration associated with the non-promoted and Ni-promoted phases. It is independent of the primary sulfide phase, i.e., the SH groups associated with Ni²⁺-decorated slab edge lead to identical intrinsic rates on Ni-WS₂ or Ni-MoS₂. While turnover frequencies (TOFs) for PHE hydrogenation over each SH on Ni-promoted phase and non-promoted MS₂ phase could be estimated (40 vs. 6 h⁻¹) from the slopes in Figure 2.3(A), it should be added that the concentration of SH at reaction conditions might be different from those determined in the spectroscopic cell at lower temperatures and pressures.

2.4 Conclusion

In summary, the unequivocal structure-activity relation established for aromatics hydrogenation pinpoints the direct role of sulfhydryl groups as the sites that lead to H-addition. The results show that the SH groups vicinal to edge-decorated Ni are much more reactive than SH associated with non-promoted sites. This leads to higher hydrogen addition rates as well as a much greater extent of enhancement on hydrogenation of one of the lateral rings in phenanthrene. These reactive species exhibit the same intrinsic activity and selectivity in hydrogenation, regardless of the slab composition (MoS₂, WS₂ or mixed MoWS₂). Our results on phenanthrene hydrogenation show that the higher activity of Ni-WS₂ primarily results from its higher concentration of SH groups, which is in turn related to an inherently higher concentration of strong Lewis acid sites on Ni-WS₂ than on Ni-MoS₂, but not to the intrinsic rate constant for the rate-determining H-addition. This study not only provides an answer to the question as to why Ni-promoted WS₂ manifests itself as a better hydrogenation catalyst in general than the MoS₂-based counterpart, but should also enable a more rigorous comparison of intrinsic activities among different transition metal sulfides in their supported or even unsupported forms.

2.5 References

- (1) Topsøe, H.; Clausen, B. S.; Massoth, F. E. *Hydrotreating catalysis*; Springer, 1996.
- (2) Scott, C. E.; Perez-Zurita, M. J.; Carbognani, L. a.; Molero, H.; Vitale, G.; Guzmán, H. J.; Pereira-Almao, P. *Catal. Today* **2015**, *250*, 21–27.
- (3) Eijsbouts, S. *Appl. Catal. A Gen.* **1997**, *158* (1), 53–92.
- (4) Lauritsen, J. V.; Kibsgaard, J.; Olesen, G. H.; Moses, P. G.; Hinnemann, B.; Helveg, S.; Nørskov, J. K.; Clausen, B. S.; Topsøe, H.; Lægsgaard, E.; Besenbacher, F. *J. Catal.* **2007**, *249* (2), 220–233.
- (5) Gutiérrez, O. Y.; Singh, S.; Schachtl, E.; Kim, J.; Kondratieva, E.; Hein, J.; Lercher, J. A.; Han, W.; Nie, H.; Long, X.; Li, M.; Yang, Q.; Li, D. *ACS Catal.* **2014**, *4* (5), 1487–1499.
- (6) Hensen, E. J. M.; van der Meer, Y.; van Veen, J. A. R.; Niemantsverdriet, J. W. *Appl. Catal. A Gen.* **2007**, *322* (0), 16–32.
- (7) Zuo, D.; Vrinat, M.; Nie, H.; Maugé, F.; Shi, Y.; Lacroix, M.; Li, D. *Catal. today* **2004**, *93*, 751–760.
- (8) Voorhoeve, R. J. H.; Stuiver, J. C. M. *J. Catal.* **1971**, *23* (2), 228–235.
- (9) Scheffer, B.; Mangnus, P. J.; Moulijn, J. a. *J. Catal.* **1990**, *121* (1), 18–30.
- (10) Stanislaus, a.; Cooper, B. *Catal. Rev.* **1994**, *36* (May 2013), 75–123.
- (11) Reinhoudt, H. R.; van Langeveld, a. D.; Kooyman, P. J.; Stockmann, R. M.; Prins, R.; Zandbergen, H. W.; Moulijn, J. a. *J. Catal.* **1998**, *179* (2), 443–450.
- (12) Kelly, S. D.; Yang, N.; Mickelson, G. E.; Greenlay, N.; Karapetrova, E.; Sinkler, W.; Bare, S. R. *J. Catal.* **2009**, *263* (1), 16–33.
- (13) Bensch, W. *Hydrotreating: Removal of Sulfur from Crude Oil Fractions with Sulfide Catalysts*; Elsevier Ltd., 2013; Vol. 7.
- (14) Alphazan, T.; Bonduelle-Skrzypczak, A.; Legens, C.; Boudene, Z.; Taleb, A.-L.; Gay, A.-S.; Ersen, O.; Copéret, C.; Raybaud, P. *J. Catal.* **2016**, *340*, 60–65.

- (15) Wang, H.; Dai, F.; Li, Z.; Li, C. *Energy & Fuels* **2015**, *29* (8), 4902–4910.
- (16) Romero, C. M. C.; Thybaut, J. W.; Marin, G. B. *Catal. Today* **2008**, *130* (1), 231–242.
- (17) Shin, J.; Oh, Y.; Choi, Y.; Lee, J.; Lee, J. K. *Appl. Catal. A Gen.* **2017**, *547*, 12–21.
- (18) Choi, Y.; Lee, J.; Shin, J.; Lee, S.; Kim, D.; Lee, J. K. *Appl. Catal. A Gen.* **2015**, *492*, 140–150.
- (19) Prins, R.; De Beer, V. H. J.; Somorjai, G. a. *Catal. Rev.* **1989**, *31* (1–2), 1–41.
- (20) Byskov, L. S.; Nørskov, J. K.; Clausen, B. S.; Topsøe, H. *J. Catal.* **1999**, *187*, 109–122.
- (21) Zhu, Y.; Ramasse, Q. M.; Brorson, M.; Moses, P. G.; Hansen, L. P.; Kisielowski, C. F.; Helveg, S. *Angew. Chem., Int. Ed.* **2014**, *53*, 10723.
- (22) Korre, S. C.; Klein, M. T.; Quann, R. J. *Ind. Eng. Chem. Res.* **1995**, *34* (1), 101–117.
- (23) Schachtl, E.; Yoo, J. S.; Gutiérrez, O. Y.; Studt, F.; Lercher, J. A. *J. Catal.* **2017**, *352*, 171–181.
- (24) Schachtl, E.; Zhong, L.; Kondratieva, E.; Hein, J.; Gutiérrez, O. Y.; Jentys, A.; Lercher, J. A. *ChemCatChem* **2015**, *7* (24), 4118–4130.
- (25) Hensen, E. J. M. J. M.; Kooyman, P. J. J.; van der Meer, Y.; a.M. van der Kraan; de Beer, V. H. J. H. J.; van Veen, J. a. R.; van Santen, R. a.; van der Kraan, A. M.; de Beer, V. H. J. H. J.; van Veen, J. a. R.; van Santen, R. a. *J. Catal.* **2001**, *199* (2), 224–235.
- (26) Schachtl, E.; Kondratieva, E.; Gutiérrez, O. Y.; Lercher, J. A. *J. Phys. Chem. Lett.* **2015**, *6* (15), 2929–2932.
- (27) Shabtai, J.; Veluswamy, L.; Oblad, A. G. *Am. Chem. Soc. Div. Fuel Chem, Prepr.* **1978**, *23* (1), 107.
- (28) Lemberon, J.-L.; Guisnet, M. *Appl. Catal.* **1984**, *13* (1), 181–192.
- (29) Topsøe, N.-Y.; Topsøe, H. *J. Catal.* **1983**, *84* (2), 386–401.

- (30) Topsøe, N. Y.; Tuxen, A.; Hinnemann, B.; Lauritsen, J. V.; Knudsen, K. G.; Besenbacher, F.; Topsøe, H. *J. Catal.* **2011**, *279*, 337–351.
- (31) Gutiérrez, O. Y.; Klimova, T. *J. Catal.* **2011**, *281* (1), 50–62.
- (32) Hrabar, A.; Hein, J.; Gutiérrez, O. Y.; Lercher, J. A. *J. Catal.* **2011**, *281* (2), 325–338.
- (33) Reinhoudt, H. R.; Crezee, E.; a.D. van Langeveld; Kooyman, P. J.; van Veen, J. a. R.; Moulijn, J. a. *J. Catal.* **2000**, *196* (2), 315–329.
- (34) Atanasova, P.; Agudo, A. L.; López Agudo, A. *Appl. Catal. B Environ.* **1995**, *5* (4), 329–341.
- (35) Nielsen, L. P.; Ibsen, L.; Christensen, S. V; Clausen, B. S. *J. Mol. Catal. A Chem.* **2000**, *162* (1–2), 367–371.
- (36) Okamoto, Y.; Kawano, M.; Kubota, T. *Chem. Commun.* **2003**, No. 9, 1086–1087.
- (37) Shuxian, Z.; Hall, W. K.; Ertl, G.; Knözinger, H. *J. Catal.* **1986**, *100* (1), 167–175.
- (38) Caron, F.; Rivallan, M.; Humbert, S.; Daudin, A.; Bordiga, S.; Raybaud, P. *J. Catal.* **2018**, *361*, 62–72.
- (39) Ratnasamy, P.; Knözinger, H. *J. Catal.* **1978**, *54* (2), 155–165.
- (40) Riseman, S. M.; Bandyopadhyay, S.; Massoth, F. E.; Eyring, E. M. *Appl. Catal.* **1985**, *16* (1), 29–37.
- (41) Breysse, M.; Berhault, G.; Kasztelan, S.; Lacroix, M.; Maugé, F.; Perot, G. *Catal. Today* **2001**, *66* (1), 15–22.
- (42) Berhault, G.; Lacroix, M.; Breysse, M.; Mauge, F.; Lavalley, J. C.; Nie, H.; Qu, L. L. *J. Catal.* **1998**, *178*, 555–565.
- (43) Rocha, A. S.; Faro Jr, A. C.; Oliviero, L.; Van Gestel, J.; Maugé, F. *J. Catal.* **2007**, *252* (2), 321–334.

2.6 Supporting Information

2.6.1 Characterization Results of the Oxide Precursors

The metal contents of all materials were provided in wt.% and mmol g⁻¹ in Table 2.2 with molar Ni/(W+Ni) ratios ranging from 0 to 0.67. Compared to the parent support, the deposition of W and Ni decreased the surface area and pore volume due to increase in density as shown in Table 2.3. The density of metal per surface area was 3.7 - 4.0 W atoms and up to 8.1 Ni atoms per nm².

Table 2.2. Metal content and molar Ni/(W+Ni) ratio the oxide precursors.

Catalyst	Metal content, wt.-% (mmol g ⁻¹)		Ni/(W+Ni) mol/mol
	W	Ni	
γ -Al ₂ O ₃	-	-	-
NiO/ γ -Al ₂ O ₃	-	5.8 (0.97)	-
WO ₃ / γ -Al ₂ O ₃	21.9 (1.1)	-	0
WO ₃ / γ -Al ₂ O ₃ -a	8.5 (0.4)	-	0
WO ₃ / γ -Al ₂ O ₃ -b	16.8 (0.9)	-	0
Ni(0.3)WO ₃ / γ -Al ₂ O ₃	19.0 (1.0)	0.3 (0.05)	0.05
Ni(1.1)WO ₃ / γ -Al ₂ O ₃	21.6 (1.1)	1.5 (0.19)	0.14
Ni(2.2)WO ₃ / γ -Al ₂ O ₃	20.2 (1.1)	2.2 (0.37)	0.25
Ni(3.2)WO ₃ / γ -Al ₂ O ₃	21.2 (1.1)	3.3 (0.56)	0.33
Ni(4.5)WO ₃ / γ -Al ₂ O ₃	20.3 (1.1)	4.5 (0.77)	0.41
Ni(7.8)WO ₃ / γ -Al ₂ O ₃	19.9 (1.1)	7.8 (1.33)	0.55
Ni(11.1)WO ₃ / γ -Al ₂ O ₃	17.2 (1.0)	11.1 (1.89)	0.67

Table 2.3. Concentration of impregnated metals on γ -Al₂O₃ for all the oxide precursors of the investigated catalysts.

Catalyst	W, atoms/nm ²	Ni, atoms/nm ²	Total metal, atoms /nm ²	Pore vol- ume, cm ³ /g
NiO/ γ -Al ₂ O ₃	0	2.8	2.8	0.67
WO ₃ / γ -Al ₂ O ₃	4.0	0	4.0	0.58
Ni(0.3)WO ₃ / γ -Al ₂ O ₃	3.9	0.2	4.1	0.45
Ni(1.1)WO ₃ / γ -Al ₂ O ₃	4.5	0.7	5.2	0.44
Ni(2.2)WO ₃ / γ -Al ₂ O ₃	3.6	1.2	4.9	0.43
Ni(3.2)WO ₃ / γ -Al ₂ O ₃	4.3	2.1	6.4	0.44
Ni(4.5)WO ₃ / γ -Al ₂ O ₃	3.9	2.7	6.6	0.42
Ni(7.8)WO ₃ / γ -Al ₂ O ₃	4.3	5.2	9.5	0.42
Ni(11.1)WO ₃ / γ -Al ₂ O ₃	4.0	8.1	12.2	0.37

The X-ray diffractograms (Figure 2.4) show that, besides the reflections of γ -Al₂O₃ at 37.5 °2 θ , 46°2 θ , and 67 °2 θ , all W-containing oxide precursors exhibited reflections at

24 °2 θ , and 33 °2 θ corresponding to WO₃ (JCPDS file No.20-1323). These reflections were weak and broad, which points to low crystallinity. Reflections assigned to NiO (JCPDS file No.01-1239) were present only for Ni(7.8)WO₃/ γ -Al₂O₃, and Ni(11.1)WO₃/ γ -Al₂O₃. Influence of Ni on the dispersion of WO₃ species was not evident by XRD.

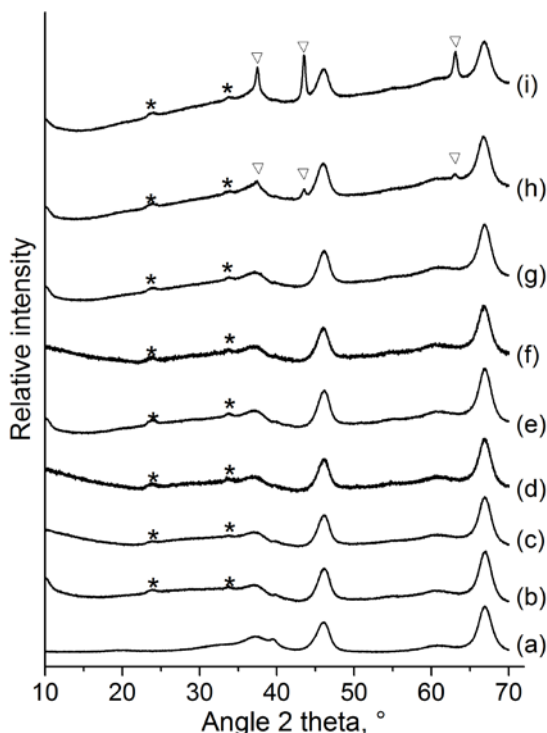


Figure 2.4. X-ray diffraction patterns of the support and the oxide precursors: (a) γ -Al₂O₃, (b) WO₃/ γ -Al₂O₃, (c) Ni(0.3)WO₃/ γ -Al₂O₃, (d) Ni(1.1)WO₃/ γ -Al₂O₃, (e) Ni(2.2)WO₃/ γ -Al₂O₃, (f) Ni(3.2)WO₃/ γ -Al₂O₃, (g) Ni(4.5)WO₃/ γ -Al₂O₃, (h) Ni(7.8)WO₃/ γ -Al₂O₃, (i) Ni(11.1)WO₃/ γ -Al₂O₃. The not labeled reflections correspond to γ -Al₂O₃. The labeled reflections correspond to WO₃(*) and NiO(▽).

The Raman spectra of the oxide precursors (Figure 2.5) exhibited a main band at 976 cm⁻¹ with a shoulder at around 898 cm⁻¹, which are attributed to the A₁ vibration of W=O, and the F₂ vibration of W-O, respectively.¹⁻⁴ This indicates the presence of W oxide species in distorted tetrahedral environment⁵. The two stretching modes of W-O that appeared at 695 cm⁻¹ and 800 cm⁻¹ are assigned to modes of WO₃ particles⁶ in line with the findings in XRD. Increasing Ni loading did not have a clear effect on the intensity of these signals. In the presence of Ni, however, the development of the broad band centered at ~280 cm⁻¹, associated to W-O-W linkages, suggests that Ni increases the connectivity of tetrahedral W oxide species. The band at 510 cm⁻¹, found only for Ni(11.1)WO₃/ γ -Al₂O₃, is consistent with the Ni-O vibration in crystalline NiO species.⁷

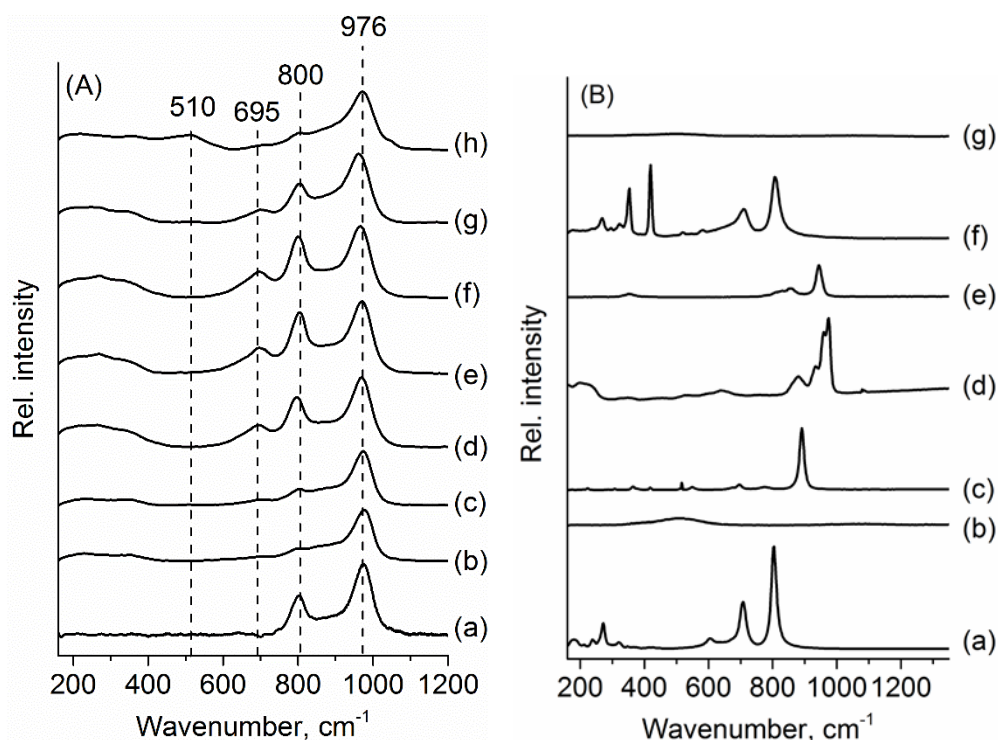


Figure 2.5. Raman spectra ($\lambda_{\text{ex}} = 514 \text{ nm}$) of (a) $\text{WO}_3/\gamma\text{-Al}_2\text{O}_3$, (b) $\text{Ni}(0.3)\text{WO}_3/\gamma\text{-Al}_2\text{O}_3$, (c) $\text{Ni}(1.1)\text{WO}_3/\gamma\text{-Al}_2\text{O}_3$, (d) $\text{Ni}(2.2)\text{WO}_3/\gamma\text{-Al}_2\text{O}_3$, (e) $\text{Ni}(3.2)\text{WO}_3/\gamma\text{-Al}_2\text{O}_3$, (f) $\text{Ni}(4.5)\text{WO}_3/\gamma\text{-Al}_2\text{O}_3$, (g) $\text{Ni}(7.8)\text{WO}_3/\gamma\text{-Al}_2\text{O}_3$, (h) $\text{Ni}(11.1)\text{WO}_3/\gamma\text{-Al}_2\text{O}_3$ in (A). Raman spectra ($\lambda_{\text{ex}} = 514 \text{ nm}$) of reference materials (a) WO_3 , (b) NiO , (c) NiWO_4 , (d) $(\text{NH}_4)_6\text{H}_2\text{W}_{12}\text{O}_{40}\cdot x\text{H}_2\text{O}$, (e) NiMoO_4 , (f) WS_2 , (g) Ni_3S_2 are shown in (B).

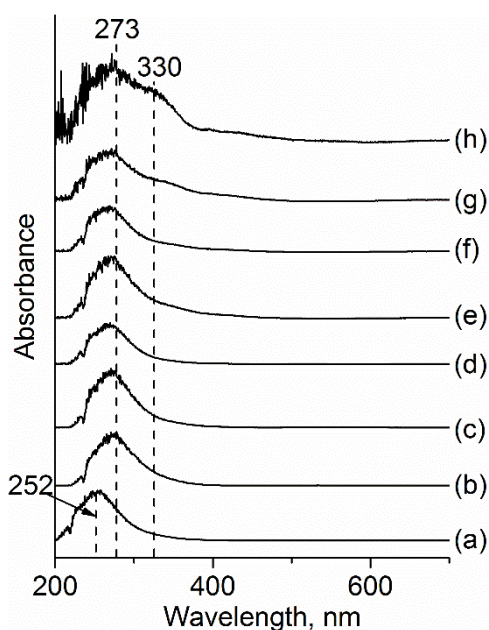


Figure 2.6. UV-Vis spectroscopy for (a) $\text{WO}_3/\gamma\text{-Al}_2\text{O}_3$, (b) $\text{Ni}(0.3)\text{WO}_3/\gamma\text{-Al}_2\text{O}_3$, (c) $\text{Ni}(1.1)\text{WO}_3/\gamma\text{-Al}_2\text{O}_3$, (d) $\text{Ni}(2.2)\text{WO}_3/\gamma\text{-Al}_2\text{O}_3$, (e) $\text{Ni}(3.2)\text{WO}_3/\gamma\text{-Al}_2\text{O}_3$, (f) $\text{Ni}(4.5)\text{WO}_3/\gamma\text{-Al}_2\text{O}_3$, (g) $\text{Ni}(7.8)\text{WO}_3/\gamma\text{-Al}_2\text{O}_3$, (h) $\text{Ni}(11.1)\text{WO}_3/\gamma\text{-Al}_2\text{O}_3$.

UV-Vis DR analysis (Figure 2.6) showed formation of polytungstate species (bands from 252 nm to 273 nm and 330 nm, O_h coordination⁸). Upon impregnation of Ni, the shift of the absorption edge to higher wavelengths indicated an increase in nuclearity of tungsten entities in the oligomeric oxides.^{9,10}

The small structural changes shown by Raman and UV-vis DR spectroscopy contrast the drastic changes observed at the surface by NO-IR as described in the following. The concentration of NO adsorbed on bare $\gamma\text{-Al}_2\text{O}_3$ was negligible, whereas NO adsorbed on $\text{WO}_3/\gamma\text{-Al}_2\text{O}_3$ gave rise to weak bands at wavenumbers below 1850 cm^{-1} (Figure 2.7A (a)). This is due to the steric hindrance of a d^0 -structure in an octahedral coordination around W atoms, therefore NO can barely adsorb.^{11,12} On $\text{NiO}/\gamma\text{-Al}_2\text{O}_3$, two bands appeared at 1852 cm^{-1} and 1776 cm^{-1} (Figure 2.7A(b)), which are assigned to NO on Ni^{2+} incorporated in octahedral sites of $\gamma\text{-Al}_2\text{O}_3$,¹³ and to NO adsorbed on exposed Ni^{2+} cations on NiO.^{14,15} NO adsorbed on the Ni-W oxide precursors produced a distinctive intense band at 1875 cm^{-1} , e.g., NO adsorbed on $\text{Ni}(3.2)\text{WO}_3/\gamma\text{-Al}_2\text{O}_3$ (Figure 2.7A (c)), which we attribute to Ni-substituted W-oxide octahedral species (labeled in the following as Ni-O-W) in agreement with Ref.¹⁵. Thus, the adsorption of NO allows for an accurate differentiation of adsorption sites on the precursors. At increasing Ni loadings, the contribution of the bands of NO adsorbed on NiO (1852 cm^{-1} and 1790 cm^{-1}) to the spectra of the bimetallic precursors increased, whereas the relative intensity of the band at 1875 cm^{-1} decreased (Figure 2.7B). The contribution of the band at 1875 cm^{-1} (NO on Ni-O-W) sharply increased with Ni/(W+Ni) molar ratio up to 0.25 and remained constant at higher ratios (Figure 2.7B). In contrast, the contributions of the bands at 1853 cm^{-1} and 1776 cm^{-1} (NO on NiO) increased sharply from 0.25 to 0.4 and slowly at higher Ni/(W+Ni) molar ratios (Figure 2.7B). These observations suggest that the formation of Ni-O-W species is preferred below the Ni/(W+Ni) molar ratio of 0.3. However, there seems to be a maximum for the amount of Ni that can be incorporated to the Ni-O-W species (reached when the area of the 1875 cm^{-1} band levels off). When the maximum is reached (above the Ni/(W+Ni) molar ratio of 0.3), there is a sudden increase in the proportion of NiO species (bands at 1853 cm^{-1} and 1776 cm^{-1}) with further Ni loading and a slow increase afterwards probably due to agglomeration as observed with XRD.

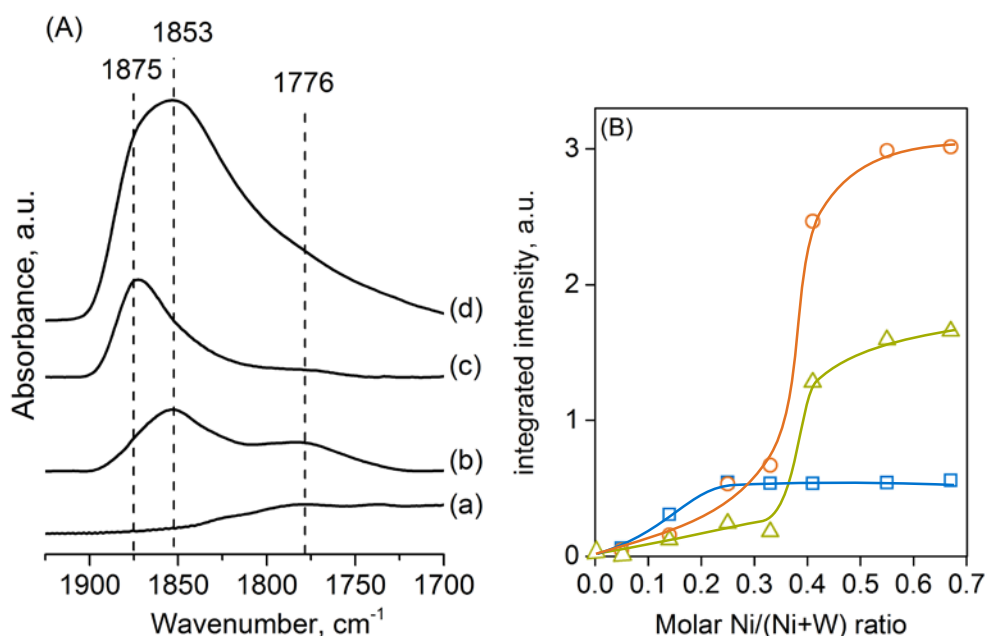


Figure 2.7. Infrared spectra of NO (A) adsorbed on $\text{WO}_3/\gamma\text{-Al}_2\text{O}_3$ (a), $\text{NiO}/\gamma\text{-Al}_2\text{O}_3$ (b), $\text{Ni}(2.2)\text{WO}_3/\gamma\text{-Al}_2\text{O}_3$ (c), and $\text{Ni}(11.1)\text{WO}_3/\gamma\text{-Al}_2\text{O}_3$ (d). Deconvoluted areas (B) of the bands at 1875 cm^{-1} (\square), 1852 cm^{-1} (\circ), and 1776 cm^{-1} (Δ) along the molar Ni/(W+Ni) ratio.

2.6.2 Impact of the W-Ni Interactions on the Sulfidation of Oxide Precursors

Sulfidation of $\gamma\text{-Al}_2\text{O}_3$ -supported W oxide species is a stepwise process^{19,20, 22,23, 33–37} as discussed for the TPS profiles for all the samples depicted in Figure 2.8. The first H_2S evolution signal below 400 K corresponds to physisorbed H_2S . In the subsequent step (above 400 K), terminal oxygen ligands on W(VI) are exchanged by sulfur yielding tungsten oxysulfides with bridged $\text{W}(=\text{S})_2$ species while releasing H_2O .^{4,16} The reduction of W(VI) to W(IV) with H_2 occurs in a $2e^-$ -redox process, which releases H_2S .²⁴ The corresponding H_2S evolution signal appears at a specific temperature (T_{red}) around 500–700 K although it might overlap with H_2S consumption due to O-S exchange of W and Ni species.¹⁸ After the reduction step, H_2S is further consumed in a high temperature O-S exchange step.

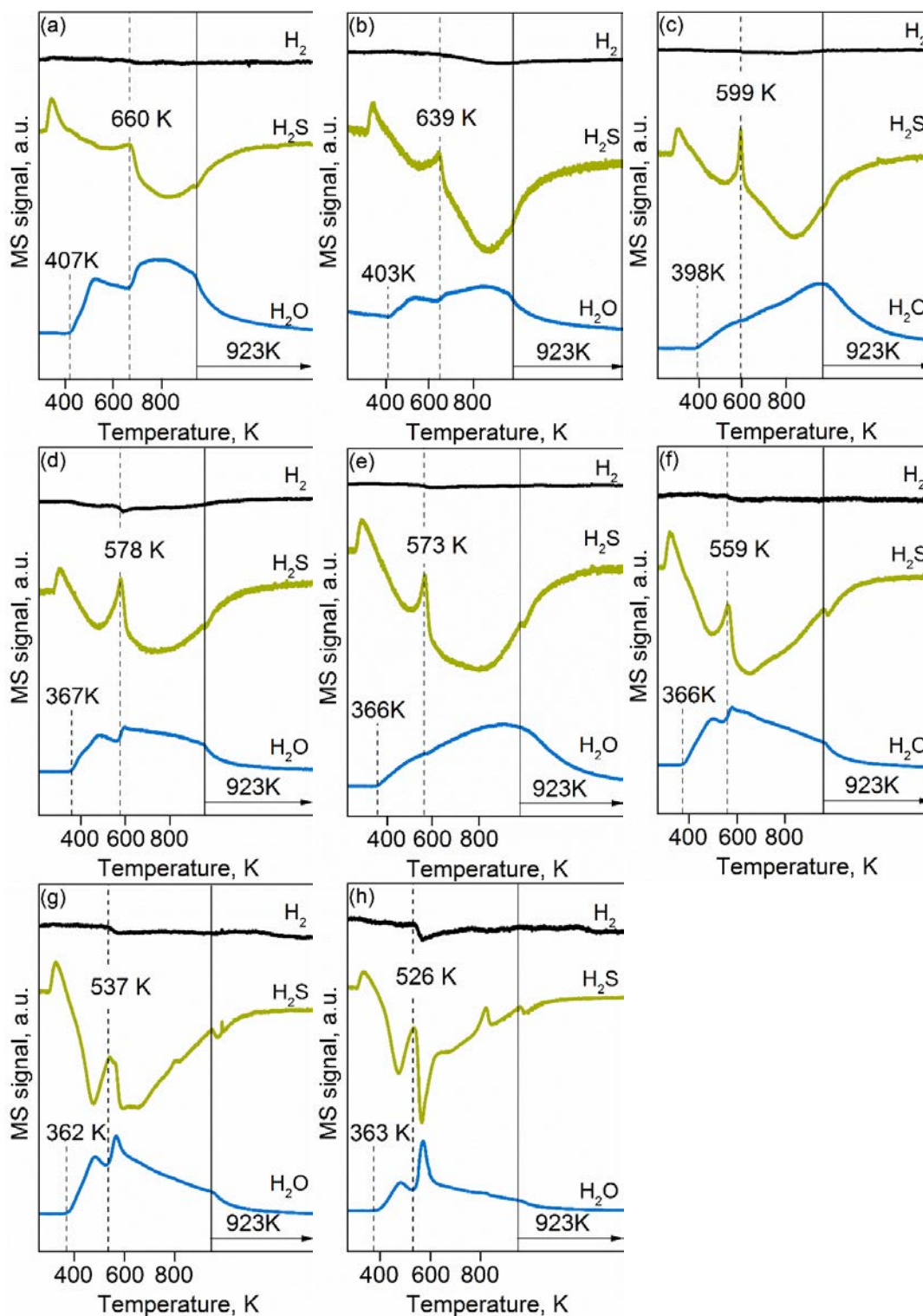


Figure 2.8. Profile of H_2O (blue), H_2S (green) and H_2 (black) signal during temperature programmed sulfidation for (a) $\text{WO}_3/\gamma\text{-Al}_2\text{O}_3$, (b) $\text{Ni}(0.5)\text{WO}_3/\gamma\text{-Al}_2\text{O}_3$, (c) $\text{Ni}(1.1)\text{WO}_3/\gamma\text{-Al}_2\text{O}_3$, (d) $\text{Ni}(2.2)\text{WO}_3/\gamma\text{-Al}_2\text{O}_3$, (e) $\text{Ni}(3.2)\text{WO}_3/\gamma\text{-Al}_2\text{O}_3$, (f) $\text{Ni}(4.5)\text{WO}_3/\gamma\text{-Al}_2\text{O}_3$, (g) $\text{Ni}(7.8)\text{WO}_3/\gamma\text{-Al}_2\text{O}_3$, (h) $\text{Ni}(11.1)\text{WO}_3/\gamma\text{-Al}_2\text{O}_3$.

In the TPS profiles of all catalysts, the onset of H_2O evolution, from S-O exchange (T_{ex}), shifted to lower temperature as the Ni content increased (Figure 2.9(b)), i.e., from 407

K for $\text{WO}_3/\gamma\text{-Al}_2\text{O}_3$ to 367 K on $\text{Ni}(3.2)\text{WO}_3/\gamma\text{-Al}_2\text{O}_3$. T_{ex} leveled off with further Ni loading. This observation suggests that the formation of Ni-O-W species weakens the W=O bonds easing the O-S exchange on W(VI). The effect of Ni loading on T_{ex} was much weaker at Ni/(W+Ni) molar ratios above 0.25, which indicates that the Ni incorporation on W oxide species is mostly completed at that Ni ratio in agreement with the trend of the NO-IR band at 1875 cm^{-1} (Figure 2.7). The duration of reduction step also shifted to lower temperature with increasing Ni content. That is, from 213 K for $\text{WO}_3/\gamma\text{-Al}_2\text{O}_3$, over 132 K for $\text{Ni}(3.2)\text{WO}_3/\gamma\text{-Al}_2\text{O}_3$, to 79 K for $\text{Ni}(11.1)\text{WO}_3/\gamma\text{-Al}_2\text{O}_3$, as depicted in Figure 2.8. T_{red} decreased continuously from 660 K ($\text{WO}_3/\gamma\text{-Al}_2\text{O}_3$) to 526 K ($\text{Ni}(11.1)\text{WO}_3/\gamma\text{-Al}_2\text{O}_3$) inversely correlating the Ni/(W+Ni) molar ratio (Figure 2.9(a)).

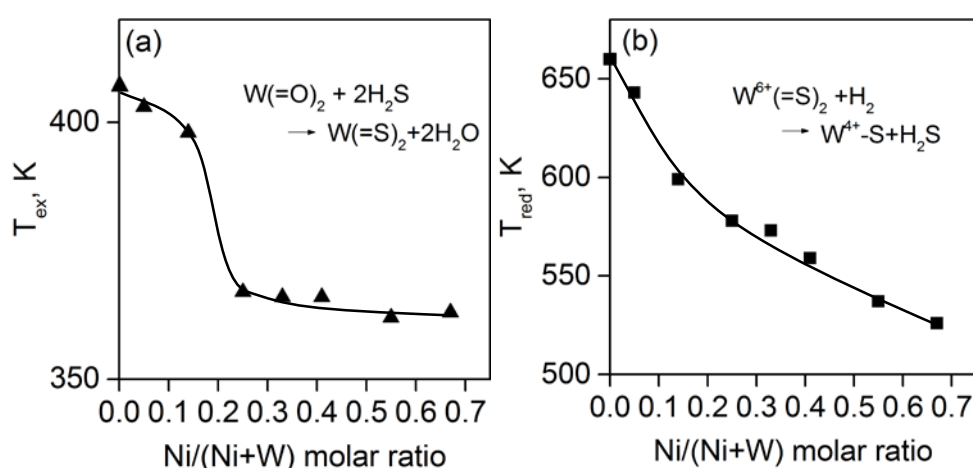


Figure 2.9. Sulfur-exchange temperature, T_{ex} (a), and reduction temperature, T_{red} (b), observed during temperature programmed sulfidation, as a function of molar Ni/(W+Ni) ratio.

2.6.3 Kinetic Data for Hydrogenation of Phenanthrene

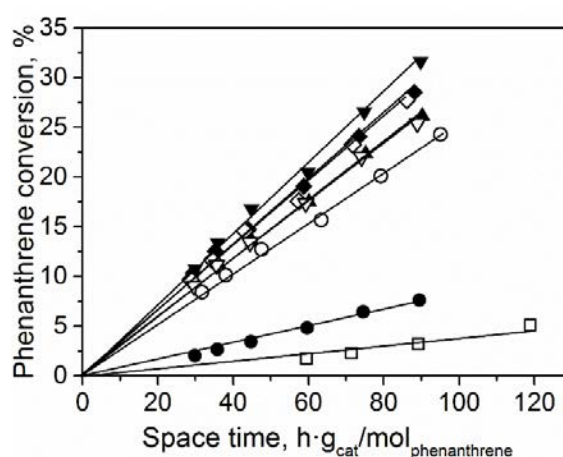


Figure 2.10. Conversion of phenanthrene as function of space time over $\text{WS}_2/\gamma\text{-Al}_2\text{O}_3$ (□), $\text{Ni}(0.3)\text{WS}_2/\gamma\text{-Al}_2\text{O}_3$ (●), $\text{Ni}(1.5)\text{WS}_2/\gamma\text{-Al}_2\text{O}_3$ (▲), $\text{Ni}(2.2)\text{WS}_2/\gamma\text{-Al}_2\text{O}_3$ (▼), $\text{Ni}(3.2)\text{WS}_2/\gamma\text{-Al}_2\text{O}_3$ (◆), $\text{Ni}(4.5)\text{WS}_2/\gamma\text{-Al}_2\text{O}_3$ (◇), $\text{Ni}(7.8)\text{WS}_2/\gamma\text{-Al}_2\text{O}_3$ (▽), $\text{Ni}(11.1)\text{WS}_2/\gamma\text{-Al}_2\text{O}_3$ (○).

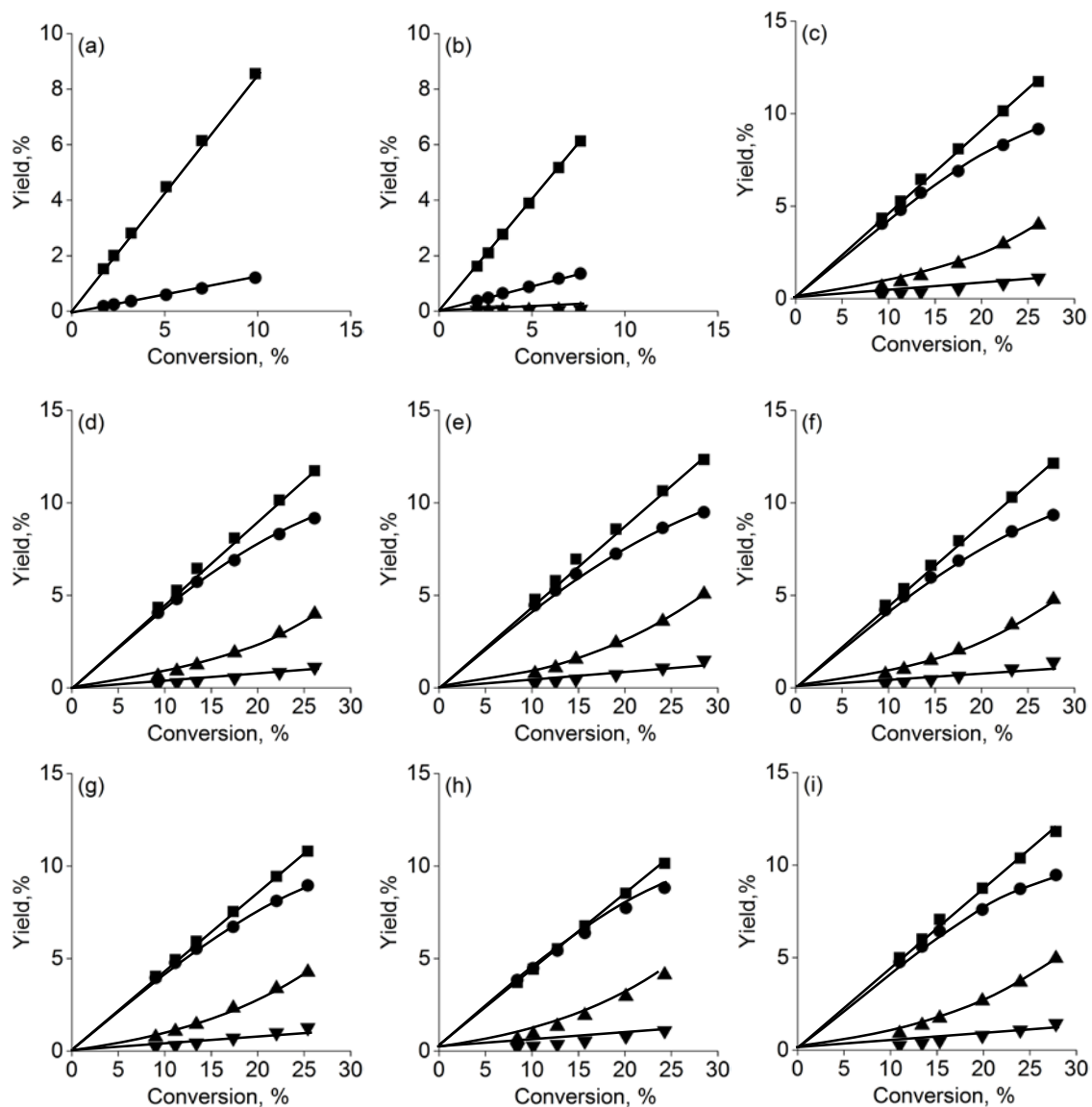


Figure 2.11. Product yields as a function of phenanthrene conversion on: (a) $WS_2/\gamma-Al_2O_3$, (b) $Ni(0.3)WS_2/\gamma-Al_2O_3$, (c) $Ni(1.5)WS_2/\gamma-Al_2O_3$, (d) $Ni(2.2)WS_2/\gamma-Al_2O_3$, (e) $Ni(3.2)WS_2/\gamma-Al_2O_3$, (f) $Ni(4.5)WS_2/\gamma-Al_2O_3$, (g) $Ni(7.8)WS_2/\gamma-Al_2O_3$, (h) $Ni(11.1)WS_2/\gamma-Al_2O_3$, (i) $Ni(2.5)MoWS_2/\gamma-Al_2O_3$. The products are labeled as DiHPhe(■), TetHPhe(●), *sym*OHPhe(▲), *asym*OHPhe(▼). On $WS_2/\gamma-Al_2O_3$, *sym*OHPhe and *asym*OHPhe were observed only in trace amounts. Continuous lines represent trends.

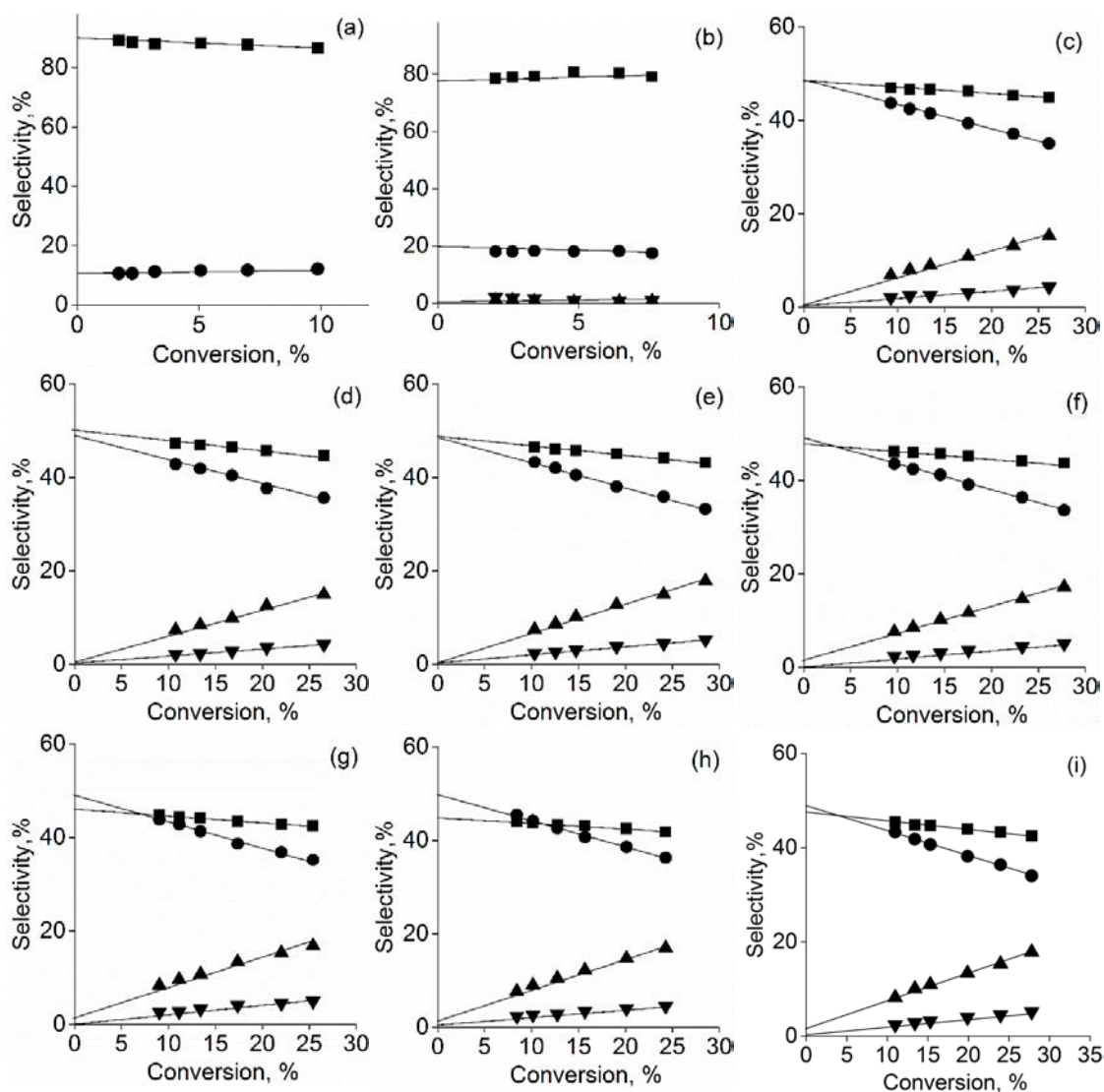


Figure 2.12. Selectivity-conversion plots of hydrogenation of phenanthrene on (a) $\text{WS}_2/\gamma\text{-Al}_2\text{O}_3$, (b) $\text{Ni}(0.3)\text{WS}_2/\gamma\text{-Al}_2\text{O}_3$, (c) $\text{Ni}(1.5)\text{WS}_2/\gamma\text{-Al}_2\text{O}_3$, (d) $\text{Ni}(2.2)\text{WS}_2/\gamma\text{-Al}_2\text{O}_3$, (e) $\text{Ni}(3.2)\text{WS}_2/\gamma\text{-Al}_2\text{O}_3$, (f) $\text{Ni}(4.5)\text{WS}_2/\gamma\text{-Al}_2\text{O}_3$, (g) $\text{Ni}(7.8)\text{WS}_2/\gamma\text{-Al}_2\text{O}_3$, (h) $\text{Ni}(11.1)\text{WS}_2/\gamma\text{-Al}_2\text{O}_3$, (i) $\text{Ni}(2.5)\text{MoWS}_2/\gamma\text{-Al}_2\text{O}_3$. The hydrogenation products are marked as DiHPhe(■), TetHPhe(●), *sym*OHPhe(▲), *asym*OHPhe(▼).

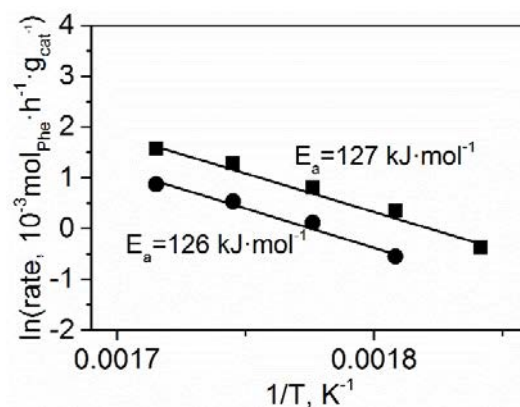


Figure 2.13. Arrhenius plots of hydrogenation of phenanthrene over Ni(2.2)WS₂/γ-Al₂O₃ catalysts(■) and over Ni(2.7)MoS₂/γ-Al₂O₃ (●). Hydrogenation rates were determined at temperatures from 543 to 583 K at a H₂ to hydrocarbon volumetric ratio of 300.

2.6.4 Structural Characterization of WS₂-based Catalysts

2.6.4.1 XRD, TEM and Raman

All sulfide catalysts exhibited reflections at 2θ of 33 and 59° (Figure 2.14), which correspond to WS₂ (JCPDS file No.8-237). Weak reflections of Ni₃S₂ (JCPDS file No.44-1418) were observed in Ni(11.1)WS₂/γ-Al₂O₃ and Ni(7.8)WS₂/γ-Al₂O₃ at 2θ of 30, 51, and 55°. There was no appreciable effect of Ni on the diffraction patterns of WS₂ except for a loss of intensity at 33°.

In line with XRD measurements, the effect of Ni on the structure of WS₂ shown by HRTEM was also limited (representative micrographs shown in Figure 2.15). The average slab length of WS₂ decreased in the presence of Ni, i.e., from 5.6 nm in WS₂/γ-Al₂O₃ to 4.5 nm in Ni(1.5)WS₂/γ-Al₂O₃ (Table 2.4). Ni concentrations above 1 wt.% changed the average slab length only to a minor extent. The average stacking degree was ~2 for all catalysts (Table 2.4). The fraction of edge W-atoms in a WS₂ slabs (f_w), determined from the slab length assuming a perfect hexagonal geometry,²⁵ increased slightly with the addition of Ni, e.g., from 0.2 for WS₂/γ-Al₂O₃, to 0.24 for Ni(2.2)WS₂/γ-Al₂O₃, and was the highest at 0.27 for Ni(11.1)WS₂/γ-Al₂O₃.

Table 2.4 Measured molar fraction of Ni, average slab length, stacking degree (TEM), and dispersion factor $f_{W \text{ or } Mo}$ of the WS_2 or MoS_2 phase (standard deviation given in brackets).

Catalyst	Ni/(M+Ni) mol/mol	Slab length, [nm]	Stacking	$f_{W \text{ or } Mo}$
$WS_2/\gamma-Al_2O_3$	-	5.6 (2.1)	2.0 (1.1)	0.20
Ni(0.3) $WS_2/\gamma-Al_2O_3$	0.05	5.1 (1.8)	2.0 (1.0)	0.21
Ni(1.1) $WS_2/\gamma-Al_2O_3$	0.14	4.5 (1.9)	1.9 (0.9)	0.22
Ni(2.2) $WS_2/\gamma-Al_2O_3$	0.25	4.2 (1.6)	1.9 (0.9)	0.24
Ni(3.2) $WS_2/\gamma-Al_2O_3$	0.33	4.2 (1.8)	2.0 (1.0)	0.24
Ni(4.5) $WS_2/\gamma-Al_2O_3$	0.41	4.1 (1.8)	1.9 (1.0)	0.24
Ni(7.8) $WS_2/\gamma-Al_2O_3$	0.55	4.0 (1.6)	2.0 (1.1)	0.25
Ni(11.1) $WS_2/\gamma-Al_2O_3$	0.67	3.6 (1.5)	2.1 (1.1)	0.27
Ni(2.5) $MoS_2/\gamma-Al_2O_3$	0.34	3.9 (2.2)	1.7 (0.7)	0.25
$NiS_x/\gamma-Al_2O_3$	-	-	-	-
$MoS_2/\gamma-Al_2O_3$ ^[a]	-	5.5 (2.2)	1.5 (0.7)	0.22
Ni(1.3) $MoS_2/\gamma-Al_2O_3$ ^[a]		4.7 (1.9)	1.6 (0.8)	0.26
Ni(2.7) $MoS_2/\gamma-Al_2O_3$ ^[a]		4.5 (1.9)	1.9 (0.9)	0.26
Ni(5.0) $MoS_2/\gamma-Al_2O_3$ ^[a]		4.5 (1.9)	1.7 (0.9)	0.26
Ni(8.8) $MoS_2/\gamma-Al_2O_3$ ^[a]		4.6 (1.9)	1.8 (1.1)	0.26

[a] Data for MoS_2 and the corresponding Ni promoted series are taken from ref.[²⁶].

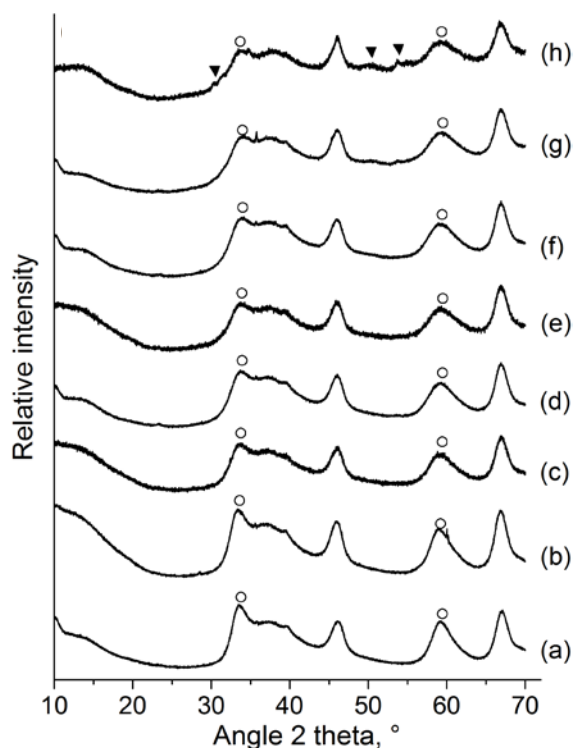


Figure 2.14. X-ray diffractograms of sulfide catalysts: (a) $WS_2/\gamma-Al_2O_3$, (b) Ni(0.3) $WS_2/\gamma-Al_2O_3$, (c) Ni(1.1) $WS_2/\gamma-Al_2O_3$, (d) Ni(2.2) $WS_2/\gamma-Al_2O_3$, (e) Ni(3.2) $WS_2/\gamma-Al_2O_3$, (f) Ni(4.5) $WS_2/\gamma-Al_2O_3$, (g) Ni(7.8) $WS_2/\gamma-Al_2O_3$, (h) Ni(11.1) $WS_2/\gamma-Al_2O_3$. Labeled reflections correspond to WS_2 (\circ) and Ni_3S_2 (\blacktriangledown), while non-labeled reflections correspond to Al_2O_3 .

The signals between 10 and 20 degree 2 theta are due to accidental instrumental baseline drifts at the time of these measurements.

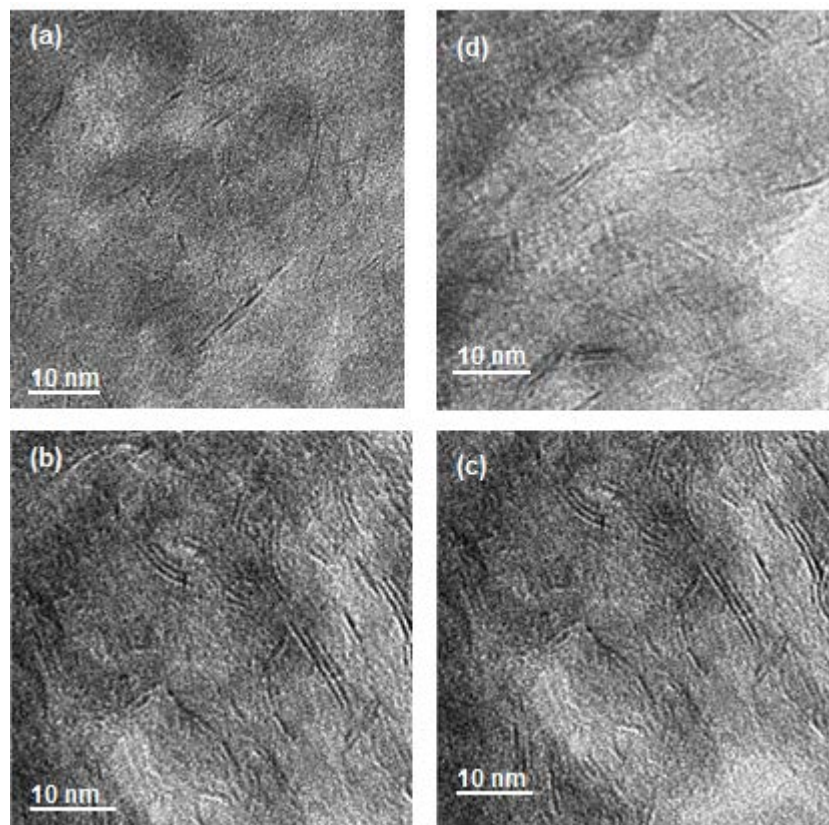


Figure 2.15. Representative transmission electron micrographs of (a) $WS_2/\gamma-Al_2O_3$, (b) $Ni(2.2)WS_2/\gamma-Al_2O_3$ (c) $Ni(7.8)WS_2/\gamma-Al_2O_3$, (d) $Ni(11.1)WS_2/\gamma-Al_2O_3$.

The Raman spectra of the sulfide catalysts showed A_{1g} and E_{2g}^1 modes^{27,28} at 421 and 345 cm^{-1} , respectively, as shown for $WS_2/\gamma-Al_2O_3$ and $Ni(2.2)WS_2/\gamma-Al_2O_3$ in Figure 2.16(a) and (c). The band of the A_{1g} mode shifted to higher wavenumbers compared to the reference bulk WS_2 (at 415 cm^{-1}), which is attributed to a low stacking degree and weak van der Waals forces between layers in the supported catalysts.²⁷ The addition of Ni did not influence the position of the discussed bands. Bands of oxide species were not detected in the as-sulfided catalysts, suggesting that the material was fully sulfided. In separate experiments, the Raman spectra of $WS_2/\gamma-Al_2O_3$ and $Ni(2.2)WS_2/\gamma-Al_2O_3$ were recorded after exposing the samples to NO (Figure 2.16(b) and (d)). No new peaks were observed on NO-exposed $WS_2/\gamma-Al_2O_3$. Two additional bands, however, appeared for $Ni(2.2)WS_2/\gamma-Al_2O_3$ at 795 and 967 cm^{-1} , which correspond to stretching modes of W-O and W=O in tetrahedrally coordinated W,¹⁻⁴ respectively. Thus, Ni- WS_2 is concluded to be oxidized at room temperature by NO, whereas non-promoted WS_2 ($WS_2/\gamma-Al_2O_3$) is not.

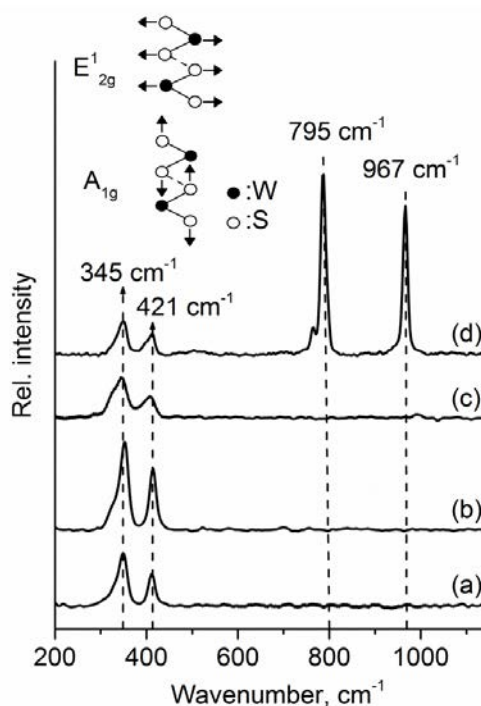


Figure 2.16. Raman spectra ($\lambda_{\text{ex}} = 514 \text{ nm}$) of as-sulfided $\text{WS}_2/\gamma\text{-Al}_2\text{O}_3$ (a), $\text{WS}_2/\gamma\text{-Al}_2\text{O}_3$ exposed to NO at room temperature (b), as-sulfided $\text{Ni}(2.2)\text{WS}_2/\gamma\text{-Al}_2\text{O}_3$ (c), and $\text{Ni}(2.2)\text{WS}_2/\gamma\text{-Al}_2\text{O}_3$ exposed to NO at room temperature (d). The E_{2g}^1 and A_{1g} modes of W-S atomic displacement are illustrated on the top left. The 795 cm^{-1} and 967 cm^{-1} peaks in (d) arise from stretching modes of W-O and W=O in tetrahedrally coordinated W, indicating oxidation of the sulfide phase by NO.

2.6.4.2 Adsorption of NO

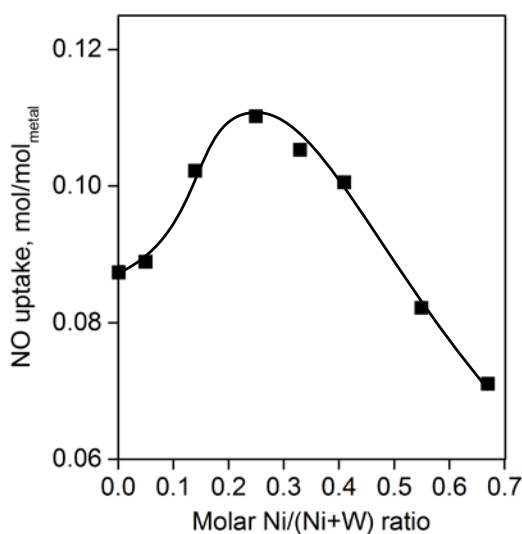


Figure 2.17. NO uptake normalized to the atomic content of metal of the catalysts as a function of atomic $\text{Ni}/(\text{W}+\text{Ni})$ ratio. The continuous line represents a trend.

For the studied samples the mass-normalized NO uptake increased steadily with the Ni concentration. The concentration of NO adsorbed per mole of metal reached the maximum at a Ni/(Ni+W) atomic ratio of 0.25 (Figure 2.17), as was also observed for Ni-MoS₂/ γ -Al₂O₃.²⁶ The decreasing NO uptake per mole of metal at Ni/(Ni+M) ratio > 0.25 is attributed to the reduced accessibility of the slab edges caused by extra-lattice NiS_x crystallites that form at the Ni-substituted edge.

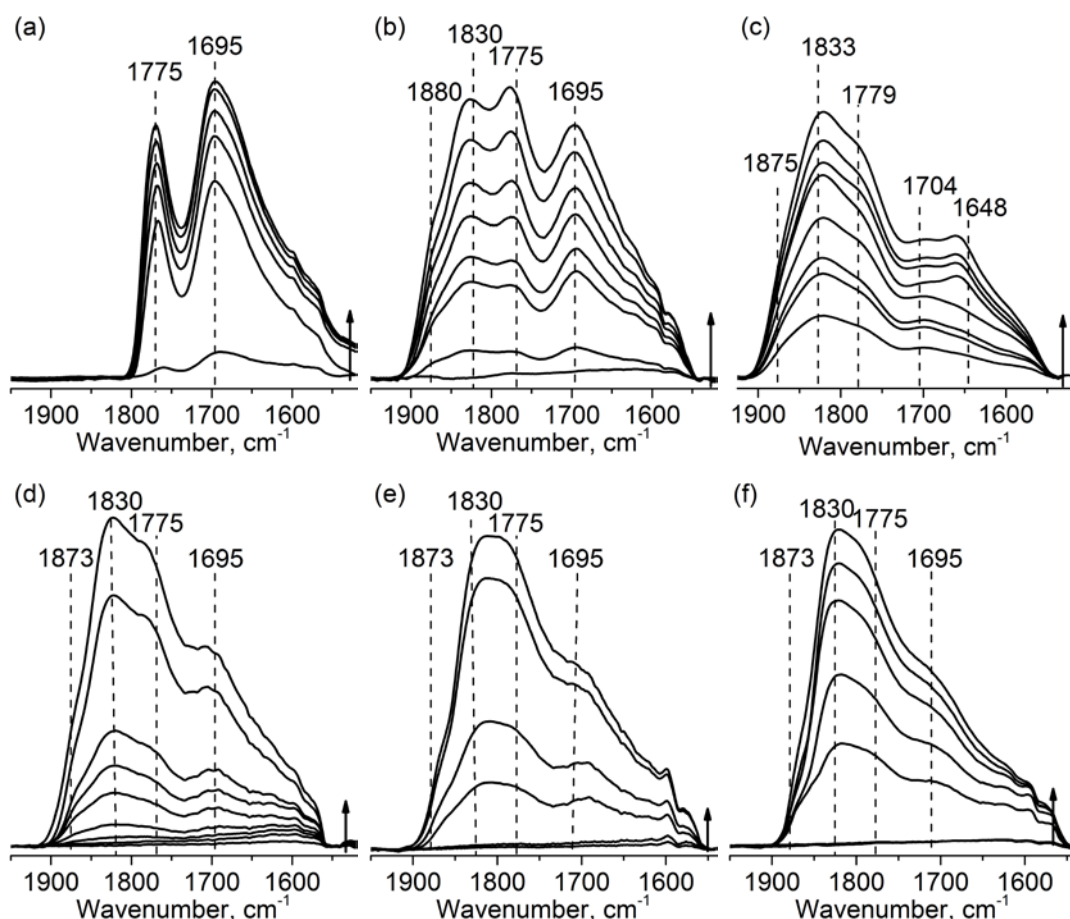


Figure 2.18. IR spectra of NO adsorbed at 303 K on (a) WS₂/ γ -Al₂O₃, (b) Ni(2.2)WS₂/ γ -Al₂O₃, (c) Ni(3.2)WS₂/ γ -Al₂O₃, (d) Ni(4.5)WS₂/ γ -Al₂O₃, (e) Ni(7.8)WS₂/ γ -Al₂O₃ and (f) Ni(11.1)WS₂/ γ -Al₂O₃. The bottom traces in these spectra correspond to the lowest NO dosage in each case.

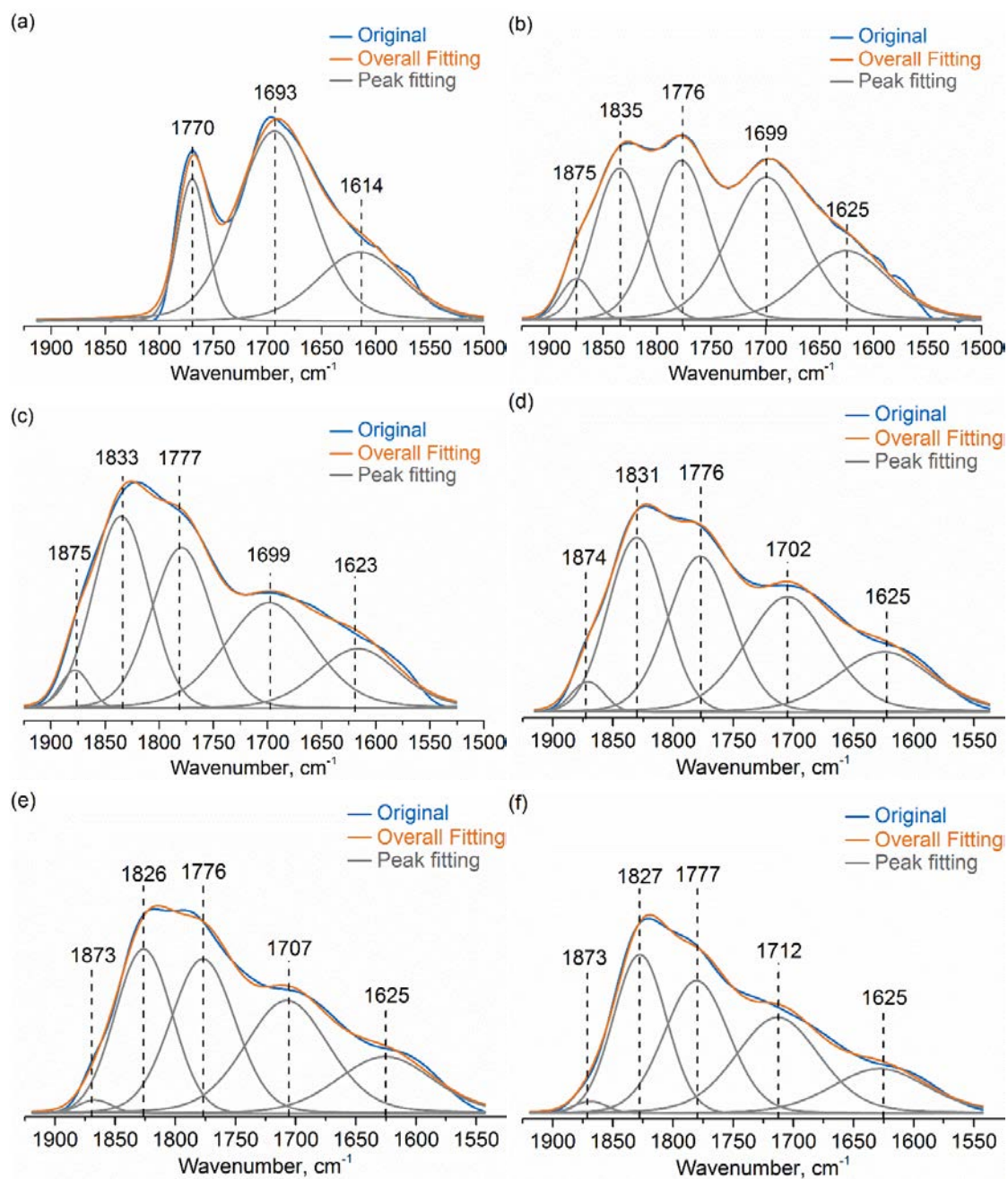


Figure 2.19. Deconvoluted IR spectra of NO adsorbed on (a) WS₂/γ-Al₂O₃, (b) Ni(2.2)WS₂/γ-Al₂O₃, (c) Ni(3.2)WS₂/γ-Al₂O₃, (d) Ni(4.5)WS₂/γ-Al₂O₃, (e) Ni(7.8)WS₂/γ-Al₂O₃, and (f) Ni(11.1)WS₂/γ-Al₂O₃.

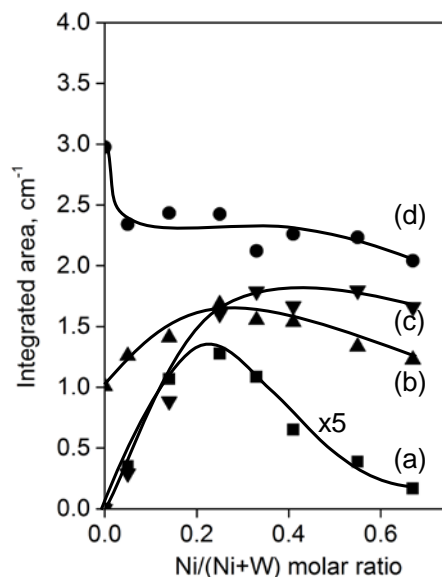


Figure 2.20. Integrated areas of the deconvoluted bands of NO adsorbed on Ni(x)WS₂/γ-Al₂O₃ sulfides as a function of the molar ratio of Ni/(Ni+W) at 1875 (a), 1770 (b), 1830 (c) and 1695 cm⁻¹ (d). The continuous line represents a trend.

2.6.5 Determination of Surface Brønsted and Lewis Acid Sites

2.6.5.1 DMP Adsorption Probed by IR Spectroscopy

In order to quantify the Brønsted acid site (BAS) concentration, i.e., the concentration of SH groups of Ni-WS₂/γ-Al₂O₃ catalysts, co-adsorption of DMP and H₂S(or H₂) was followed by IR spectroscopy; the methodology was reported in ref^{29,30}. Deconvoluted spectra are shown in Figure 2.21 and 2.22. Protonated DMP gives rise to vibration bands ν_{8a} (~1650 cm⁻¹) and ν_{8b} (~1627 cm⁻¹), the peaks at ~1615 and 1580 cm⁻¹ result from DMP coordinated to Lewis acid sites (LAS), and the bands at 1602 and 1580 cm⁻¹ correspond to weakly adsorbed DMP.^{31,32}

The concentration of SH groups quantified by IR spectroscopy is listed in Table 2.5, which is equated to the SH concentration for each material, based on a 1:1 stoichiometry between the base molecule and the BAS (-SH group). To build a correlation between the SH concentration and the reaction rate of phenanthrene hydrogenation only associated with Ni decorated at the edge, the contributions of SH associated with W or Mo at the slab edge, as well as their contribution to the reaction rate, have been subtracted (Table 2.5 and ref²⁹). The resultant values are denoted as the corrected SH concentration and the corrected rate, respectively.

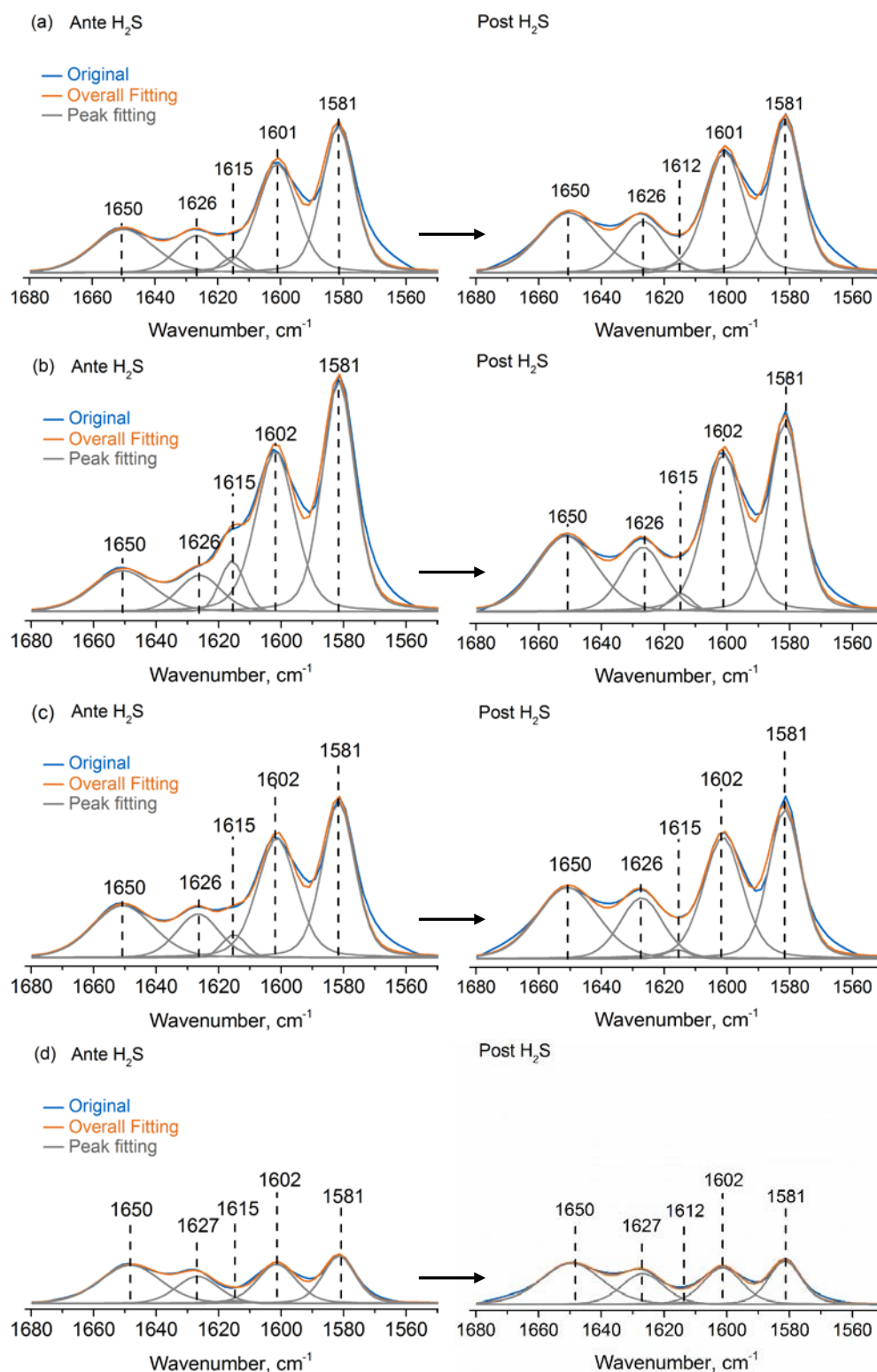


Figure 2.21. Deconvoluted infrared spectra of adsorbed 2,6-dimethylpyridine before and after the addition of H₂S (1 mbar) on (a) WS₂/γ-Al₂O₃, (b) Ni(2.2)WS₂/γ-Al₂O₃, (c) Ni(3.2)WS₂/γ-Al₂O₃, (d) Ni(11.1)WS₂/γ-Al₂O₃.

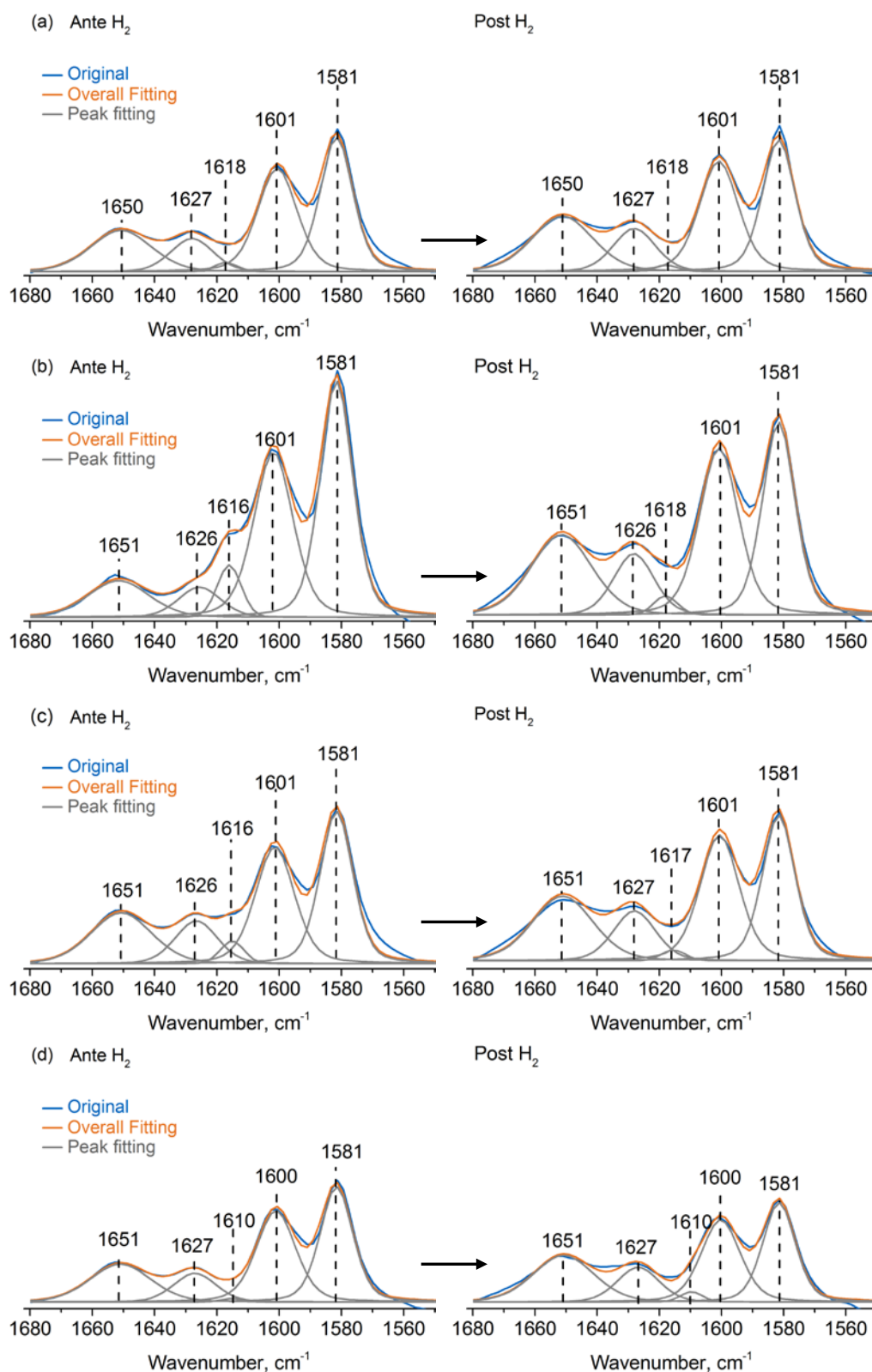


Figure 2.22. Deconvoluted IR spectra of adsorbed 2,6-dimethylpyridine before and after the addition of H₂ (1 bar) on (a) WS₂/γ-Al₂O₃, (b) Ni(2.2)WS₂/γ-Al₂O₃, (c) Ni(3.2)WS₂/γ-Al₂O₃, (d) Ni(11.1)WS₂/γ-Al₂O₃, collected after exposure to 1 bar of H₂.

Table 2.5. Concentration of protonated 2,6-dimethylpyridine before and after co-adsorption of H₂S (1 mbar) or H₂ (1 bar) for chosen sulfide catalysts. Note that the experiments employing H₂S or H₂ are separate runs, leading to slight differences in the SH concentration on the as-sulfided samples. The data for MoS₂-based catalysts are taken from a paper published earlier by this group using the same experimental protocol.²⁹

Catalyst	SH concentration (C _{SH} , μmol g ⁻¹)				Corrected SH conc. after H ₂	Corrected Rate (10 ⁻³ mol h ⁻¹ g _{cat} ⁻¹)
	As sul-fided	After H ₂ S	As sul-fided	After H ₂		
WS ₂ /γ-Al ₂ O ₃	69	113	62	82	82	0.46
Ni(2.2)WS ₂ /γ-Al ₂ O ₃	73	170	74	162	109	3.25
Ni(3.2)WS ₂ /γ-Al ₂ O ₃	100	156	101	150	104	3.05
Ni(4.5) WS ₂ /γ-Al ₂ O ₃	-	-	96	136	92	2.97
Ni(11.1)WS ₂ /γ-Al ₂ O ₃	82	93	84	91	58	2.30
WS ₂ /γ-Al ₂ O ₃ -a	-	-	47	55	55	0.24
WS ₂ /γ-Al ₂ O ₃ -b	-	-	60	71	71	0.35
Ni(2.5)MoWS ₂ /γ-Al ₂ O ₃	-	-	80	132	85	2.81
MoS ₂ /γ-Al ₂ O ₃	79	98	79	88	88	0.58
Ni(1.3)MoS ₂ /γ-Al ₂ O ₃	93	114	82	96	30	0.70
Ni(2.7)MoS ₂ /γ-Al ₂ O ₃	95	119	91	107	46	1.17
Ni(5.0)MoS ₂ /γ-Al ₂ O ₃	87	109	71	79	25	0.90
Ni(8.8)MoS ₂ /γ-Al ₂ O ₃	86	106	75	83	35	0.77
γ-Al ₂ O ₃	20	21	17	17	-	-

2.6.5.2 Lewis Acid sites Probed by Pyridine Adsorption

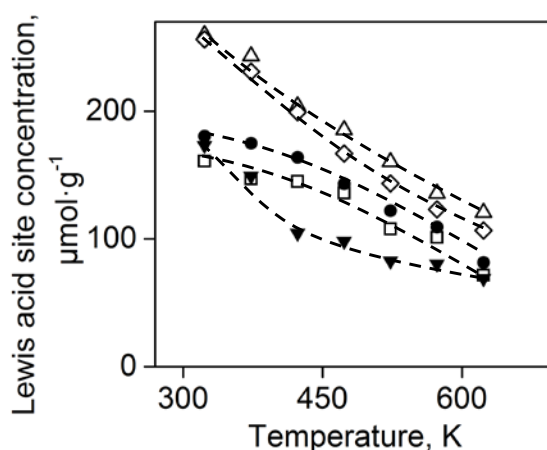


Figure 2.23. Concentration of pyridine (measured under 10⁻⁷ mbar) adsorbed on Lewis acid sites of WS₂/γ-Al₂O₃(□), Ni(2.2)WS₂/γ-Al₂O₃(Δ), Ni(3.2)WS₂/γ-Al₂O₃(◇), MoS₂/γ-Al₂O₃(▼), and Ni(2.7)MoS₂/γ-Al₂O₃(●) as a function of desorption temperature.

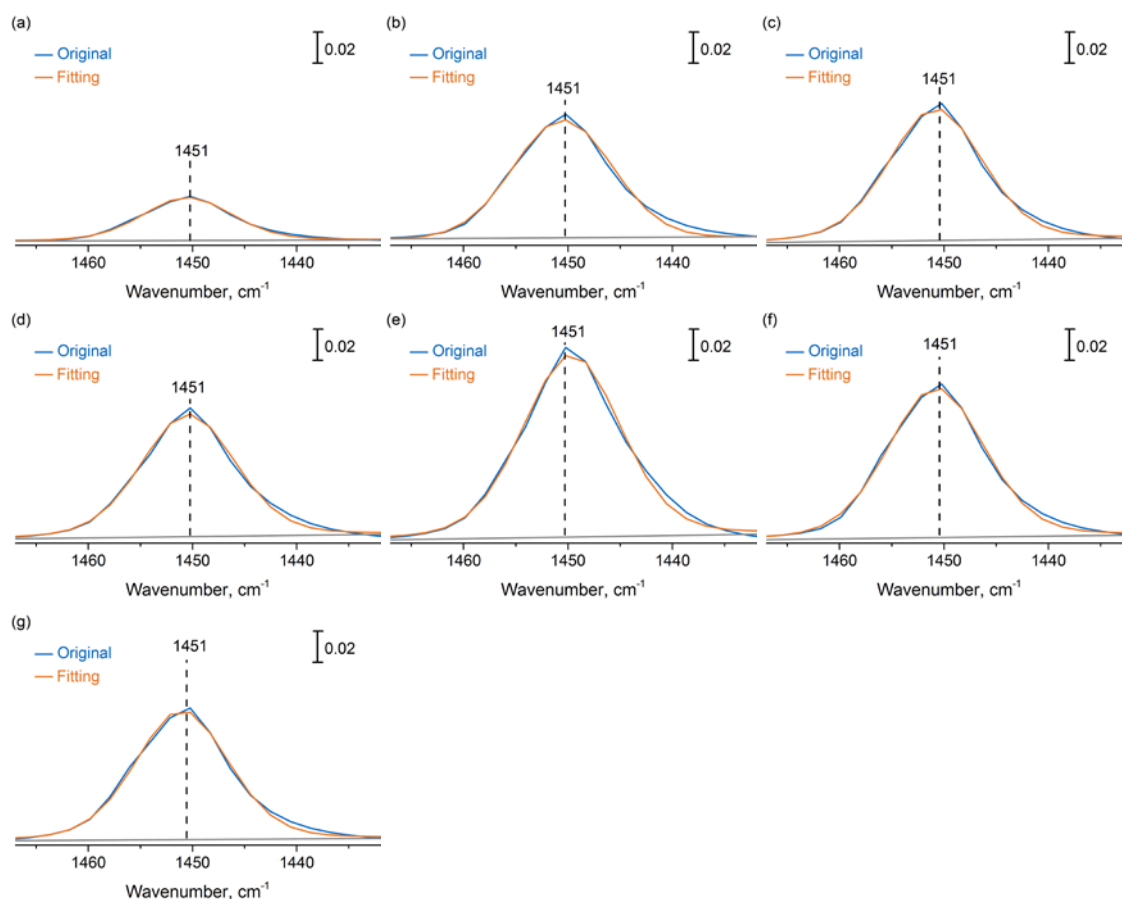


Figure 2.24. Deconvoluted IR spectra of adsorbed pyridine at Lewis acid sites on (a) γ - Al_2O_3 , (b) $\text{MoS}_2/\gamma\text{-Al}_2\text{O}_3$, (c) $\text{Ni}(2.7)\text{MoS}_2/\gamma\text{-Al}_2\text{O}_3$, (d) $\text{WS}_2/\gamma\text{-Al}_2\text{O}_3$, (e) $\text{Ni}(2.2)\text{WS}_2/\gamma\text{-Al}_2\text{O}_3$, (f) $\text{Ni}(3.2)\text{WS}_2/\gamma\text{-Al}_2\text{O}_3$, and (g) $\text{Ni}(11.1)\text{WS}_2/\gamma\text{-Al}_2\text{O}_3$. The measurements were conducted at an equilibrium pyridine pressure of 10^{-7} mbar and 623 K.

Table 2.6. Concentration of pyridine adsorbed at strong Lewis acid sites (adsorption band at 1451 cm^{-1}) for chosen sulfide catalysts, with measurements conducted at an equilibrium pyridine pressure of 10^{-7} mbar and 623 K.

Catalyst	Concentration of strong Lewis acid sites, $\mu\text{mol g}^{-1}$
$\text{WS}_2/\gamma\text{-Al}_2\text{O}_3$	71
$\text{Ni}(2.2)\text{WS}_2/\gamma\text{-Al}_2\text{O}_3$	120
$\text{Ni}(3.2)\text{WS}_2/\gamma\text{-Al}_2\text{O}_3$	106
$\text{Ni}(4.5)\text{WS}_2/\gamma\text{-Al}_2\text{O}_3$	97
$\text{WS}_2/\gamma\text{-Al}_2\text{O}_3\text{-a}$	34
$\text{WS}_2/\gamma\text{-Al}_2\text{O}_3\text{-b}$	57
$\text{Ni}(2.5)\text{MoWS}_2/\gamma\text{-Al}_2\text{O}_3$	95
$\text{MoS}_2/\gamma\text{-Al}_2\text{O}_3$	68
$\text{Ni}(2.7)\text{MoS}_2/\gamma\text{-Al}_2\text{O}_3$	81

2.6.6 Estimation of Molar Extinction Coefficients and the Fraction of Ni at Slab Edges

Table 2.7. Number of total metal atoms located on the edge of a hexagonal shaped slab, number of Ni and W atoms located at the edges of an average WS₂ particle, and the fraction of Ni among the edge atoms for catalysts studied in this work.

Catalyst	Atoms on the edge per particle	W atoms on the edge per particle	Ni atoms on the edge per particle	Ni/(Ni+M) on the edge, %
WS ₂ /γ-Al ₂ O ₃	99	99	0	0
Ni(0.3)WS ₂ /γ-Al ₂ O ₃	84	77	7	8
Ni(1.5)WS ₂ /γ-Al ₂ O ₃	75	54	21	28
Ni(2.2)WS ₂ /γ-Al ₂ O ₃	71	46	25	35
Ni(3.2)WS ₂ /γ-Al ₂ O ₃	72	40	21	29
Ni(4.5)WS ₂ /γ-Al ₂ O ₃	68	37	13	19
Ni(7.8)WS ₂ /γ-Al ₂ O ₃	70	35	4	6
Ni(11.1)WS ₂ /γ-Al ₂ O ₃	60	29	2	3

Table 2.8. Comparison of the degree of Ni decoration at the slab edge on WS₂/γ-Al₂O₃ and MoS₂/γ-Al₂O₃ (data taken from ref.²⁶)

Catalyst	Atoms on the edge per particle	Mo or W atoms on the edge per particle	Ni atoms on the edge per particle	Ni/(Ni+M) on the edge
WS ₂ /γ-Al ₂ O ₃	99	99	0	0
Ni(2.2)WS ₂ /γ-Al ₂ O ₃	71	46	25	35%
Ni(3.2)WS ₂ /γ-Al ₂ O ₃	72	40	21	29%
MoS ₂ /γ-Al ₂ O ₃	78	78	0	0
Ni(2.7)MoS ₂ /γ-Al ₂ O ₃	78	54	24	31%

Under the assumption of hexagonal geometry, the number of W atoms per particle as well as number of the edge atoms in the WS₂ slabs of WS₂/γ-Al₂O₃ were obtained using the corresponding geometric model²⁵ and the inter-atomic distance $d_{w-w}=3.2 \text{ \AA}$. Relating this concentration of W sites at the edge to the intensity of the corresponding IR signal (at 1695-1701 cm⁻¹), the apparent molar extinction coefficient of NO adsorbed on non-promoted WS₂ sites was estimated to be 3.9 cm μmol⁻¹. The second assumption was that a minimum number of sites is blocked by NiS_x species on Ni(1.1)WS₂/γ-Al₂O₃, i.e., most W and Ni-promoted sites at the edges were exposed and detected. It follows that the number of Ni-promoted sites at the edge is proportional to the decrease in the intensity of the band of NO at non-promoted sites. This allowed assigning an apparent molar extinction coefficient to the NO bands at 1875 cm⁻¹ (promoted sites) of ~1 cm μmol⁻¹. For the samples with higher Ni loadings, the number of edge atoms being

blocked was obtained by subtracting the number of W and Ni atoms exposed (ex-situ IR spectra) from the total number of edge atoms (TEM analysis).

2.7 Reference for Supporting Information

- (1) Shigesato, Y.; Murayama, A.; Kamimori, T.; Matsuhira, K. *Appl. Surf. Sci.* **1988**, *33*, 804–811.
- (2) Gabrusenoks, J. V.; Cikmach, P. D.; Lusiš, A. R.; Kleperis, J. J.; Ramans, G. M. *Solid State Ionics* **1984**, *14* (1), 25–30.
- (3) Lee, S.-H.; Cheong, H. M.; Tracy, C. E.; Mascarenhas, A.; Benson, D. K.; Deb, S. K. *Electrochim. Acta* **1999**, *44* (18), 3111–3115.
- (4) van der Vlies, a. J.; Kishan, G.; Niemantsverdriet, J. W.; Prins, R.; Weber, T. *J. Phys. Chem. B* **2002**, *106* (13), 3449–3457.
- (5) Horsley, J. A.; Wachs, I. E.; Brown, J. M.; Via, G. H.; Hardcastle, F. D.; Wachs, E.; Brown, J. M.; Via, G. H.; Hardcastle, F. D.; Wachs, I. E.; Brown, J. M.; Via, G. H.; Hardcastle, F. D. *J. Phys. Chem.* **1987**, *91* (15), 4014–4020.
- (6) Vuurmant, M. a; Wachs, I. E. *J. Phys. Chem.* **1992**, *96* (12), 5008–5016.
- (7) Cordoba-Torresi, S. I.; Gabrielli, C.; Hugot-Le Goff, A.; Torresi, R. *J. Electrochem. Soc.* **1991**, *138* (6), 1548–1553.
- (8) Fournier, M.; Louis, C.; Che, M.; Chaquin, P.; Masure, D. *J. Catal.* **1989**, *119* (2), 400–414.
- (9) Weber, R. S. *Effect of Local Structure on the UV-Visible Absorption Edges of Molybdenum Oxide Clusters and Supported Molybdenum Oxides*; Academic Press, 1995; Vol. 151.
- (10) Klepel, O.; Böhlmann, W.; Ivanov, E. B. B.; Riede, V.; Papp, H. *Microporous Mesoporous Mater.* **2004**, *76* (1), 105–112.
- (11) Topsøe, N.-Y.; Topsøe, H. *J. Catal.* **1982**, *75*, 354–374.
- (12) Portela, L.; Grange, P.; Delmon, B. *Journal of Catalysis*. 1995, pp 243–254.
- (13) Puxley, D. C.; Kitchener, I. J.; Komodromos, C.; Parkyns, N. D. *Preparation of Catalysts III - Scientific Bases for the Preparation of Heterogeneous Catalysts*; Studies in Surface Science and Catalysis; Elsevier, 1983; Vol. 16.
- (14) Platero, E. E.; Spoto, G.; Zecchina, A. *J.Chem.Soc.Faraday Trans. 1* **1985**, *81*

- (5), 1283.
- (15) Reinhoudt, H. R.; Crezee, E.; a.D. van Langeveld; Kooyman, P. J.; van Veen, J. a. R.; Moulijn, J. a. *J. Catal.* **2000**, *196* (2), 315–329.
- (16) Sun, M.; Urgi, T.; Cattaneo, R.; van Langeveld, D.; Prins, R.; Bürgi, T.; Cattaneo, R.; van Langeveld, D.; Prins, R. *J. Catal.* **2001**, *201* (2), 258–269.
- (17) Amsterdam, U. **2002**, No. 14846.
- (18) Reinhoudt, H. R.; van Langeveld, a. D.; Kooyman, P. J.; Stockmann, R. M.; Prins, R.; Zandbergen, H. W.; Moulijn, J. a. *J. Catal.* **1998**, *179* (2), 443–450.
- (19) Scheffer, B.; Mangnus, P. J.; Moulijn, J. a. *J. Catal.* **1990**, *121* (1), 18–30.
- (20) Coulier, L.; Kishan, G.; Van Veen, J. a R.; Niemantsverdriet, J. W. *J. Phys. Chem. B* **2002**, *106* (23), 5897–5906.
- (21) Reinhoudt, H. R.; der Meer, Y.; der Kraan, A. M.; Van Langeveld, A. D.; Moulijn, J. A. *Fuel Process. Technol.* **1999**, *61* (1), 43–54.
- (22) Grimblot, J.; Bonnelle, J. P. *Catal. Today* **1988**, *4*, 57–70.
- (23) Reinhoudt, H. R.; van Langeveld, A. D.; Mariscal, R.; de Beer, V. H. J.; van Veen, J. A. R.; Sie, S. T.; Moulijn, J. A. In *Hydrotreatment and Hydrocracking of Oil Fractions Proceedings of the 1st International Symposium/6th European Workshop*; G.F. Froment, B. D., Grange, P., Eds.; Studies in Surface Science and Catalysis; Elsevier, 1997; Vol. 106, pp 263–271.
- (24) Diemann, E.; Weber, T.; Muller, A. *J. Catal.* **1994**, *148* (1), 288–303.
- (25) Hensen, E. J. M. J. M.; Kooyman, P. J. J.; van der Meer, Y.; a.M. van der Kraan; de Beer, V. H. J. H. J.; van Veen, J. a. R.; van Santen, R. a.; van der Kraan, A. M.; de Beer, V. H. J. H. J.; van Veen, J. a. R.; van Santen, R. a. *J. Catal.* **2001**, *199* (2), 224–235.
- (26) Schachtl, E.; Zhong, L.; Kondratieva, E.; Hein, J.; Gutiérrez, O. Y.; Jentys, A.; Lercher, J. A. *ChemCatChem* **2015**, *7* (24), 4118–4130.
- (27) Lee, C.; Yan, H.; Brus, L. E.; Heinz, T. F.; Hone, J.; Ryu, S. *ACS Nano* **2010**, *4* (5), 2695–2700.

- (28) Chung, J. W.; Adib, A.; Dai, Z. R.; Adib, K.; Ohuchi, F. S. *Thin Solid Films* **1998**, 335 (1), 106–111.
- (29) Schachtl, E.; Kondratieva, E.; Gutiérrez, O. Y.; Lercher, J. A. *J. Phys. Chem. Lett.* **2015**, 6 (15), 2929–2932.
- (30) Topsøe, N.-Y.; Topsøe, H.; Massoth, E. F. *J. Catal.* **1989**, 255, 252–255.
- (31) Travert, A.; Maugé, F. *Stud. Surf. Sci. Catal.* **1999**, 127, 269–277.
- (32) Oliviero, L.; Vimont, A.; Lavalley, J.-C. J.-C.; Sarria, F. R.; Gaillard, M.; Maugé, F.; Romero Sarria, F.; Gaillard, M.; Maugé, F. *Phys. Chem. Chem. Phys.* **2005**, 7 (8), 1861.

2.8 Associated Content

Contributions: Dr. Oliver Y. Gutiérrez and Dr. Hui Shi supervised this work. Dr. Eva Schachtl contributed with the design of the infrared spectrometer. Wanqiu Luo contributed with the design of the reactors, preparation of the samples, operation of setups, data analysis, and draft writing. Prof. Dr. Johannes A. Lercher was responsible for data discussion, supervising and manuscript preparation. Dr. Hui Shi and Prof. Dr. Johannes A. Lercher are the principal investigators of this work.

Acknowledgement: This work is financially supported by the Chevron Energy Technology Company. The authors would like to thank Drs. Alexander Kuperman, Axel Brait, and Jinyi Han for fruitful discussions, Dr. Marianne Hanzlik for TEM measurements and Xaver Hecht for technical support. We also thank Professor Gary L. Haller (Yale University) for his careful reading of the manuscript and helpful suggestions.

Chapter 3

Maximizing active site concentrations at Ni-substituted WS₂-edges for hydrogenation of polyaromatic

Abstract: Excessive presence of Ni led to the formation of NiS_x species, which reduced the fraction of Ni sites at the WS₂ edges and had detrimental impact on the hydrotreating activities of the γ -Al₂O₃-supported Ni-WS₂. HCl-treatment has been applied to remove NiS_x particles. The influences from this treatment on the hydrogenation of phenanthrene as example of polyaromatic compounds have been explored. Ni substitutes W at the WS₂ edge with a higher concentration in the Ni-WS₂ phase, which was hindered by NiS_x before. Leached Ni-WS₂/ γ -Al₂O₃ was up to 5-times as active as the parent material, with a higher exposure of active metal-edges hence a higher coverage of active H at the edges.

3.1 Introduction

Transition metal sulfide (TMS) catalysts supported on γ -Al₂O₃, e.g., Co(Ni)Mo(W)/ γ -Al₂O₃, have been commonly applied in refineries for hydrotreating crude oil, in the context of depleting reserves and more stringent environmental regulations.^{1–4} The promotional effects of Ni and Co in such catalytic systems have been ascribed to the formation of a mixed phase, i.e. Co(Ni)-Mo(W)-S phase where Co(Ni) atoms substitute Mo(W) atoms in MoS₂ or WS₂ slabs at the edges,^{3,5,6} where hydrotreating reactions take place.^{7–10} In addition, Ni-W combinations are known to be more efficient in hydrogenation than Mo- and Co-based counterparts.^{3,11,20–29,12–19} However, the studies on Ni-WS₂ catalysts remain inadequate at a molecular scale than on their Ni-MoS₂ homologues, and their intrinsic performances, still far from being optimal, thus remain to be improved.

The impact of Ni on the shape and stacking height of sulfide slabs, as well as on catalytic activity, has been discussed over decades.^{13,20,30–33} The principal positive effect of Ni on the concentration of functional groups at active edges (S-vacancies and SH groups) and its consequences for catalytic rates have been established.^{20,33–37} Several studies reported that a maximum decoration degree at the edge in NiMo(W)S₂ of Ni/Metal = 1:3,^{20,35,38,39} which coincides with a maxima promotion effect from Ni-Mo(W)S₂ with Ni/(Ni+Mo) = 0.3-0.5 obtained by several different groups.^{13,20,35,39–41} Few studies suggested a higher degree (around 50%) of Ni decorating on MoS₂/WS₂ could be achieved.^{9,42} However, disorder of Ni-Mo(W)S₂ phase and undue NiS_x formation have always obscured the quantitative structure–activity relationship of the Ni promoters at the MoS₂ or WS₂ edge, hence revealing the intrinsic activity of each Ni promoting site is still a challenging task.

NiS_x segregation, which is thermodynamically favored,^{39,43–46} from the active edge was reported in Ni-promoted MoS₂ or WS₂ after sulfidation as well as in spent catalysts after long period of utilization.^{43,47–49} Experimental results and theoretical calculation shows that the sintering of Ni to form Ni₃S₂ (heazlewoodite) is mostly common^{46,48,50–52} when the mixed phase of NiMo(W)S₂ becomes unstable. These crystals (with diameter from 5 nm to few hundreds of nm) decreased surface area and pore volume^{39,53} hence decrease the activities of the catalysts in hydrotreating reactions³⁵. This inevitably process can be slowed down by high initial MoS₂(WS₂) dispersion and good Ni-Mo(W) mixing³⁹. In addition, Duchet et al.^{54,55} reported a post-synthetic method to remove some of the bulky NiS_x crystals on Ni-MoS₂/ γ -Al₂O₃, while leaving the MoS₂ phase untouched. This procedure could reduce the blockage of active surfaces by NiS_x, to some extent, which is conducive to probing the actual activity of Ni-promoting sites on MoS₂ or WS₂.

The target of the following work would be, therefore, to qualitatively and quantitatively elucidate the structure-activity relation of the γ -Al₂O₃ supported Ni-WS₂ catalysts with minimum effect from inactive NiS_x particles using a post-synthesis acid treatment, i.e., leaching by concentrated hydrochloric acid solution. Its impact on the surface properties of the γ -Al₂O₃ supported sulfides was investigated using IR spectroscopy with adsorption of CO, NO, pyridine, and 2,6-dimethylpyridine. The catalysts were tested for the hydrogenation of phenanthrene (as a model for polyaromatic compounds) in the absence of defunctionalization pathways. The reaction data showed that the activities of the leached catalysts were increased by up to a factor of 5 compared to the parent ones. In addition, the activities linearly correlated with the measured Ni/(Ni+W) molar ratio, which was distinct from the volcano trend reported in the literature. Combining the kinetic analysis and characterizations allowed us to address the correlation between the structure changes and enhanced hydrogenation activity of polyaromatics after the acid treatment.

3.2 Experimental Section

3.2.1 Catalysts Preparation

Non-promoted and Ni-promoted WS₂/ γ -Al₂O₃, which had been used in a previous study,³⁴ are employed in this work as the parent materials, with their physiochemical properties provided in supporting information (Table 3.3 and Figure 3.4). Before the HCl treatment, sulfidation of the oxide precursor was performed in a continuous-flow trickle bed reactor (\varnothing 1/4-inch glass-coated stainless-steel tube) in a H₂S/H₂ gas mixture (20 ml min⁻¹, and 10 vol. % H₂S) at 20 bar and 673 K for 8 h. The catalyst precursor (300 mg, powder) was diluted with SiC (0.1 g, 500-1000 μ m) and placed in the isothermal region of the reactor, while the remaining reactor volume was filled by SiC.

Leaching of Ni-substituted WS₂/ γ -Al₂O₃ was performed as described in ref^{54,55} to remove NiS_x species. Briefly, 200 mg of sulfide material was treated with 10 ml hydrochloric acid (concentrated, \geq 37 wt.%, Aldrich; [H⁺] = ca. 12 M or pH = -1.1) at room temperature for 24 h with continuous stirring. Afterwards, the HCl-treated material was rinsed with excess water and dried overnight at 353 K. The resultant materials were denoted as Ni(x)WS₂/ γ -Al₂O₃-a, with x standing for the Ni loading in wt.% of the corresponding parent material.

In a series of control experiments, Ni(3.2)WS₂/ γ -Al₂O₃, Ni(4.5)WS₂/ γ -Al₂O₃ and Ni(11.1)WS₂/ γ -Al₂O₃ were treated in diluted HCl (1 mol L⁻¹, pH = 1) at room temperature for 24 h, and the resultant materials were denoted as Ni(3.2)WS₂/ γ -Al₂O₃-b,

Ni(4.5)WS₂/γ-Al₂O₃-b and Ni(11.1)WS₂/γ-Al₂O₃-b, respectively. Again, the number in the parenthesis refers to the Ni loading (in wt.%) in the corresponding parent sample.

The preparation of HCl-treated γ-Al₂O₃ (denoted as Cl-Al₂O₃) supported Ni-WS₂: γ-Al₂O₃ (surface area of 248 m² g⁻¹, pore volume of 0.67 cm³ g⁻¹) was immersed in HCl (1 mol L⁻¹) for 30 min, leading to the deposition of 0.8 wt.% of Cl (elemental analysis) onto the support. After pretreatment in flowing synthetic air (100 ml min⁻¹) at 833 K for 2 h, the Cl-containing γ-Al₂O₃ was impregnated with aqueous solutions of ammonium metatungstate hydrate (≥99.0%, Aldrich) and nickel nitrate (≥98.5%, Aldrich) by stepwise incipient wetness impregnation. After each impregnation step, the materials were dried at 393 K for 4 h and calcined at 773 K in flowing synthetic air (100 ml min⁻¹) for 4 h. The resulting oxide precursors contain 1 mmol W per gram of catalyst while the Ni loading was varied between 0.38 mmol and 1.57 mmol per gram of catalyst. These materials were denoted as Ni(x)WO₃/Cl-Al₂O₃ and Ni(x)WS₂/Cl-Al₂O₃, respectively, for the oxide precursors and sulfided catalysts.

3.2.2 Catalysts Characterization

The BET specific surface and pore volume were determined by N₂ adsorption–desorption at 77 K using a Thermo Finnigan Sorptomatic 1990 series instrument. The samples were pretreated in vacuum at 573 K for 2 h before adsorption measurements. The elemental analysis for the oxide precursors was performed at the Microanalytical Laboratory at Technische Universität München, using atomic absorption spectroscopy (AAS), CHNS-analysis, and potentiometric titration.

Transmission electron microscopy (TEM) pictures were taken on a JEOL JEM-2011 instrument equipped with an acceleration voltage of 120 kV. Specimens of fully sulfided catalysts were dispersed in ethanol and deposited on copper grids with supporting carbon films. At least 350 WS₂ slabs in the micrographs of each sample were counted for the statistical analysis of length and stacking degree.

Powder X-ray diffraction (XRD) patterns were acquired in a Phillips X'Pert PRO system (Cu Kα1, wavelength = 0.154056 nm) operating at 40 kV and 45 mA. The samples were measured with a scan rate of 1° min⁻¹ (2θ).

Infrared spectra of catalysts with adsorbed probe molecules were collected on a Nicolet 6700 FT-IR spectrometer with a MCT detector and a scanning resolution of 4 cm⁻¹. A stainless-steel IR cell allowed the in-situ sulfidation of the samples at high pressure and temperature (up to 20 bar and 673 K) and the subsequent adsorption of probe mole-

cules at low temperature in high vacuum (down to 123 K and 10⁻⁸ mbar). In each measurement, the oxide precursors or leached sulfides were diluted with γ -Al₂O₃ (weight ratio of 1:3), ground, and pressed into self-supporting wafers (ca. 4 mg cm⁻²). Each wafer was placed into the IR cell and evacuated under vacuum (10⁻⁸ mbar). Afterwards, the sample was (re-)sulfided in situ at 20 bar and 673 K for 2 h in a flow of 10 vol. % H₂S in H₂ (20 ml min⁻¹). The sulfidation was followed by flushing with a He flow (20 ml min⁻¹) for 10 min and evacuation at 10⁻⁸ mbar and 673 K for 1 h. Absorbance spectra were normalized to the weight of the wafers, background-subtracted, and processed with the software GRAMS.

NO adsorption: At 303 K after pretreatment, NO (10 vol. % NO/He) was dosed into the IR cell up to an equilibrium pressure of 1 mbar (i.e., 0.1 m bar NO). A series of spectra were recorded while NO was being admitted into the cell.

CO adsorption: To enhance the cooling efficiency, 1 bar of He was first introduced into the cell before cooling the cell with liquid N₂. When the temperature reached 123 K, CO at an equilibrium pressure of 1 mbar was dosed into the cell after outgassing. IR spectra were recorded until no changes in the spectra were observed. The IR bands of adsorbed CO species were obtained by subtracting the spectra measured after CO introduction by the one under vacuum.

2,6-dimethylpyridine adsorption: Small doses of 2,6-dimethylpyridine (denoted as DMP, $\geq 99.7\%$, Aldrich) were admitted to the cell at 323 K, up to the equilibrium pressure of 0.5 mbar. Evacuation under 10⁻³ mbar was performed for 30 min before recording the spectra. 1 bar of H₂ was dosed to the cell and another set of spectra was collected. The concentrations of protonated DMP were calculated using the molar extinction coefficient $\epsilon_{\nu_{8a}} = 6.5 \text{ cm } \mu\text{mol}^{-1}$ for the band at around 1625 cm⁻¹.⁵⁶

Pyridine adsorption: at 323 K, pyridine (Aldrich, $\geq 99.0\%$) was admitted to the cell at an equilibrium pressure of up to 0.5 mbar. Evacuation was applied under 10⁻⁷ mbar for 30 min, and a spectrum was recorded. Desorption of pyridine was performed by increasing temperature (up to 623 K with 5 K min⁻¹) with evacuation before a spectrum was taken. The surface concentrations of coordinated pyridine were calculated using the molar extinction coefficient of 0.73 cm μmol^{-1} determined for the characteristic band at 1450-1455 cm⁻¹ (pyridine adsorbed at Lewis acid sites).

3.2.3 Kinetic Measurements

The hydrogenation of phenanthrene was performed in a continuous-flow trickle bed reactor (\emptyset 1/4-inch glass-coated stainless-steel tube) with gas and liquid feeds supplied

by high-pressure mass flow controllers (Bronkhorst EL-FLOW) and a HPLC pump (Gilson 307), respectively. Prior to each run, the catalyst precursor (20 mg, 250-355 μm) or the leached material (15 mg, 250-355 μm) was diluted with SiC (600 mg, 63-90 μm) and placed in the isothermal region of the reactor. This catalyst bed was held in place by filling up the remaining reactor volume with SiC (63-90 μm). Sulfidation of the oxide precursor or re-sulfidation of the sulfide material was performed in-situ in a H₂S/H₂ gas mixture (20 ml min⁻¹, and 10 vol. % H₂S) at 20 bar and 673 K for 8 h. Catalytic tests were performed at 573 K, 60 bar, and H₂/hydrocarbon volumetric ratio of 300. The space time, defined as $m_{\text{cat}}/F_{\text{Phe}}$ (m_{cat} : weight of the catalyst; F_{Phe} : molar flow of phenanthrene), was varied by changing the flow rates of gas and liquid feeds. The liquid mixture contained 1 wt. % of phenanthrene (Alfa Aesar, 98%), 1000 ppm S as dimethyl disulfide (Aldrich, $\geq 99.0\%$), and 2 wt. % of n-tetradecane (Alfa Aesar, $\geq 99\%$; internal standard) in decahydronaphthalene (Merck Millipore, 98%). Liquid samples were collected with a multiport sampling valve and analyzed offline by a Shimadzu 2010 GC equipped with a HP-5 capillary column. Kinetic analysis was based on data acquired after 20 h time on stream when steady state had been reached.

3.3 Results and Discussion

3.3.1 Textual Properties of Acid-Treated Sulfide Materials

Compared to the parent sulfides (see supporting information Table 3.3, data taken from Ref.³⁴), Ni concentration was 33-62% lower in the acid-treated materials (at pH = -1 and 1) without appreciable losses of W, indicating a selective removal of Ni by HCl at room temperature (Table 3.1). Specifically, the Ni loss was 39-62% after concentrated HCl treatment (pH = -1), while the Ni loss was less pronounced after diluted HCl treatment (pH = 1). On the other hand, the changes in the Ni content did not lead to remarkable changes in the slab length and stacking degree, compared to the parent samples (representative TEM pictures in Figure 3.5). The crystalline structure of the WS₂ phase was retained after both concentrated and dilute HCl treatments, but the reflections from crystalline Ni₃S₂ phase were largely removed in both cases (see XRD in Figure 3.4 in supporting information). Moreover, for the series of samples subjected to the more severe acid-treatment (nomenclature ending with -a), the Ni loss in the Ni(1.1) sample was significantly lower than others to increase with the Ni loading, which is attributed to an increasing fraction of NiS_x at higher Ni loadings that is removed by the severe HCl treatment.

Table 3.1. Atomic Ni/(Ni+W) ratio, Ni loss (compared to the parent), and Cl content (before re-sulfidation) for the leached materials and the Cl-Al₂O₃ supported Ni-WS₂ samples. Note that the number in the parenthesis refers to the Ni loading (in wt.%) in the corresponding parent sample.

Catalyst	Ni/(Ni+W), mol/mol	Ni loss, %	Cl, wt. %
WS ₂ /γ-Al ₂ O ₃ -a	0	-	0.77
Ni(1.1)WS ₂ /γ-Al ₂ O ₃ -a	0.11	39	0.45
Ni(3.2)WS ₂ /γ-Al ₂ O ₃ -a	0.19	63	0.50
Ni(4.5)WS ₂ /γ-Al ₂ O ₃ -a	0.27	51	0.45
Ni(11.1)WS ₂ /γ-Al ₂ O ₃ -a	0.42	62	0.60
Ni(3.2)WS ₂ /γ-Al ₂ O ₃ -b	0.25	39	0.35
Ni(4.5)WS ₂ /γ-Al ₂ O ₃ -b	0.33	39	0.27
Ni(11.1)WS ₂ /γ-Al ₂ O ₃ -b	0.61	33	0.35
WS ₂ /Cl-Al ₂ O ₃	0	-	0.57
Ni(2.2)WS ₂ /Cl-Al ₂ O ₃	0.24	-	0.56
Ni(4.4)WS ₂ /Cl-Al ₂ O ₃	0.42	-	0.56
Ni(9.2)WS ₂ /Cl-Al ₂ O ₃	0.61	-	0.54

3.3.2 CO-IR and NO-IR Spectra on Acid-treated Materials and Chlorinated-Al₂O₃-supported Ni-WS₂

Figure 3.1(a-c) shows the IR spectra of CO adsorbed on three acid-treated (pH= -1) samples, WS₂/γ-Al₂O₃-a, Ni(3.2)WS₂/γ-Al₂O₃-a and Ni(11.1)WS₂/γ-Al₂O₃-a, together with the corresponding parent materials (see Figure 3.6 in supporting information for more spectra, including deconvoluted spectra, on other samples). All these spectra were recorded under an equilibrium pressure of 1 mbar at 123 K. The peak at 2197 cm⁻¹ was due to CO adsorbed on γ-Al₂O₃, while CO adsorption on the sulfide phase gave rise to bands in the range of 1950-2128 cm⁻¹. The deconvoluted peak at 2107 cm⁻¹ on the parent WS₂/γ-Al₂O₃ catalyst was attributed to CO adsorbed at non-promoted WS₂ (dashed lines in Figure 3.1a and Figure. 3.6a).^{13,57-61} This component was also present on the spectra of the Ni-WS₂ samples.

We should keep in mind that there is substantial ambiguity in reliable and irrefutable attribution of spectral components to the various adsorbed CO species on different sites. Studying a series of non-promoted and Ni-promoted WS₂/γ-Al₂O₃ samples at room temperature (instead of 123 K used in the present study), Duchet et al.⁵⁷ observed that CO adsorption on non-promoted WS₂/γ-Al₂O₃ led to bands centered at 2110 and 2060 cm⁻¹; on the other hand, they attributed the peaks at 2127, 2090 and 2073 cm⁻¹ on the Ni-

promoted WS₂/ γ -Al₂O₃ samples to adsorbed CO on W-atoms in the mixed Ni-W-S phase or a precursor phase where Ni is not fully incorporated into the promoted phase. In contrast, based on the fact that Ni substitution leads to an electron transfer from Ni to WS₂, Zuo et al.¹³ argued that this band at 2128 cm⁻¹ should not arise from a more electron-deficient W (in a mixed phase) compared to the unpromoted WS₂. Instead, they attributed it to the electron deficient Ni involved in the mixed Ni-W-S phase. Contrary to their observations, however, our attempts to deconvolute the spectra of the parent Ni-WS₂ samples never showed an appreciable presence of peaks centered at 2125-2128 cm⁻¹.

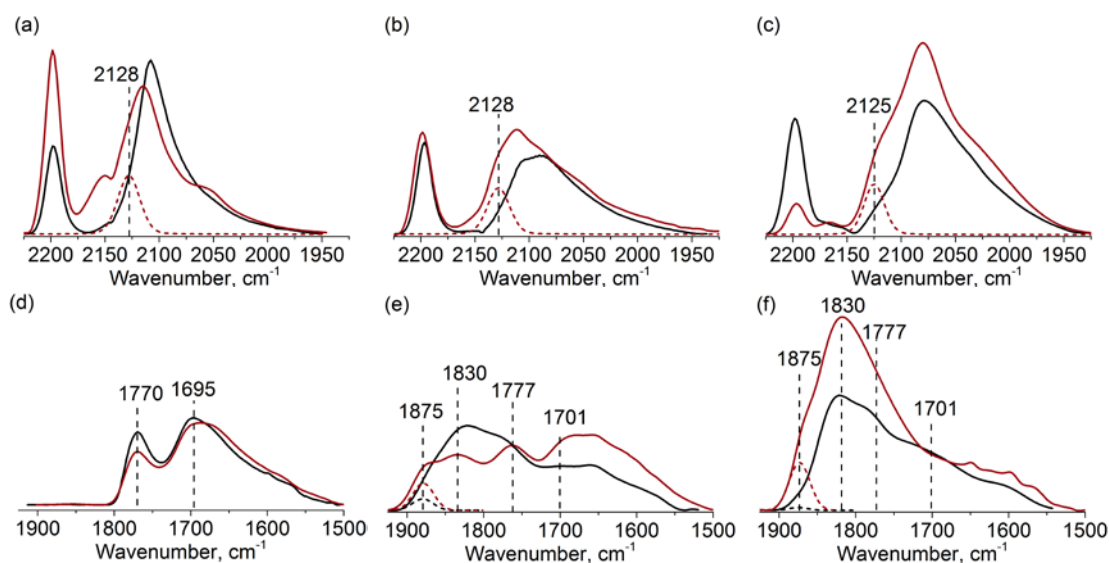


Figure 3.1. (Upper panels) Comparison of infrared spectra of CO adsorption on concentrated-HCl-treated materials: WS₂/ γ -Al₂O₃-a and the parent sample, WS₂/ γ -Al₂O₃ (a), Ni(3.2)WS₂/ γ -Al₂O₃-a and its parent Ni(3.2)WS₂/ γ -Al₂O₃(b), Ni(11.1)WS₂/ γ -Al₂O₃-a and its parent Ni(11.1)WS₂/ γ -Al₂O₃; (lower panels) comparison of infrared spectra of NO adsorption on leached material WS₂/ γ -Al₂O₃-a and the parent WS₂/ γ -Al₂O₃ (d), Ni(3.2)WS₂/ γ -Al₂O₃-a and its parent Ni(3.2)WS₂/ γ -Al₂O₃(e), Ni(11.1)WS₂/ γ -Al₂O₃-a and its parent Ni(11.1)WS₂/ γ -Al₂O₃(f). All the leached sulfides are labeled as red lines and the black lines represent the corresponding parent materials. The deconvoluted bands corresponding to CO adsorption on WS₂-edge with electron deficiency are shown in dashed lines in (a)-(c), while those corresponding to NO adsorption on edge-substituted Ni in the mixed Ni-W-S slab are shown with dashed lines in (d)-(f).

The CO adsorption spectra of the acid-treated (pH = -1) sulfides are distinct from those of parent materials (red traces). On WS₂/ γ -Al₂O₃-a, the band of CO adsorption at the slab edge of WS₂ shifted to a higher wavenumber (2128 cm⁻¹), indicating a greater electron deficiency of W. This is also observed on other leached materials containing Cl (Figure 3.1 and Figure 3.8 for deconvoluted spectra). The same shift is observed on WS₂/Cl-Al₂O₃ (Figure 3.7), indicating that Cl on the support is responsible for the upward

shift in the wavenumber for the corresponding adsorbed CO species. It is worth mentioning that adsorbed CO on NiS_x is still detected on the leached samples (2080-2084cm⁻¹, Figure 3.8), showing the existence of residual NiS_x after leaching.

The NO adsorption spectra allow semi-quantitative differentiation of three adsorbed species on materials having been treated in concentrated HCl (Figure 3.1(d-e), Figure 3.9 for more spectra with deconvolution): (i) NO adsorbed on oxidized Ni-substituted WS₂ edge site (1875 cm⁻¹); (ii) NO adsorbed on segregated NiS_x phase (1830 cm⁻¹); (iii) dinitrosyl species adsorbed on W⁴⁺ at the edges of WS₂ (symmetric stretching vibration at 1695 cm⁻¹ and asymmetric stretching vibration at 1775 cm⁻¹).^{34,41,62,63} On WS₂/γ-Al₂O₃-a (Figure 3.1d), the symmetric stretching of dinitrosyl at 1695 cm⁻¹ barely changed after leaching, indicating that the concentration of W⁴⁺ at the edge was retained, while the asymmetric one at 1770 cm⁻¹ decreased by 20%. Leached Ni-WS₂/γ-Al₂O₃ samples also show similar integrated areas on W⁴⁺ at the edges of WS₂ compared to parent materials (the 1695 cm⁻¹ trace, Figure 3.2a). More importantly, the area of the deconvoluted band at 1875 cm⁻¹ increases compared to that on parent materials, for example, by a factor of 2 on Ni(3.2)WS₂/γ-Al₂O₃-a and 18 on Ni(11.1)WS₂/γ-Al₂O₃-a. Thus, more Ni-W sites at the slab edges are exposed after the treatment in concentrated HCl. Meanwhile, the peak of adsorbed NO on NiS_x (at 1830 cm⁻¹) also becomes more intense for Ni/(Ni+W) ≥ 0.4, suggesting that leaching at such loadings led to smaller particle size of NiS_x (more surface NiS_x sites accessible to NO); these NiS_x might be so small that they appeared XRD-amorphous. It is unclear, however, how these small NiS_x particles were formed.

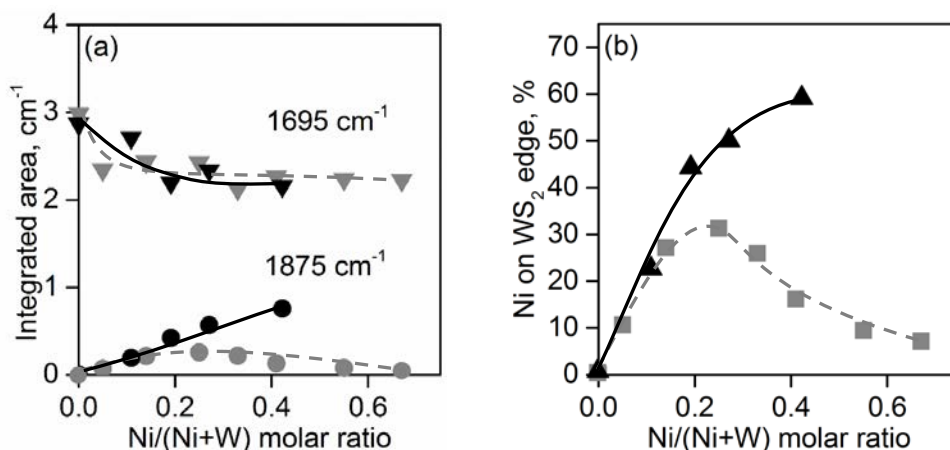


Figure 3.2. Comparison of the integrated areas in the spectra of NO adsorption at 1875 cm⁻¹ (●) and 1695 cm⁻¹ (▼)(a); Percentage of Ni decoration degree at the slab edge of (Ni)WS₂/γ-Al₂O₃-a (▲) and parent material Ni-WS₂/γ-Al₂O₃ (■) with increasing Ni content(b). All the leached sulfides Ni-WS₂/γ-Al₂O₃-a are labeled in black symbols with continuous

lines, while the grey symbols connected with dashed lines represent the corresponding parent materials Ni-WS₂/ γ -Al₂O₃.

The degree of Ni substitution at the edge was calculated by using molar extinction coefficients of 1.0 and 3.9 cm μ mol⁻¹ for the peaks at 1875 and 1695 cm⁻¹, respectively, for the model mentioned in ref.^{34,35}. The accessible metal fraction of Ni at the edge, Ni/(Ni+W), was calculated to be 44% on Ni(3.2)WS₂/ γ -Al₂O₃-a and 59% on Ni(11.1)WS₂/ γ -Al₂O₃-a (Figure 3.2b and Table 3.5 for the calculation results). Besides the increased exposure of metal sulfide edges by removing NiS_x particles, surface roughening of WS₂, possibly caused by concentrated acid treatment, and might have also contributed to the overall increase in the concentration of total metal atoms at the slab edge (Table 3.5).

3.3.3 Characterization of Acid Sites on the Sulfide Materials

Co-adsorption of a basic molecule (2,6-dimethylpyridine, DMP) and H₂ followed by IR spectroscopy was used to quantify the Brønsted acid site (BAS) concentration, i.e., the concentration of SH groups, for the HCl-treated (Ni-)WS₂/ γ -Al₂O₃ and the Cl-Al₂O₃-supported samples. Deconvoluted spectra are shown in Figure 3.11. Protonated DMP gives rise to vibration bands ν_{8a} (~1650 cm⁻¹) and ν_{8b} (~1627 cm⁻¹), the peaks at ~1615 and 1580 cm⁻¹ result from DMP coordinated to Lewis acid sites (LAS), and the bands at 1602 and 1580 cm⁻¹ correspond to weakly adsorbed DMP.^{56,64}

Co-adsorbing H₂ and DMP on the sulfide catalysts increased the intensity of the bands of protonated DMP (ν_{8a} and ν_{8b}). The concentrations of protonated DMP (in turn, the concentration of SH) on selected samples of HCl-treated sulfides are shown in Table 3.2, while those on the corresponding parent sulfides are provided in Table 3.6 for comparison. For WS₂/ γ -Al₂O₃ and Ni(1.1)WS₂/ γ -Al₂O₃, the concentration of SH barely changed after concentrated HCl treatment (82 μ mol g⁻¹ for WS₂/ γ -Al₂O₃ vs. 89 μ mol g⁻¹ for WS₂/ γ -Al₂O₃-a; 114 μ mol g⁻¹ for Ni(1.1)WS₂/ γ -Al₂O₃ and 119 μ mol g⁻¹ for Ni(1.1)WS₂/ γ -Al₂O₃-a). At higher Ni loadings, however, significantly more SH groups are created; for example, the SH concentration increased from 150 μ mol g⁻¹ on the parent Ni(3.2)WS₂/ γ -Al₂O₃ sample to 201 μ mol g⁻¹ on the concentrated-HCl-treated Ni(3.2)WS₂/ γ -Al₂O₃-a, and from 91 μ mol g⁻¹ on Ni(11.1)WS₂/ γ -Al₂O₃ to 354 μ mol g⁻¹ on Ni(11.1)WS₂/ γ -Al₂O₃-a. It is estimated that nearly 30% of this significant increase in SH concentration can be ascribed to the Cl-induced acidity, as Ni(9.2)WS₂/Cl-Al₂O₃ shows 183 μ mol g⁻¹ of SH groups.

Table 3.2. Concentration of protonated DMP before and after co-adsorption of H₂ and the concentration of pyridine adsorbed on Lewis acid sites (LAS) after out-gassing at 623 K and 10⁻⁷ mbar.

Catalyst	As sulfided μmol g ⁻¹	After H ₂ , μmol g ⁻¹	Strong LAS, μmol g ⁻¹
WS ₂ /γ-Al ₂ O ₃ -a	79	89	91
Ni(1.1)WS ₂ /γ-Al ₂ O ₃ -a	78	119	104
Ni(3.2)WS ₂ /γ-Al ₂ O ₃ -a	123	201	132
Ni(4.5)WS ₂ /γ-Al ₂ O ₃ -a	157	278	178
Ni(11.1)WS ₂ /γ-Al ₂ O ₃ -a	297	354	215
Ni(11.1)WS ₂ /γ-Al ₂ O ₃ -b	101	210	148
WS ₂ /Cl-Al ₂ O ₃	76	90	83
Ni(9.2)WS ₂ /Cl-Al ₂ O ₃	121	183	121
Cl-Al ₂ O ₃	52	58	68

The concentration of SH groups on Ni-related sites on the edge was proved to be in linear correlation with the PHE hydrogenation activity over the Ni-MS₂/γ-Al₂O₃ (M stands for Mo or W),³⁴ indicating that they are the active species. Similarly, the concentration of SH groups on the Ni-promoted phases in the leached materials was obtained by subtracting that of the unpromoted WS₂ from the total SH concentration, the results are listed in Table 3.7, as a criteria for the amount of active species on leached LAS materials.

Adsorption of pyridine followed by IR spectroscopy as well as desorption at 623 K was performed on leached Ni-WS₂/γ-Al₂O₃ in order to assess strong acid site concentrations and their strength in selected materials (deconvoluted spectra in Figure 3.12). Compared to the spectra on the parent materials, the band at 1450 cm⁻¹ slightly shifted to ca. 1455 cm⁻¹ for all acid-treated samples. The concentrations of LAS after desorption at 623 K, i.e., classified as strong LAS, are listed in Table 3.2. For comparison, the concentrations of the strong LAS on parent sulfides are provided in Table 3.6. On all the sulfides after HCl treatment, the increase in the concentration of strong LAS is conspicuous, ranging from 28% to 241% compared to such concentrations in the parent samples. It is worth noticing that Cl-Al₂O₃ already has 68 μmol g⁻¹ strong LAS in comparison to 33 μmol g⁻¹ on the pure γ-Al₂O₃, which is in agreement with some previous studies,⁶⁵⁻⁷¹ and such Cl-induced effects are also observed on WS₂/Cl-Al₂O₃ and Ni(9.2)WS₂/Cl-Al₂O₃, containing 83 and 121 μmol g⁻¹ strong LAS, respectively.

3.3.4 Hydrogenation of Phenanthrene over Leached and Chlorided-Al₂O₃ supported Ni-WS₂

The catalytic activities of Ni-WS₂/Al₂O₃ that had been subjected to treatments in concentrated and dilute HCl was evaluated in the hydrogenation of phenanthrene (denoted as PHE). Figure 3a plots the reaction rate of PHE hydrogenation as a function of the measured atomic Ni/(Ni+W) ratio among different series of materials. The model compound, PHE, is representative of the polycyclic aromatic hydrocarbons which are hydrogenated during the processing of heavy feeds. The PHE conversion as a function of space time on the leached Ni-WS₂/γ-Al₂O₃ catalysts is shown in Figure 3.13, in addition, Table 3.9 includes the reactions rates over all the catalysts mentioned in this work. Products from ring opening and multiple hydrogenolysis reactions were not detected in any case. Hydrogenation produces 9,10-dihydrophenanthrene (DiHPhe), 1,2,3,4-tetrahydrophenanthrene (TetHPhe) as primary products, while 1,2,3,4,5,6,7,8-octahydrophenanthrene (*sym*OHPhe), and 1,2,3,4,4a,9,10,10a-octahydrophenanthrene (*asym*OHPhe) are mechanistically secondary products. The reaction network under these conditions comprises two main routes^{34,35}, i.e., initial hydrogenation at the middle ring (PHE → DiHPhe → *asym*OHPhe) and initial hydrogenation at a lateral ring (PHE → TetHPhe → *sym*OHPhe), and the rates of these two routes are denoted as r_1 and r_2 , respectively. This is in agreement with the observations on Ni-MoS₂/γ-Al₂O₃³⁵ and Ni-WS₂/γ-Al₂O₃.³⁴ The yields and selectivities of the products as a function of PHE conversion are shown in Figure 3.14 and 3.15 in supporting information.

Concentrated-HCl-treatment of the non-promoted WS₂/γ-Al₂O₃ did not change its hydrogenation activity, as the hydrogenation rate and selectivity remained identical over WS₂/γ-Al₂O₃-a (0.45 mmol h⁻¹ g_{cat}⁻¹, Table 3.9 and Figure 3.3a). For Ni(1.1)WS₂/γ-Al₂O₃-a, the mass specific activity was also nearly identical to its parent counterpart despite a Ni loss of 39%. For all catalysts, the product distribution hardly changed after the “severe” HCl treatment (Figure 3.15 and Table 3.9).

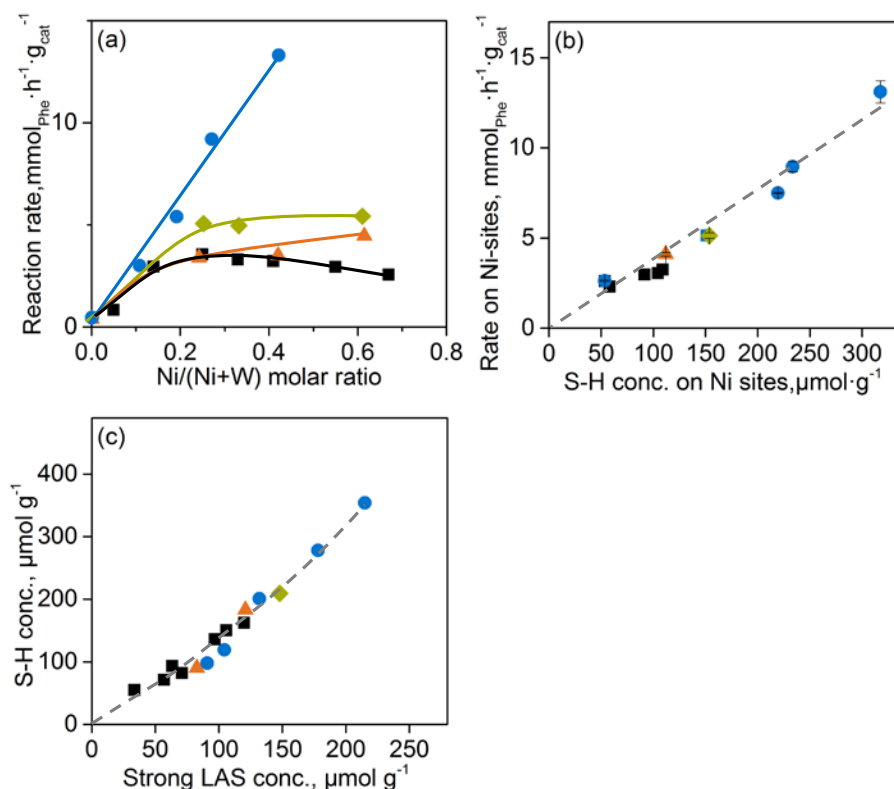


Figure 3.3. (a) Reaction rates of phenanthrene hydrogenation as a function of the measured Ni/(Ni+W) molar ratio, (b) correlation between the specific reaction rates and S-H concentration on Ni-sites (c) correlation between S-H concentration and strong LAS concentration on parent materials Ni-WS₂/ γ -Al₂O₃ (data points labeled with black marker ■), sulfides leached by concentrated HCl Ni-WS₂/ γ -Al₂O₃-a (blue ●), sulfides leached at pH=1 Ni-WS₂/ γ -Al₂O₃-b (green ◆) and Ni-WS₂/Cl-Al₂O₃ (orange ▲). The data of parent materials Ni-WS₂/ γ -Al₂O₃ was taken from Ref ³⁴. The single green symbol in (b) and (c) is Ni(11.1)WS₂/ γ -Al₂O₃-b, and the single orange symbol in (b) is Ni(9.2)WS₂/Cl-Al₂O₃, while the two orange symbols in (c) are WS₂/Cl-Al₂O₃ and Ni(9.2)WS₂/Cl-Al₂O₃.

For samples with higher Ni contents, hydrogenation rates were increased, which was attributed to the presence of catalytically inactive NiS_x on WS₂ edges (NiS_x/ γ -Al₂O₃ and leached NiS_x/ γ -Al₂O₃ had only an activity of 3 $\mu\text{mol} \cdot \text{h}^{-1} \cdot \text{g}_{\text{cat}}^{-1}$).³⁴ As illustrated in Figure 3, removing NiS_x led to remarkable rate enhancements in the hydrogenation of PHE, if compared to the parent material (Table 3.3) with Ni/(Ni+W) \geq 0.3. Compared to the parent material Ni(3.2)WS₂/ γ -Al₂O₃ (3.3 $\text{mmol} \cdot \text{h}^{-1} \cdot \text{g}_{\text{cat}}^{-1}$), a higher PHE conversion rate of 5.4 $\text{mmol} \cdot \text{h}^{-1} \cdot \text{g}_{\text{cat}}^{-1}$ was achieved on Ni(3.2)WS₂/ γ -Al₂O₃-a. At the highest Ni loading studied, the rate measured on Ni(11.1)WS₂/ γ -Al₂O₃-a was more than five-fold that of the parent one. It is also noticeable that the mass specific rate linearly increased with the actual Ni/(Ni+W) atomic ratio for the series subjected to concentrated HCl treatment (Figure 3.3a), distinctly different from the well-known volcano plot with the maximum

promotion effect in HDS and HDA appearing at Ni/(Ni+W)~0.3.^{13,20,35,39–41} In the meantime, the product distribution slightly shifted in favor of path 2 with $r_1/r_2 \sim 0.6$ (i.e., more TetHPhe and symHPhe; Table 3.9). Repeating the “severe” acid treatment once more for Ni(11.1)WS₂/γ-Al₂O₃-a, however, led to a lowered activity of 7.8 mmol h⁻¹ g_{cat}⁻¹, due to additional loss of Ni from the active Ni-W-S phase, see Figure 3.9(i).

To understand the origin of activity enhancement in HCl-treated catalysts, hydrogenation of PHE was conducted on Ni-WS₂/γ-Al₂O₃-b (having been subjected to milder treatment in HCl solution with pH = 1) and Ni-WS₂/Cl-Al₂O₃ series, as plotted in Figure 3.3a for comparison. When the parent materials were treated at pH = 1, Ni(3.2)WS₂/γ-Al₂O₃-b, Ni(4.5)WS₂/γ-Al₂O₃-b and Ni(11.1)WS₂/γ-Al₂O₃-b showed similar activities. The ratio of r_1/r_2 on this series of catalysts was the same as on Ni-WS₂/γ-Al₂O₃-a with Ni/(Ni+W) ≥ 0.33 (Table 3.9). This indicates milder leaching condition (pH = 1) could already produce better catalysts for hydrogenation, albeit with a less pronounced improvement (by 51-112%). In contrast, a significantly higher catalytic activity (4.5 mmol h⁻¹ g_{cat}⁻¹) was only observed at Ni/(Ni+W) of 0.6 when chlorinated Al₂O₃ was used as the support (Figure 3.2a) with a similar product distribution as on parent materials (r_1/r_2 ratio ~ 1), but even in this case, the rate enhancement compared to the parent series was much smaller for a given Ni/(Ni+W). Thus, we conclude that the rate enhancement should be caused primarily by the removal of NiS_x, rather than effects of residual Cl on the surface. The specific activity of Ni-decorated WS₂ edge sites has been calculated by subtracting the contribution of non-promoted WS₂ edge sites (Table 3.7); a sample calculation is shown in the Supporting information. Figure 3.3b shows that there is a linear correlation between the specific rate and the concentration of SH groups associated with the Ni-substituted edge in a mixed Ni-W-S phase (with Brønsted acidity from Cl-containing Al₂O₃ and unpromoted WS₂ edge sites subtracted; a sample calculation is shown in SI) on parent, acid-treated (“severe” and “mild”) and Cl-Al₂O₃ supported catalysts, despite a slight deviation from the linearity at higher SH concentrations. This observations lends support to the conclusion that the site-normalized activity of surface SH is identical across different Ni-WS₂ samples, regardless of the Cl content and the concentration of segregated NiS_x phases.

3.3.5 Effects from γ-Al₂O₃ and Cl-Al₂O₃ Supports

All the samples after the HCl treatment contained Cl on γ-Al₂O₃ even after extensive rinsing cycles with pure water (Table 3.1). The Cl content was relatively similar for a given series of samples, regardless of the Ni loading. For the “severe”-acid-treatment series, the Cl contents varied between 0.12–0.17 mmol g⁻¹, whereas for the “mild”-acid-

treatment series, the Cl contents varied between 0.075–0.097 mmol g⁻¹. To investigate whether residual Cl influences the physicochemical properties and catalytic performance of the sulfide phase, Cl-Al₂O₃ was used as the support for synthesizing Ni-WS₂ catalysts, specifically, WS₂/Cl-Al₂O₃, Ni(2.2)WS₂/Cl-Al₂O₃, Ni(4.4)WS₂/Cl-Al₂O₃, Ni(9.2)WS₂/Cl-Al₂O₃ with 0.15-0.16 mmol g⁻¹ of Cl (Table 3.1).

IR spectra of CO and NO adsorption on WS₂/Cl-Al₂O₃ are largely similar to those measured on WS₂/γ-Al₂O₃-a (Figure 3.7), and the corresponding acidities (Table 3.2) are almost the same, which confirms that halogen on the support is responsible for the electron deficiency on WS₂-edge and the enhanced acid strength of LAS.^{8,72–74} However, no positive effect was shown on the catalytic activity of this series except for Ni(9.2)WS₂/Cl-Al₂O₃. In all cases, the selectivities as well as the apparent activation energy remained identical for hydrogenation of phenanthrene (Figure 3.16 in supporting information). Hence, the residual Cl only marginally contributes to the increase of the activity on leached sulfides.

3.3.6 Effect of the Acid Treatment on Metal Sulfide Phase

39-63% of Ni was removed from the parent sulfide materials by treatment with concentrated HCl. It is speculated that the removed Ni species were present as NiS_x that had blocked the active Ni- and W-sites at the edge and some NiS_x dispersed on γ-Al₂O₃. Ni(11.1)WS₂/γ-Al₂O₃-a showed the highest degree of Ni substitution (59%), which exceeds the postulated optimum in the well-accepted “NiMoS” model. However, IR spectra with adsorption of CO and NO still show noticeable amount of NiS_x species on the surface that had undergone the acid treatment, indicating that even the “severe” HCl-treatment cannot eliminate all the NiS_x at room temperature, or somehow they re-form during re-sulfidation.

Concomitantly, the HCl treatment caused changes in the concentration of acid sites on the sulfide surfaces. Upon DMP adsorption, significantly higher concentrations of protonated DMP were observed after HCl treatment. The impact was the most significant on Ni(11.1)WS₂/γ-Al₂O₃-a, which is a direct result from the highest exposure of Ni-substituted and non-promoted WS₂-edge sites. On the other hand, the strength of LAS was increased, as indicated by adsorbed pyridine appearing at 1454 cm⁻¹ and the blueshift in the CO stretching vibration on WS₂.^{65,67,71,72} The stronger acid strength is ascribed to Cl on the alumina support,^{65–70} perhaps inducing electron deficiency to the WS₂ phase. However, this change in the electronic state of W showed negligible impacts on the catalytic properties of the Ni-promoted sites, as the specific reaction rates in PHE hydrogenation are still linearly correlated to the corresponding S-H concentration.

3.4 Conclusion

Leaching treatment with concentrated hydrochloric acid is applied to Ni-WS₂/γ-Al₂O₃, so as to remove NiS_x particles which is destructive for hydrogenation of polyaromatics. The impact of the leaching process was manifold. First of all, removal of NiS_x particles by concentrated hydrochloric acid cleans up the surface of the catalysts and significantly increases the concentration of exposed metal edges, for both WS₂ sites and Ni decorated sites with highest decoration degree up to 59%. This further benefits the concentration of S-H groups on the leached catalyst with up to 287% increment. The contribution of NiS_x removal was estimated to be 70%-80% to the overall rate enhancement for hydrogenation of phenanthrene. Another factor is that residue Cl brought by hydrochloric acid treatment was proved to be also positive for enhancement of the catalyst activity. It locates on the γ-Al₂O₃ support and improves the strength of acid sites, which further changes the electronic character of the sulfide particles. Therefore, WS₂ phase shows an electron deficiency after leaching, which has only a marginal for S-H groups and activity (20~30%), as it does not shift the selectivities noticeably nor does it change the apparent activation energy for hydrogenation of phenanthrene. Hence, one could conclude that the removal of NiS_x took precedence over other factors on the Ni-promoted WS₂/γ-Al₂O₃.

Leaching treatment as well allows us to better understand the promotion effect of Ni on WS₂/γ-Al₂O₃. Our work proves the decoration degree of Ni can exceed the well-known maxima 33%, which was not observed before due to blocking of NiS_x on the edges. Higher Ni bulk loading is beneficial for achieving higher decoration degree of Ni at the edges and hence exposing more active species for hydrogenation of polyaromatic compounds.

3.5 Reference

- (1) Chianelli, R. R.; Berhault, G.; Torres, B. *Catal. Today* **2009**, *147* (3–4), 275–286.
- (2) Toulhoat, H.; Raybaud, P. *Catalysis by Transition Metal Sulphides: From Molecular Theory to Industrial Application*; Technip, 2013.
- (3) Topsøe, H.; Clausen, B. S.; Massoth, F. E. *Hydrotreating catalysis*; Springer, 1996.
- (4) *Regulation (EC) No. 715/2007 of the European Parliament and of the Council*; 2007.
- (5) Topsøe, H.; Candia, R.; Topsøe, N.; Clausen, B. S.; Topsøe, H. *Bull. des Sociétés Chim. Belges* **1984**, *93* (8-9), 783–806.
- (6) Prins, R.; De Beer, V. H. J.; Somorjai, G. a. *Catal. Rev.* **1989**, *31* (1–2), 1–41.
- (7) Laurenti, D.; Phung-Ngoc, B.; Roukoss, C.; Devers, E.; Marchand, K.; Massin, L.; Lemaitre, L.; Legens, C.; Quoineaud, A. A.; Vrinat, M. *J. Catal.* **2013**, *297*, 165–175.
- (8) Gutiérrez, O. Y.; Singh, S.; Schachtl, E.; Kim, J.; Kondratieva, E.; Hein, J.; Lercher, J. A.; Han, W.; Nie, H.; Long, X.; Li, M.; Yang, Q.; Li, D. *ACS Catal.* **2014**, *4* (5), 1487–1499.
- (9) Eijsbouts, S.; Heinerman, J. J. L.; Elzerman, H. J. W. *Appl. Catal. A, Gen.* **1993**, *105* (1), 53–68.
- (10) Breyse, M.; Afanasiev, P.; Geantet, C.; Vrinat, M. *Catalysis Today*. Elsevier November 1, 2003, pp 5–16.
- (11) Van Der Meer, Y.; Vissenberg, M. J.; De Beer, V. H. J.; Van Veen, J. A. R.; Van Der Kraan, A. M. In *Industrial Applications of the Mössbauer Effect*, Cook, D. C., Hoy, G. R., Eds.; Springer Netherlands: Dordrecht, 2002; pp 51–57.
- (12) Hensen, E. J. M.; van der Meer, Y.; van Veen, J. A. R.; Niemantsverdriet, J. W. *Appl. Catal. A Gen.* **2007**, *322* (0), 16–32.
- (13) Zuo, D.; Vrinat, M.; Nie, H.; Maugé, F.; Shi, Y.; Lacroix, M.; Li, D. *Catal. today*

- 2004**, 93, 751–760.
- (14) Kameoka, T.; Yanase, H.; Nishijima, A.; Sato, T.; Yoshimura, Y.; Shimada, H.; Matsubayashi, N. *Appl. Catal. A Gen.* **1995**, 123 (2), 217–228.
- (15) Yoshimura, Y.; Sato, T.; Shimada, H.; Matsubayashi, N.; Imamura, M.; Nishijima, A.; Higo, M.; Yoshitomi, S. *Catal. Today* **1996**, 29 (1–4), 221–228.
- (16) Stanislaus, a.; Cooper, B. *Catal. Rev.* **1994**, 36 (May 2013), 75–123.
- (17) Zuo, D.; Li, D.; Nie, H.; Shi, Y.; Lacroix, M.; Vrinat, M. *J. Mol. Catal. A Chem.* **2004**, 211 (1), 179–189.
- (18) Sizova, I. A.; Serdyukov, S. I.; Maksimov, A. L.; Sinikova, N. A. *Pet. Chem.* **2015**, 55 (1), 38–44.
- (19) Kelly, S. D.; Yang, N.; Mickelson, G. E.; Greenlay, N.; Karapetrova, E.; Sinkler, W.; Bare, S. R. *J. Catal.* **2009**, 263 (1), 16–33.
- (20) Alphazan, T.; Bonduelle-Skrzypczak, A.; Legens, C.; Boudene, Z.; Taleb, A.-L.; Gay, A.-S.; Ersen, O.; Copéret, C.; Raybaud, P. *J. Catal.* **2016**, 340, 60–65.
- (21) R.J.H. Voorhoeve, J. C. M. S. *J. Catal.* **1971**, 252, 243–252.
- (22) Kim, C.-H.; Yoon, W. L.; Lee, I. C.; Woo, S. I. *Appl. Catal. A Gen.* **1996**, 144 (1–2), 159–175.
- (23) Scheffer, B.; Mangnus, P. J.; Moulijn, J. a. *J. Catal.* **1990**, 121 (1), 18–30.
- (24) Bensch, W. *Hydrotreating: Removal of Sulfur from Crude Oil Fractions with Sulfide Catalysts*; Elsevier Ltd., 2013; Vol. 7.
- (25) Navalikhina, M. D.; Krylov, O. V. *Russ. Chem. Rev.* **1998**, 67 (7), 587–616.
- (26) Reinhoudt, H. R.; van Langeveld, a. D.; Kooyman, P. J.; Stockmann, R. M.; Prins, R.; Zandbergen, H. W.; Moulijn, J. a. *J. Catal.* **1998**, 179 (2), 443–450.
- (27) Frank, J. P.; LePage, J. F. **1981**.
- (28) Grange, P. *Catal. Rev.* **1980**, 21 (777306419), 135–181.
- (29) Reinhoudt, H. R.; Troost, R.; van Schalkwijk, S.; van Langeveld, A. D.; Sie, S. T.; Schulz, H.; Chadwick, D.; Cambra, J.; de Beer, V. H. J.; van Veen, J. A. R.;

- Fierro, J. L. G.; Moulijn, J. A. *Stud. Surf. Sci. Catal.* **1997**, *106*, 237–244.
- (30) Nikulshin, P. a.; Salnikov, V. a.; Mozhaev, a. V.; Minaev, P. P.; Kogan, V. M.; Pimerzin, a. a. *J. Catal.* **2014**, *309*, 386–396.
- (31) Ding, S.; Jiang, S.; Zhou, Y.; Wei, Q.; Zhou, W. *J. Catal.* **2017**, *345*, 24–38.
- (32) Grønberg, S. S.; Šarić, M.; Moses, P. G.; Rossmeisl, J.; Lauritsen, J. V. *J. Catal.* **2016**, *344*, 121–128.
- (33) Chen, W.; Nie, H.; Li, D.; Long, X.; van Gestel, J.; Maugé, F. *J. Catal.* **2016**, *344*, 420–433.
- (34) Luo, W.; Shi, H.; Schachtl, E.; Gutiérrez, O. Y.; Lercher, J. A.; Willnecker, E.; Gutiérrez, O. Y.; Lercher, J. A. *Angew. Chemie Int. Ed.* **2018**, *0* (ja).
- (35) Schachtl, E.; Zhong, L.; Kondratieva, E.; Hein, J.; Gutiérrez, O. Y.; Jentys, A.; Lercher, J. A. *ChemCatChem* **2015**, *7* (24), 4118–4130.
- (36) Schachtl, E.; Kondratieva, E.; Gutiérrez, O. Y.; Lercher, J. A. *J. Phys. Chem. Lett.* **2015**, *6* (15), 2929–2932.
- (37) Popov, A.; Kondratieva, E.; Mariey, L.; Goupil, J. M.; El Fallah, J.; Gilson, J. P.; Travert, A.; Maugé, F. *J. Catal.* **2013**, *297*, 176–186.
- (38) Gao, Q.; Ofosu, T. N. K.; Ma, S. G.; Komvokis, V. G.; Williams, C. T.; Segawa, K. In *Catalysis Today*; Elsevier, 2011; Vol. 164, pp 538–543.
- (39) Eijsbouts, S.; Li, X.; Bergwerff, J.; Louwen, J.; Woning, L.; Loos, J. *Catal. Today* **2017**, *292*, 38–50.
- (40) Pratt, K. C.; Sanders, J. V.; Tamp, N. *J. Catal.* **1980**, *66* (1), 82–92.
- (41) Topsøe, N.-Y.; Topsøe, H. *J. Catal.* **1983**, *84* (2), 386–401.
- (42) Woolfolk, L. G.; Geantet, C.; Massin, L.; Laurenti, D.; De los Reyes, J. A. *Appl. Catal. B Environ.* **2017**, *201*, 331–338.
- (43) Guichard, B.; Roy-Auberger, M.; Devers, E.; Pichon, C.; Legens, C.; Lecour, P. *Catal. Today* **2010**, *149* (1–2), 2–10.
- (44) Guichard, B.; Roy-Auberger, M.; Devers, E.; Legens, C.; Raybaud, P. *Catal.*

- Today* **2008**, 130 (1), 97–108.
- (45) Krebs, E.; Silvi, B.; Raybaud, P. *Catal. Today* **2008**, 130 (1), 160–169.
- (46) Schweiger, H.; Raybaud, P.; Toulhoat, H. *J. Catal.* **2002**, 212 (1), 33–38.
- (47) Eijsbouts, S.; Van Den Oetelaar, L. C. A.; Van Puijenbroek, R. R. *J. Catal.* **2005**, 229 (2), 352–364.
- (48) Karroua, M.; Matralis, H.; Grange, P.; Delmon, B. *Bull. des Sociétés Chim. Belges* **2010**, 104 (1), 11–18.
- (49) Eijsbouts, S. *Appl. Catal. A Gen.* **1997**, 158 (1), 53–92.
- (50) Matsubayashi, N.; Sato, T.; Shimada, H.; Imamura, M.; Yoshimura, Y.; Nishijima, A.; Kameoka, T.; Masuda, K. *Coal Sci. Technol.* **1995**, 24, 1495–1498.
- (51) Kuriki, Y.; Yumura, M.; Ohshima, S.; Uchida, K.; Ikazaki, F. *Coal Sci. Technol.* **1995**, 24, 1347–1350.
- (52) Eijsbouts, S.; Van Gestel, J. N. M.; Van Veen, J. A. R.; De Beer, V. H. J.; Prins, R. *J. Catal.* **1991**, 131 (2), 412–432.
- (53) Yoosuk, B.; Kim, J. H.; Song, C.; Ngamcharussrivichai, C.; Prasassarakich, P. *Catal. Today* **2008**, 130 (1), 14–23.
- (54) J.C. Duchet, D. C. J. B. *Bull. Soc. Chim. Fr.* **1978**, 112–118.
- (55) J.C. Duchet, D. C. J. B. *Bull. Soc. Chim. Fr.* **1979**, 221–228.
- (56) Oliviero, L.; Vimont, A.; Lavalley, J.-C. J.-C.; Sarria, F. R.; Gaillard, M.; Maugé, F.; Romero Sarria, F.; Gaillard, M.; Maugé, F. *Phys. Chem. Chem. Phys.* **2005**, 7 (8), 1861.
- (57) Duchet, J.-C.; Lavalley, J.-C.; Housni, S.; Ouafi, D.; Bachelier, J.; Lakhdar, M.; Mennour, A.; Cornet, D. *Catal. Today* **1988**, 4 (1), 71–96.
- (58) Müller, B.; van Langeveld, a D.; Moulijn, J. A.; Knözinger, H.; Mueller, B.; van Langeveld, a D.; Moulijn, J. A.; Knoezinger, H. *J. Phys. Chem.* **1993**, 97 (35), 9028–9033.

- (59) Maugé, F.; Lavalley, J. C. *J. Catal.* **1992**, *137* (1), 69–76.
- (60) Ouafi, D.; Mauge, F.; Lavalley, J. C. *Bull. Soc. Chim. Fr.* **1989**, No. 3, 363–369.
- (61) Travert, A.; Dujardin, C.; Maugé, F.; Cristol, S.; Paul, J. F.; Payen, E.; Bougeard, D. *Catal. Today* **2001**, *70* (1–3), 255–269.
- (62) Reinhoudt, H. R.; Crezee, E.; a.D. van Langeveld; Kooyman, P. J.; van Veen, J. a. R.; Moulijn, J. a. *J. Catal.* **2000**, *196* (2), 315–329.
- (63) Ouafi, D.; Mauge, F.; Lavalley, J.-C.; Payen, E.; Kasztelan, S.; Houari, M.; Grimblot, J.; Bonnelle, J.-P. *Catal. today* **1988**, *4* (1), 23–37.
- (64) Travert, A.; Maugé, F. *Stud. Surf. Sci. Catal.* **1999**, *127*, 269–277.
- (65) Clet, G.; Goupil, J.-M.; Cornet, D. *Bull. Soc. Chim. Fr.* **1997**, *134* (2), 223–233.
- (66) Sharma, L. D.; Sinhamahapatra, P. K.; Sharma, H. R.; Mehrotra, R. P.; Balamalliah, G. *J. Catal.* **1977**, *48* (1–3), 404–407.
- (67) Melchor, A.; Garbowski, E.; Mathieu, M.-V.; Primet, M. *J. Chem. Soc. {,} Faraday Trans. 1* **1986**, *82* (6), 1893–1901.
- (68) Guillaume, D.; Gautier, S.; Despujol, I.; Alario, F.; Beccat, P. *Catal. Letters* **1997**, *43* (3), 213–218.
- (69) M., G. J.; L., J. E.; L., P. C.; J., V. R.; M., P. J. *J. Chem. Technol. Biotechnol.* **2007**, *38* (2), 105–113.
- (70) Corma, a.; Fornés, V.; Ortega, E. *J. Catal.* **1985**, *92* (2), 284–290.
- (71) Peri, J. B. *J. Phys. Chem.* **1966**, *70* (5), 1482–1491.
- (72) Breysse, M.; Cattenot, M.; Kougonas, V.; Lavalley, J. C.; Mauge, F.; Portefaix, J. L.; Zotin, J. L. *J. Catal.* **1997**, *168* (2), 143–153.
- (73) Sun, M.; Urgi, T.; Cattaneo, R.; van Langeveld, D.; Prins, R.; Bürgi, T.; Cattaneo, R.; van Langeveld, D.; Prins, R. *J. Catal.* **2001**, *201* (2), 258–269.
- (74) Han, W.; Nie, H.; Long, X.; Li, M.; Yang, Q.; Li, D. *Catal. Today* **2017**, *292*, 58–66.

3.6 Supporting Information

3.6.1 Elemental Analysis and Textual Properties of Parent Sulfides and Leached Sulfides

The metal loading of all parent materials were similar to the nominal compositions, with atomic Ni/(W+Ni) ratios ranging from 0 to 0.67 (Table 3.3). The X-ray diffractograms, as given in Figure 3.4A), show that besides the reflections of γ -Al₂O₃ at 2θ of 37.5°, 46°, and 67°, all W-containing sulfide catalysts exhibited reflections at 2θ of 33° and 59°, which correspond to WS₂ (JCPDS file No.8-237). Weak reflections of Ni₃S₂ (JCPDS file No.44-1418) were observed in Ni(11)WS₂/ γ -Al₂O₃ and Ni(8)WS₂/ γ -Al₂O₃ at 2θ of 30°, 51°, and 55°. The fraction of W atoms (denoted as “ f_w ”) at the edges of the sulfide slabs was calculated with assumption of perfect hexagonal geometry for the WS₂ slabs.^{1,2}

Table 3.3. Measured molar fraction of Ni, average slab length, stacking degree (obtained from TEM) and dispersion factor f_w of the WS₂ phase (standard deviation given in brackets), and hydrogenation rate of phenanthrene per gramm catalysts for the parent sulfide materials.

Catalyst	Ni/(W+Ni) mol/mol	Slab length, [nm]	Stacking	f_w	Reaction rate, mol _{Phe} h ⁻¹ g ⁻¹
WS ₂ / γ -Al ₂ O ₃	-	5.6 (2.1)	2.0 (1.1)	0.20	0.46
Ni(1.1)WS ₂ / γ -Al ₂ O ₃	0.14	4.5 (1.9)	1.9 (0.9)	0.22	2.95
Ni(3.2)WS ₂ / γ -Al ₂ O ₃	0.33	4.2 (1.8)	2.0 (1.0)	0.24	3.31
Ni(4.5)WS ₂ / γ -Al ₂ O ₃	0.41	4.1 (1.8)	1.9 (1.0)	0.24	3.22
Ni(11.1)WS ₂ / γ -Al ₂ O ₃	0.67	3.6 (1.5)	2.1 (1.1)	0.27	2.56

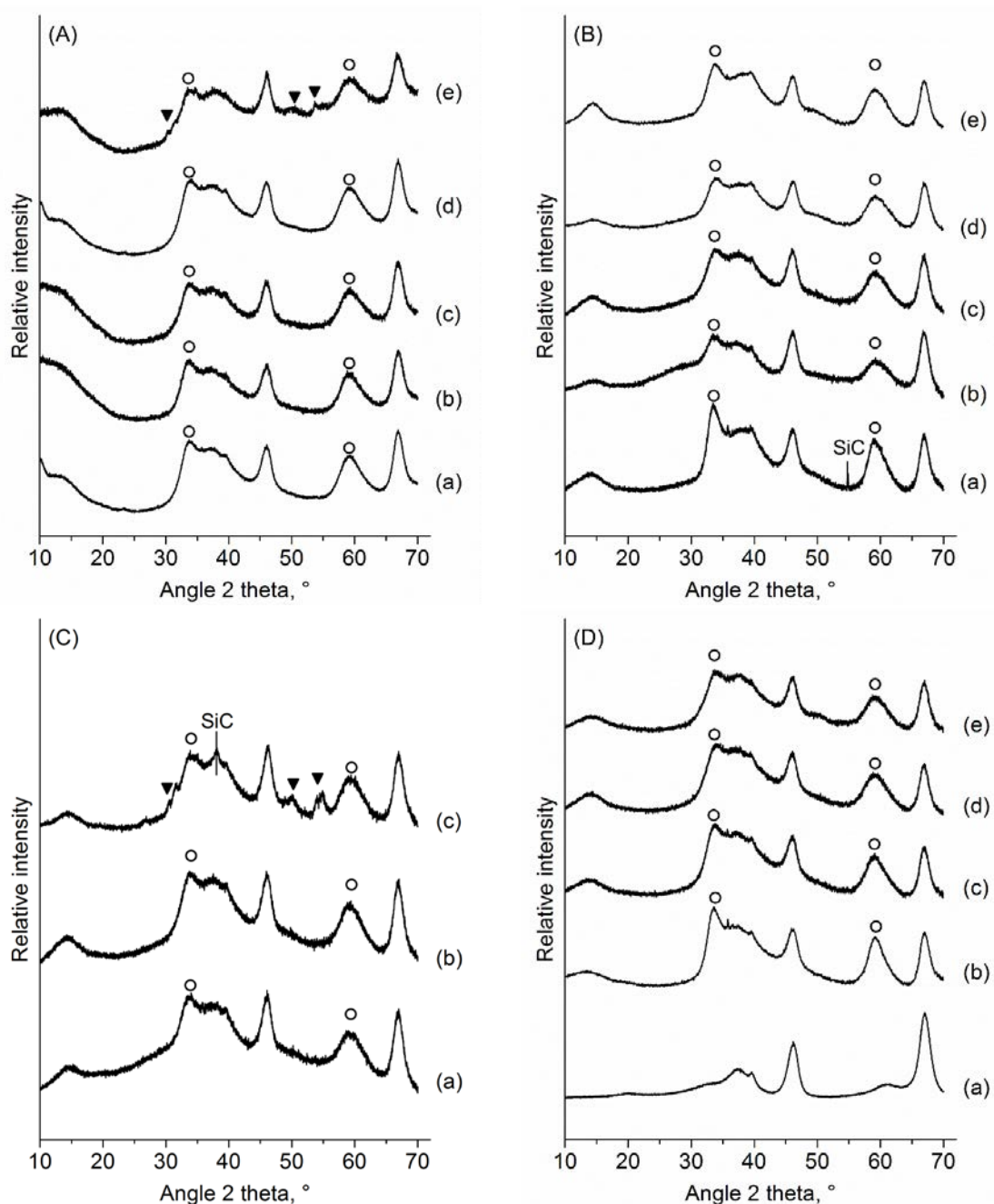
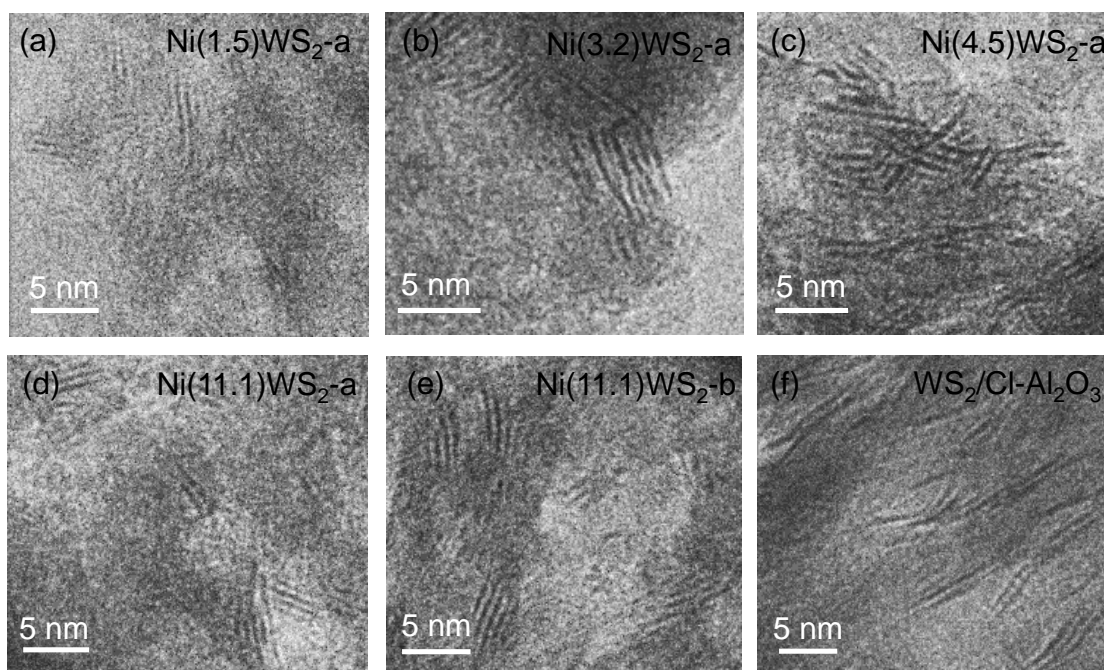


Figure 3.4. X-ray diffractograms of (A) parent sulfide catalysts WS₂/γ-Al₂O₃ (a), Ni(1.1)WS₂/γ-Al₂O₃ (b), Ni(3.2)WS₂/γ-Al₂O₃ (c), Ni(4.5)WS₂/γ-Al₂O₃ (d), Ni(11.1)WS₂/γ-Al₂O₃ (e); (B) leached sulfides WS₂/γ-Al₂O₃-a (a), Ni(1.1)WS₂/γ-Al₂O₃-a (b), Ni(3.2)WS₂/γ-Al₂O₃-a (c), Ni(4.5)WS₂/γ-Al₂O₃-a (d), Ni(11.1)WS₂/γ-Al₂O₃-a (e); (C) sulfides leached at pH=1 Ni(3.2)WS₂/γ-Al₂O₃-b (a), Ni(4.5)WS₂/γ-Al₂O₃-b (b), Ni(11.1)WS₂/γ-Al₂O₃-b (c); (D) Cl-Al₂O₃ support(a), and WS₂/Cl-Al₂O₃ (b), Ni(2.2)WS₂/Cl-Al₂O₃ (c), Ni(4.4)WS₂/Cl-Al₂O₃ (d), Ni(9.2)WS₂/Cl-Al₂O₃(e). Labeled reflections correspond to WS₂(○) and Ni₃S₂(▼), while non-labeled reflections correspond to Al₂O₃.

Table 3.4. Metal content, chloride content and atomic Ni/(W+Ni) ratio of the leached sulfide materials and oxide precursors supported on Cl-Al₂O₃.

Catalyst	Elemental content, mmol·g ⁻¹			Ni/(W+Ni) mol/mol
	W	Ni	Cl	
WS ₂ /γ-Al ₂ O ₃ -a	1.05	-	0.21	0
Ni(1.1)WS ₂ /γ-Al ₂ O ₃ -a	1.05	0.12	0.13	0.11
Ni(3.2)WS ₂ /γ-Al ₂ O ₃ -a	1.09	0.25	0.14	0.19
Ni(4.5)WS ₂ /γ-Al ₂ O ₃ -a	1.01	0.38	0.13	0.27
Ni(11.1)WS ₂ /γ-Al ₂ O ₃ -a	0.98	0.72	0.16	0.42
Ni(3.2)WS ₂ /γ-Al ₂ O ₃ -b	1.01	0.34	0.10	0.25
Ni(4.5)WS ₂ /γ-Al ₂ O ₃ -b	0.96	0.46	0.08	0.33
Ni(11.1)WS ₂ /γ-Al ₂ O ₃ -b	0.80	1.26	0.10	0.61
WS ₂ /Cl-Al ₂ O ₃	1.12	-	0.17	0
Ni(2.2)WS ₂ /Cl-Al ₂ O ₃	1.12	0.38	0.17	0.24
Ni(4.4)WS ₂ /Cl-Al ₂ O ₃	1.03	0.75	0.17	0.42
Ni(9.2)WS ₂ /Cl-Al ₂ O ₃	0.98	1.57	0.16	0.61

**Figure 3.5. Representative transmission electron micrographs of Ni(1.1)WS₂/γ-Al₂O₃-a (a), Ni(3.2)WS₂/γ-Al₂O₃-a (b), Ni(4.5)WS₂/γ-Al₂O₃-a (c), Ni(11.1)WS₂/γ-Al₂O₃-a (d), Ni(11.1)WS₂/γ-Al₂O₃-b (e), WS₂/Cl-Al₂O₃-a (f).**

3.6.2 CO Adsorption on Parent and Leached Sulfides

Five main bands at 2198, 2148, 2107, and 2068 cm⁻¹ are observed on parent WS₂/γ-Al₂O₃ catalyst (Figure. 3.6a), From previous studies,³⁻⁹ these bands can be attributed, respectively, to coordination of CO on Lewis acid sites (2197 cm⁻¹) and Brønsted acid sites (2150 cm⁻¹) of the support γ-Al₂O₃, and to CO adsorption onto the WS₂ edges. Additionally, the spectra of NiS_x/γ-Al₂O₃ (Figure 3.6b) exhibited an intense asymmetric band at 2079 cm⁻¹ with shoulders at 2056 and 2025 cm⁻¹. The main band (2084 cm⁻¹) is attributed to CO adsorbed on NiS_x, while the rest of band are attributed to polycarbonyl species (Ni(CO)_x).^{4,10-12} For simplification, six bands are used for deconvolution on parent Ni-promoted WS₂ materials: 2197, 2150-2160, 2107, 2066 and 2025 cm⁻¹, and the deconvoluted results are plotted in Figure 3.6.

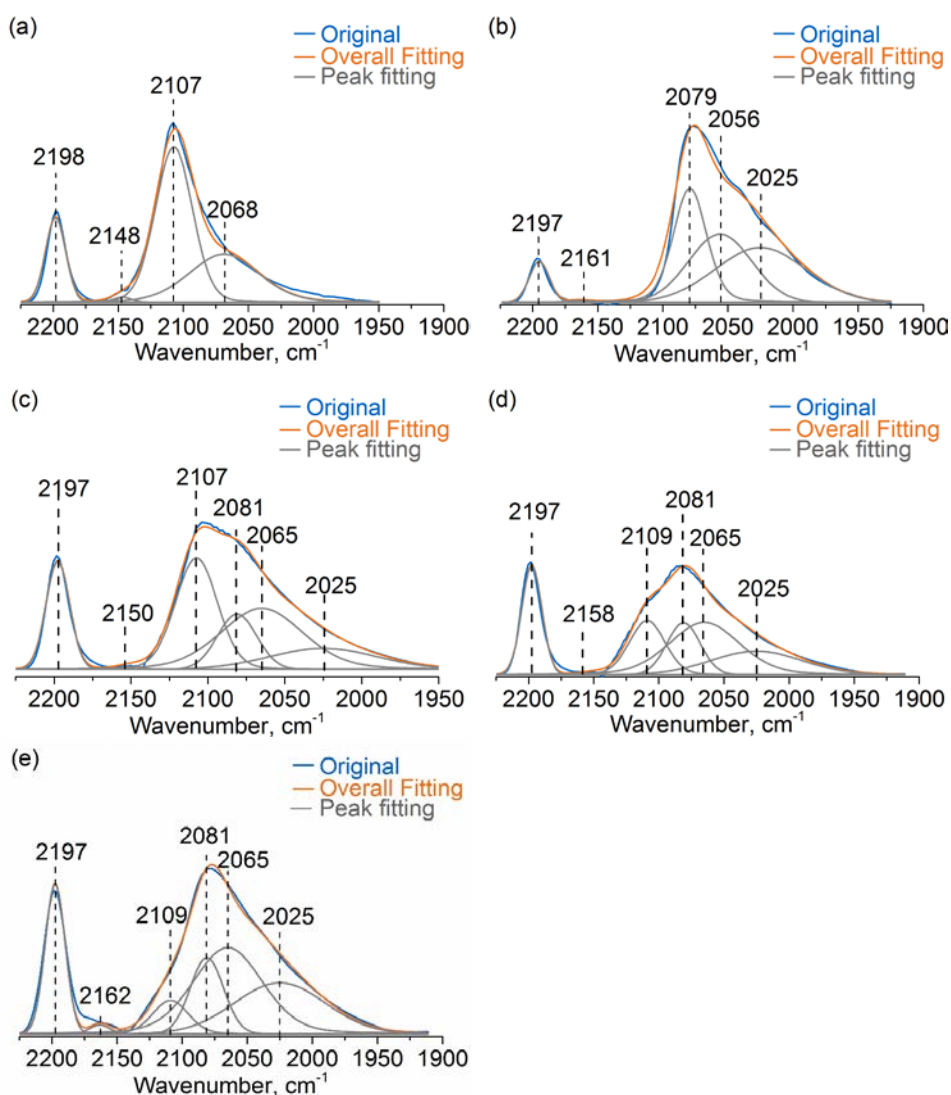


Figure 3.6. Deconvoluted infrared spectra of CO adsorbed at 123 K on parent sulfides WS₂/γ-Al₂O₃ (a), Ni(3)S_x/γ-Al₂O₃(b), Ni(3.2)WS₂/γ-Al₂O₃(c), Ni(4.5)WS₂/γ-Al₂O₃ (d), and Ni(11.1)WS₂/γ-Al₂O₃(e).

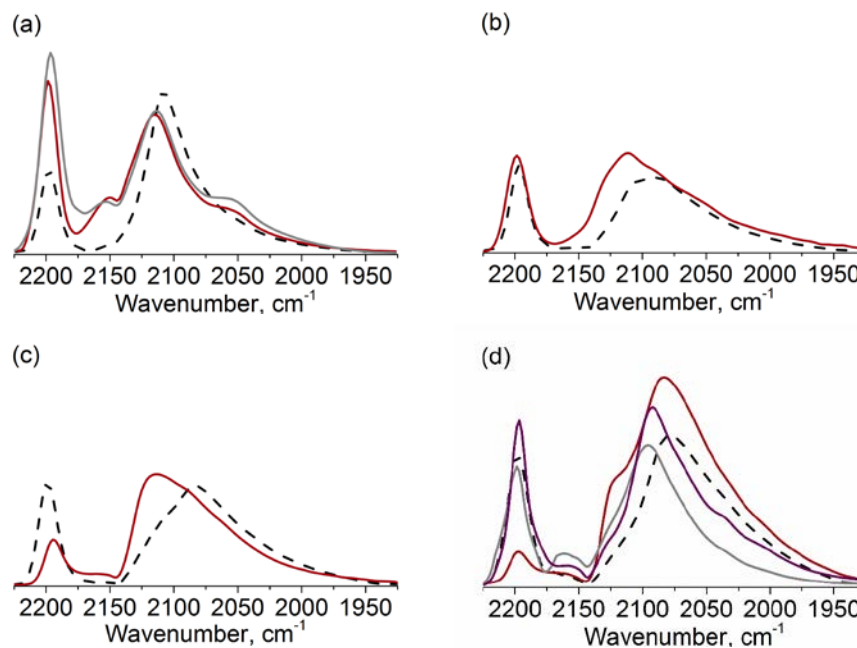


Figure 3.7. Comparison of IR spectra of CO adsorbed on WS₂/γ-Al₂O₃(black dashed), WS₂/γ-Al₂O₃-a(red) and WS₂/Cl-Al₂O₃(grey)(a), Ni(3.2)WS₂/γ-Al₂O₃(black dashed) and Ni(3.2)WS₂/γ-Al₂O₃-a(red) (b), Ni(4.5)WS₂/γ-Al₂O₃(black dashed) and Ni(4.5)WS₂/γ-Al₂O₃-a(red) (c), Ni(11.1)WS₂/γ-Al₂O₃(black dashed), Ni(11.1)WS₂/γ-Al₂O₃-a(red), Ni(11.1)WS₂/γ-Al₂O₃-b(purple) and Ni(9.2)WS₂/Cl-Al₂O₃(grey) (d). Adsorption experiments were conducted at 123 K with equilibrium pressure of 1 mbar CO.

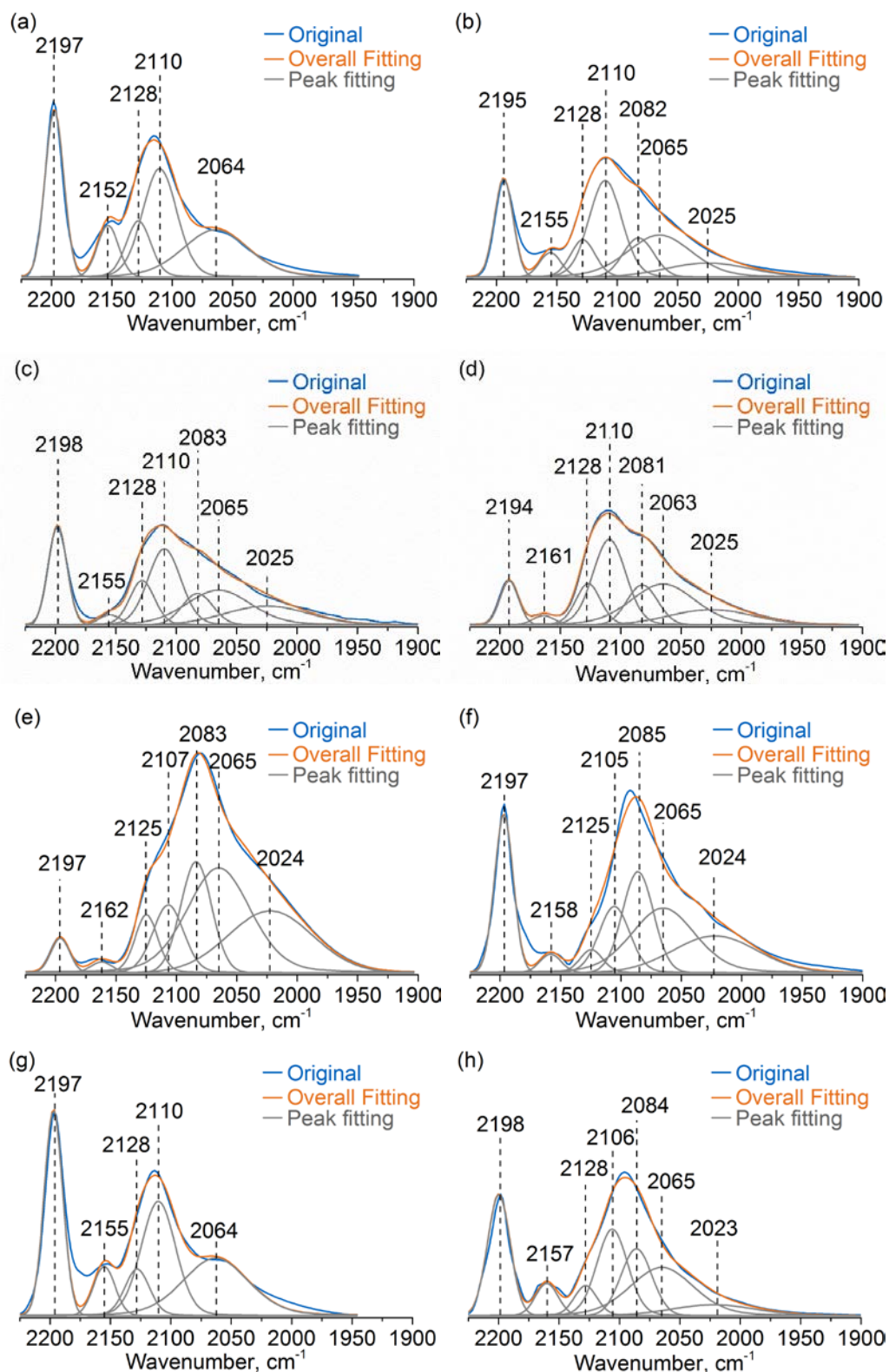


Figure 3.8. Deconvoluted IR spectra of CO adsorbed on WS₂/γ-Al₂O₃-a(a), Ni(1.1)WS₂/γ-Al₂O₃-a(b), Ni(3.2)WS₂/γ-Al₂O₃-a(c), Ni(4.5)WS₂/γ-Al₂O₃-a(d), Ni(11.1)WS₂/γ-Al₂O₃-a(e), Ni(11.1)WS₂/γ-Al₂O₃-b(f), WS₂/Cl-Al₂O₃ (g) and Ni(9.2)WS₂/Cl-Al₂O₃(h). Adsorption experiments were conducted at 123 K with equilibrium pressure of 1 mbar CO.

3.6.3 NO Adsorption on Leached WS₂ and Ni-promoted WS₂

The apparent molar extinction coefficient of NO adsorbed on non-promoted WS₂ sites is 3.9 cm·μmol⁻¹ for the band at ~1700 cm⁻¹ and for the NO bands at 1875 cm⁻¹ (promoted sites) the apparent molar extinction coefficient is 1 cm·μmol⁻¹.¹³

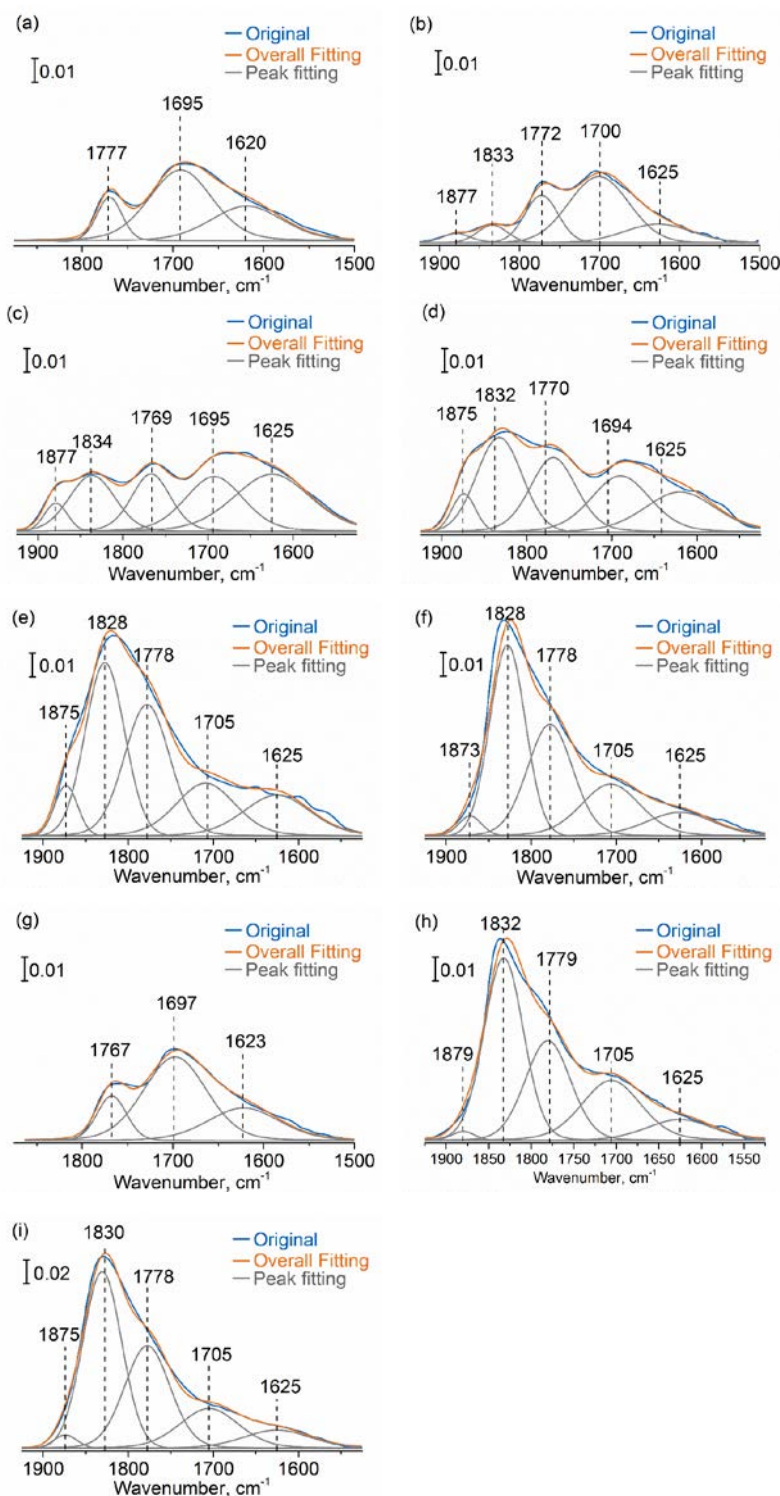


Figure 3.9. Deconvoluted IR spectra of NO adsorbed on WS₂/γ-Al₂O₃-a(a), Ni(1.1)WS₂/γ-Al₂O₃-a(b), Ni(3.2)WS₂/γ-Al₂O₃-a(c), Ni(4.5)WS₂/γ-Al₂O₃-a(d), Ni(11.1)WS₂/γ-Al₂O₃-a(e),

Ni(11.1)WS₂/γ-Al₂O₃-b(f), WS₂/Cl-Al₂O₃ (g), Ni(9.2)WS₂/Cl-Al₂O₃(h), and Ni(11.1)WS₂/γ-Al₂O₃-a' (treated twice in concentrated HCl) (i). Adsorption experiments were conducted at 303 K with equilibrium pressure of 1 mbar NO.

Table 3.5. Comparison of accessible Ni and W concentrations and fractions for the parent and leached Ni-WS₂/γ-Al₂O₃. The data for parent materials were taken from ref.¹³.

Catalyst	Atoms on the edge, μmol g ⁻¹	W atoms on the edge, μmol g ⁻¹	Ni atoms on the edge, μmol g ⁻¹	Ni/(Ni+W) on the edge, %
WS ₂ /γ-Al ₂ O ₃	238	238	0	0
Ni(1.1)WS ₂ /γ-Al ₂ O ₃	265	194	70	26
Ni(3.2)WS ₂ /γ-Al ₂ O ₃	242	170	72	30
Ni(4.5)WS ₂ /γ-Al ₂ O ₃	224	181	43	19
Ni(11.1)WS ₂ /γ-Al ₂ O ₃	192	178	14	7
WS ₂ /γ-Al ₂ O ₃ -a	229	229	0	0
Ni(1.1)WS ₂ /γ-Al ₂ O ₃ -a	280	217	63	23
Ni(3.2)WS ₂ /γ-Al ₂ O ₃ -a	315	176	139	44
Ni(4.5)WS ₂ /γ-Al ₂ O ₃ -a	375	183	192	51
Ni(11.1)WS ₂ /γ-Al ₂ O ₃ -a	422	173	249	59
Ni(11.1)WS ₂ /γ-Al ₂ O ₃ -b	274	169	105	38
Ni(9.2)WS ₂ /Cl-Al ₂ O ₃	242	194	48	20
Ni(11.1)WS ₂ /γ-Al ₂ O ₃ -a' (acid treated twice)	392	260	132	34

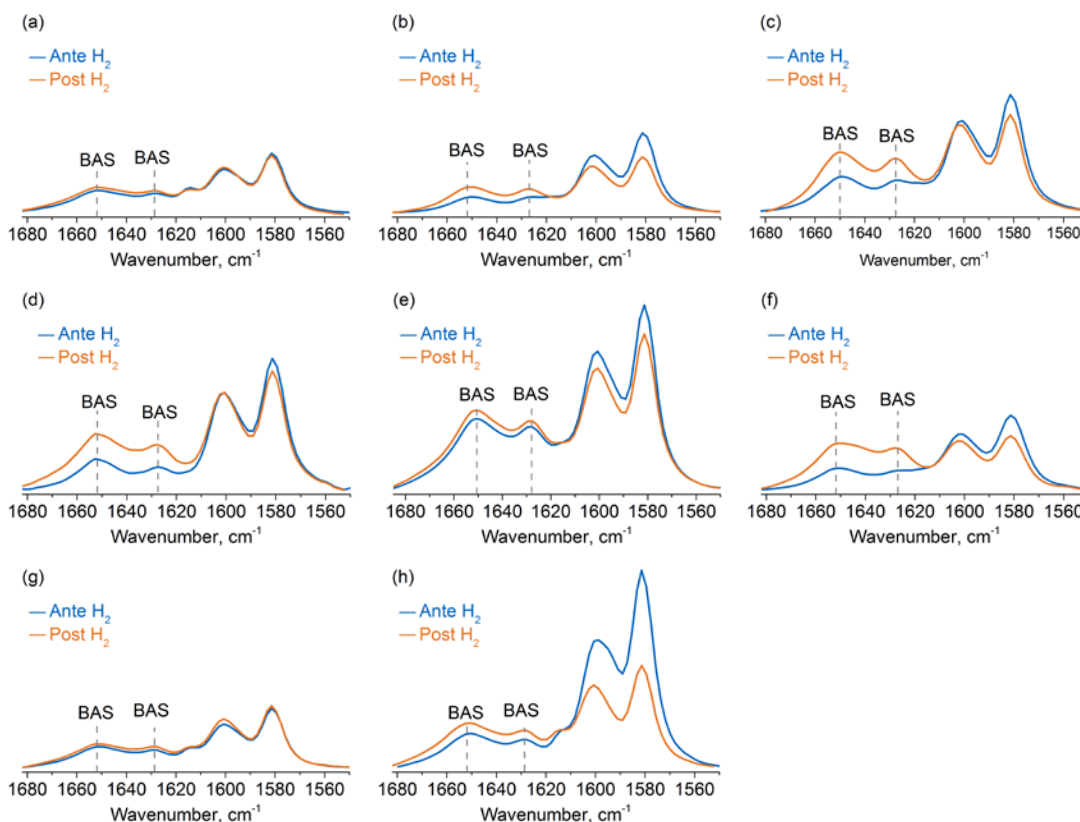
3.6.4 DMP-H₂ and Pyridine Adsorption Probed by IR Spectroscopy

Figure 3.10. IR spectra of adsorbed 2,6-dimethylpyridine (in the presence of 1 bar H₂) on WS₂/γ-Al₂O₃-a(a), Ni(1.1)WS₂/γ-Al₂O₃-a(b), Ni(3.2)WS₂/γ-Al₂O₃-a(c), Ni(4.5)WS₂/γ-Al₂O₃-a(d), Ni(11.1)WS₂/γ-Al₂O₃-a(e), Ni(11.1)WS₂/γ-Al₂O₃-b(f), WS₂/Cl-Al₂O₃ (g) and Ni(9.2)WS₂/Cl-Al₂O₃(h). Adsorption bands at 1650 cm⁻¹ and 1627 cm⁻¹ are assigned to vibration bands ν_{8a} and ν_{8b} from protonated 2,6-dimethylpyridine; The bands at ~1615 and 1580 cm⁻¹ result from 2,6-dimethylpyridine coordinated to Lewis acid sites; and bands at 1602 and 1580 cm⁻¹ correspond to weakly adsorbed 2,6-dimethylpyridine.^{14,15}

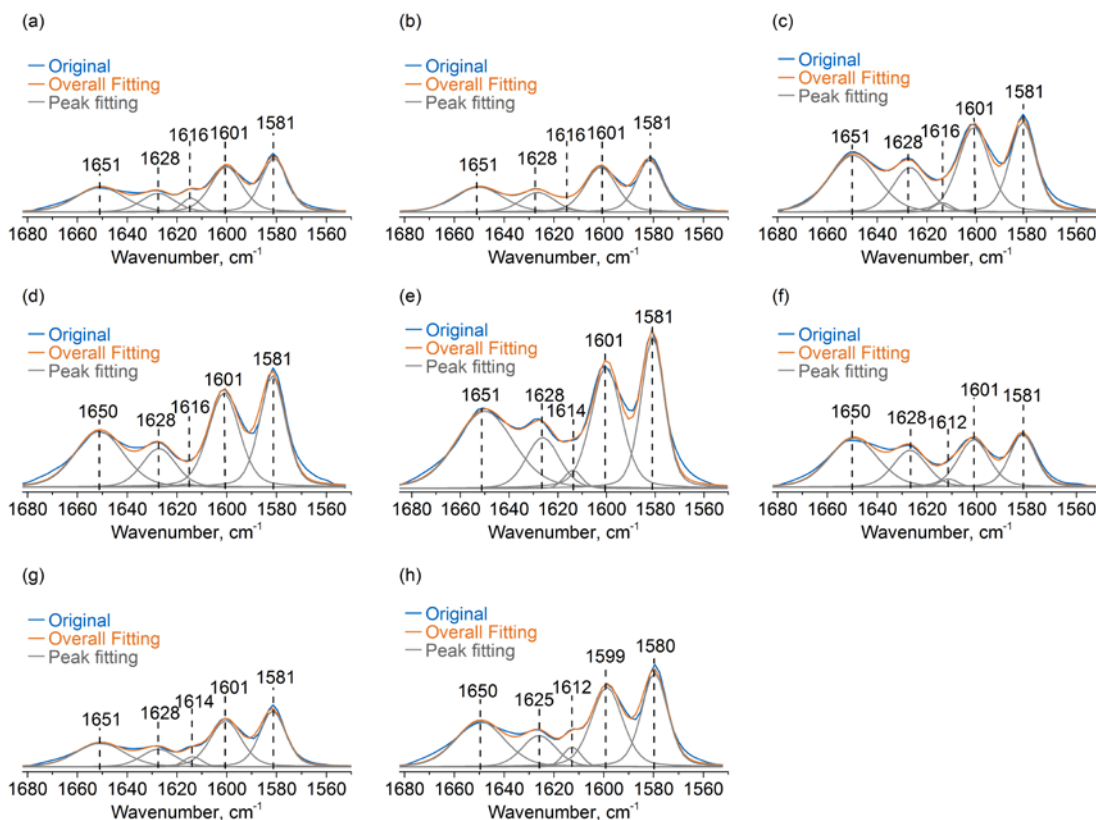


Figure 3.11. IR spectra of adsorbed 2,6-dimethylpyridine (in the presence of 1 bar H₂) on WS₂/γ-Al₂O₃-a(a), Ni(1.1)WS₂/γ-Al₂O₃-a(b), Ni(3.2)WS₂/γ-Al₂O₃-a(c), Ni(4.5)WS₂/γ-Al₂O₃-a(d), Ni(11.1)WS₂/γ-Al₂O₃-a(e), Ni(11.1)WS₂/γ-Al₂O₃-b(f), WS₂/Cl-Al₂O₃ (g) and Ni(9.2)WS₂/Cl-Al₂O₃(h). Peaks at 1650 cm⁻¹ and 1627 cm⁻¹ are assigned to vibration bands ν_{8a} and ν_{8b} from protonated 2,6-dimethylpyridine; The bands at ~1615 and 1580 cm⁻¹ result from 2,6-dimethylpyridine coordinated to Lewis acid sites; and bands at 1602 and 1580 cm⁻¹ correspond to weakly adsorbed 2,6-dimethylpyridine.^{14,15}

The specific activity as well as the S-H concentration on Ni-decorated WS₂ edge sites has been calculated by subtracting the contribution of non-promoted WS₂ edge sites. For example, on Ni(11.1)WS₂/γ-Al₂O₃-a with overall S-H concentration of 354 μmol g⁻¹ and a Ni/(Ni+W) molar ratio on the edge of 59%, the contribution of non-promoted W to S-H concentration is calculated as 89 μmol g⁻¹ (S-H concentration on WS₂/γ-Al₂O₃-a) times the W/(Ni+W) molar ratio of 0.41, which equals to 36 μmol g⁻¹. The contribution from Ni then can be obtained by subtracting 36 μmol g⁻¹ from 354 μmol g⁻¹, as shown in Table 3.6, 318 μmol g⁻¹. Similar corrections have been applied for calculating the specific activity related to Ni-substituted WS₂ sites.

Table 3.6. Concentration of S-H and the concentration of pyridine adsorbed on strong Lewis acid sites (LAS) over parent materials.

Catalyst	S-H, $\mu\text{mol}\cdot\text{g}^{-1}$	Strong LAS, $\mu\text{mol}\cdot\text{g}^{-1}$
WS ₂ / γ -Al ₂ O ₃	82	71
Ni(1.1)WS ₂ / γ -Al ₂ O ₃	114	-
Ni(3.2)WS ₂ / γ -Al ₂ O ₃	150	106
Ni(4.5)WS ₂ / γ -Al ₂ O ₃	136	97
Ni(11)WS ₂ / γ -Al ₂ O ₃	93	63
γ -Al ₂ O ₃ ¹⁶	22	33

Table 3.7. Hydrogenation rate of PHE and the concentration of S-H groups on Ni sites decorated on the edge.

Catalyst	Ni/(Ni+W) on the edge, %	S-H conc. on Ni sites, $\mu\text{mol g}^{-1}$	Reaction rate on Ni sites, $\text{mol}_{\text{Phe}} \text{h}^{-1} \text{g}^{-1}$
Ni(1.1)WS ₂ / γ -Al ₂ O ₃ -a	23	53	2.6
Ni(3.2)WS ₂ / γ -Al ₂ O ₃ -a	44	151	5.1
Ni(4.5)WS ₂ / γ -Al ₂ O ₃ -a	51	234	9.0
Ni(11.1)WS ₂ / γ -Al ₂ O ₃ -a	59	318	13.1
Ni(11.1)WS ₂ / γ -Al ₂ O ₃ -b	38	154	5.1
Ni(9.2)WS ₂ /Cl-Al ₂ O ₃	20	112	4.1
Ni(11.1)WS ₂ / γ -Al ₂ O ₃ - a' (acid treated twice)	34	219	7.5

Table 3.8. Increment of concentration of S-H on Cl-containing samples compared to parent materials.

Catalyst	S-H conc., $\mu\text{mol g}^{-1}$	Difference compared to parent materials, $\mu\text{mol g}^{-1}$	Increment of S-H conc., %
WS ₂ / γ -Al ₂ O ₃ -a	89	7	9
Ni(1.1)WS ₂ / γ -Al ₂ O ₃ -a	119	5	4
Ni(3.2)WS ₂ / γ -Al ₂ O ₃ -a	201	51	34
Ni(4.5)WS ₂ / γ -Al ₂ O ₃ -a	278	142	104
Ni(11.1)WS ₂ / γ -Al ₂ O ₃ -a	354	261	287
Ni(11.1)WS ₂ / γ -Al ₂ O ₃ -b	210	117	126
WS ₂ /Cl-Al ₂ O ₃	90	8	10
Ni(9.2)WS ₂ /Cl-Al ₂ O ₃	183	90	97

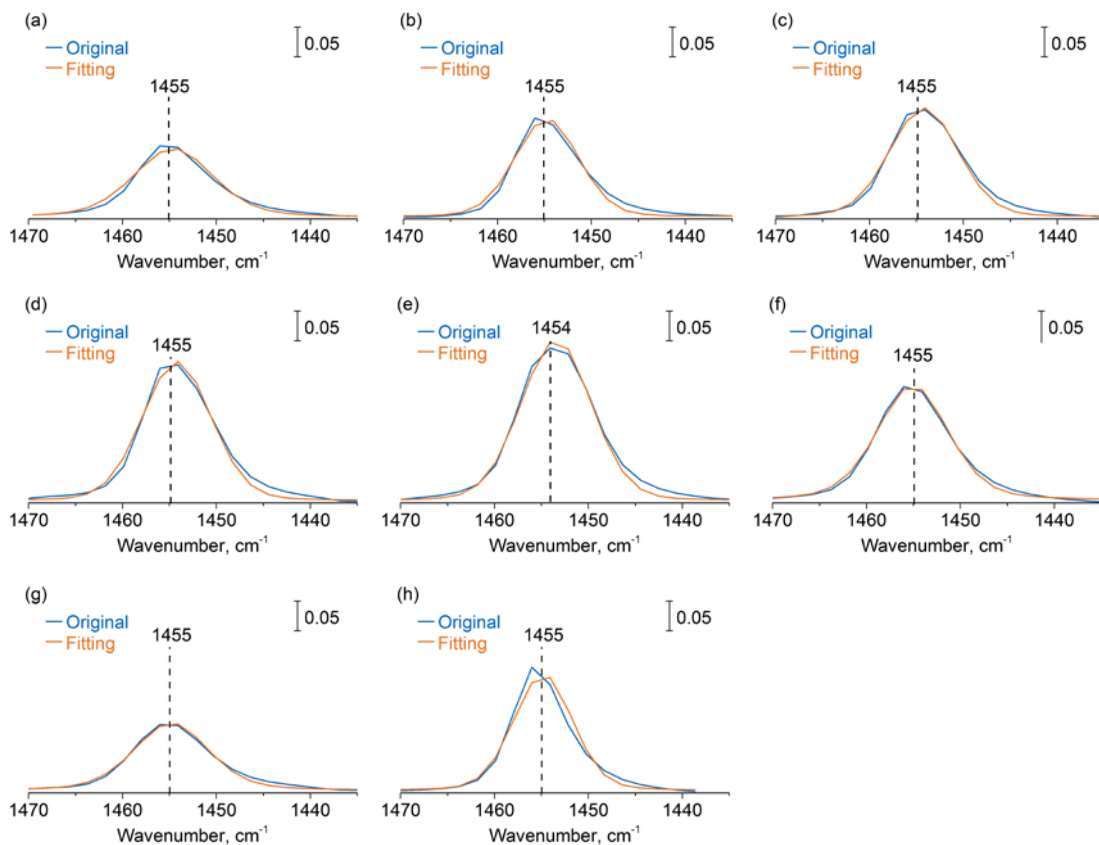


Figure 3.12. Deconvoluted spectra of adsorbed pyridine monitored by IR spectroscopy on WS₂/ γ -Al₂O₃-a(a), Ni(1.1)WS₂/ γ -Al₂O₃-a(b), Ni(3.2)WS₂/ γ -Al₂O₃-a(c), Ni(4.5)WS₂/ γ -Al₂O₃-a(d), Ni(11.1)WS₂/ γ -Al₂O₃-a(e), Ni(11.1)WS₂/ γ -Al₂O₃-b(f), WS₂/Cl-Al₂O₃ (g) and Ni(9.2)WS₂/Cl-Al₂O₃(h).

3.6.5 Hydrogenation of Phenanthrene

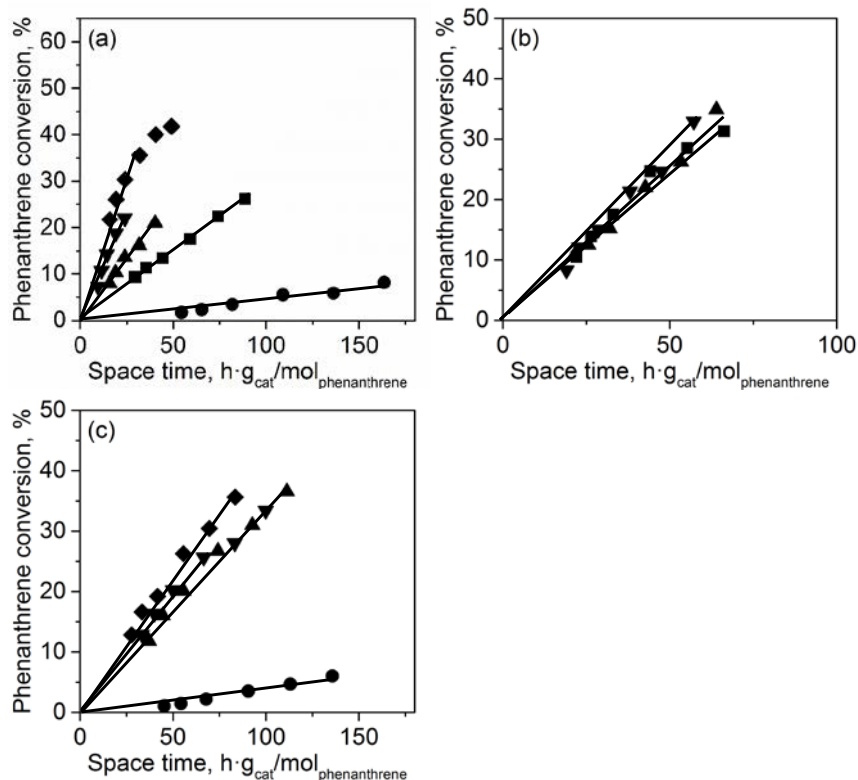
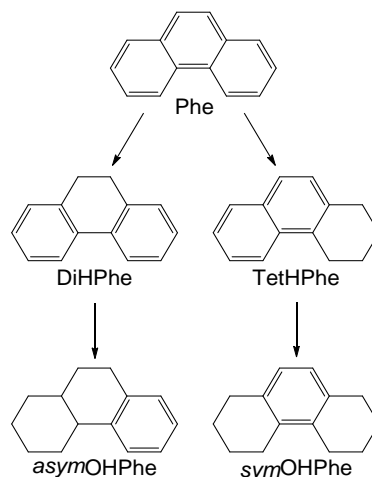


Figure 3.13. Conversion of PHE as function of space time over catalysts (a) leached sulfides WS₂/γ-Al₂O₃-a (●), Ni(1)WS₂/γ-Al₂O₃-a (■), Ni(3)WS₂/γ-Al₂O₃-a (▲), Ni(5)WS₂/γ-Al₂O₃-a (▼), Ni(11)WS₂/γ-Al₂O₃-a (◆); (b) sulfides leached at pH=1 Ni(3)WS₂/γ-Al₂O₃-b (■), Ni(5)WS₂/γ-Al₂O₃-b (▲), Ni(11)WS₂/γ-Al₂O₃-b (▼); (c) WS₂/Cl-Al₂O₃ (●), Ni(2)WS₂/Cl-Al₂O₃ (▲), Ni(5)WS₂/Cl-Al₂O₃ (▼), Ni(11)WS₂/Cl-Al₂O₃ (◆).

Table 3.9. Overall rate of phenanthrene conversion (r_{Phe}), and rates of reaction with initial hydrogenation at the middle and at a lateral ring (r_1 and r_2 , respectively). All rates are given in mol·h⁻¹·g_{cat}⁻¹. The compounds involved in the reaction network are: phenanthrene (Phe), 9,10-dihydro-phenanthrene (DiHPhe), 1,2,3,4-tetrahydrophenanthrene (TetHPhe), 1,2,3,4,5,6,7,8-octahydrophenanthrene (symOHPhe), and 1,2,3,4,4a,9,10,10a-octahydrophenanthrene (asymOHPhe).

Catalyst	$r_{\text{Phe}} \times 10^3$	$r_1 \times 10^3$	$r_2 \times 10^3$	r_1/r_2
WS ₂ /γ-Al ₂ O ₃ -a	0.45	0.36	0.09	4.0
Ni(1.1)WS ₂ /γ-Al ₂ O ₃ -a	3.0	1.5	1.5	1.0
Ni(3.2)WS ₂ /γ-Al ₂ O ₃ -a	5.4	2.3	3.1	0.7
Ni(4.5)WS ₂ /γ-Al ₂ O ₃ -a	9.2	3.6	5.6	0.6
Ni(11.1)WS ₂ /γ-Al ₂ O ₃ -a	13.3	5.1	8.2	0.6
Ni(10)S ₂ /γ-Al ₂ O ₃ -a	0	0	0	-
Ni(3.2)WS ₂ /γ-Al ₂ O ₃ -b	5.0	2.0	3.0	0.6
Ni(4.5)WS ₂ /γ-Al ₂ O ₃ -b	5.0	2.0	3.0	0.6
Ni(11.1)WS ₂ /γ-Al ₂ O ₃ -b	5.4	2.2	3.2	0.6
WS ₂ /Cl-Al ₂ O ₃	0.45	3.5	0.5	7.0
Ni(2.2)WS ₂ /Cl-Al ₂ O ₃	3.4	1.7	1.7	1.0
Ni(4.4)WS ₂ /Cl-Al ₂ O ₃	3.5	1.6	1.9	0.9
Ni(9.2)WS ₂ /Cl-Al ₂ O ₃	4.5	2.2	2.3	1.0
γ-Al ₂ O ₃ -Cl	0	0	0	-



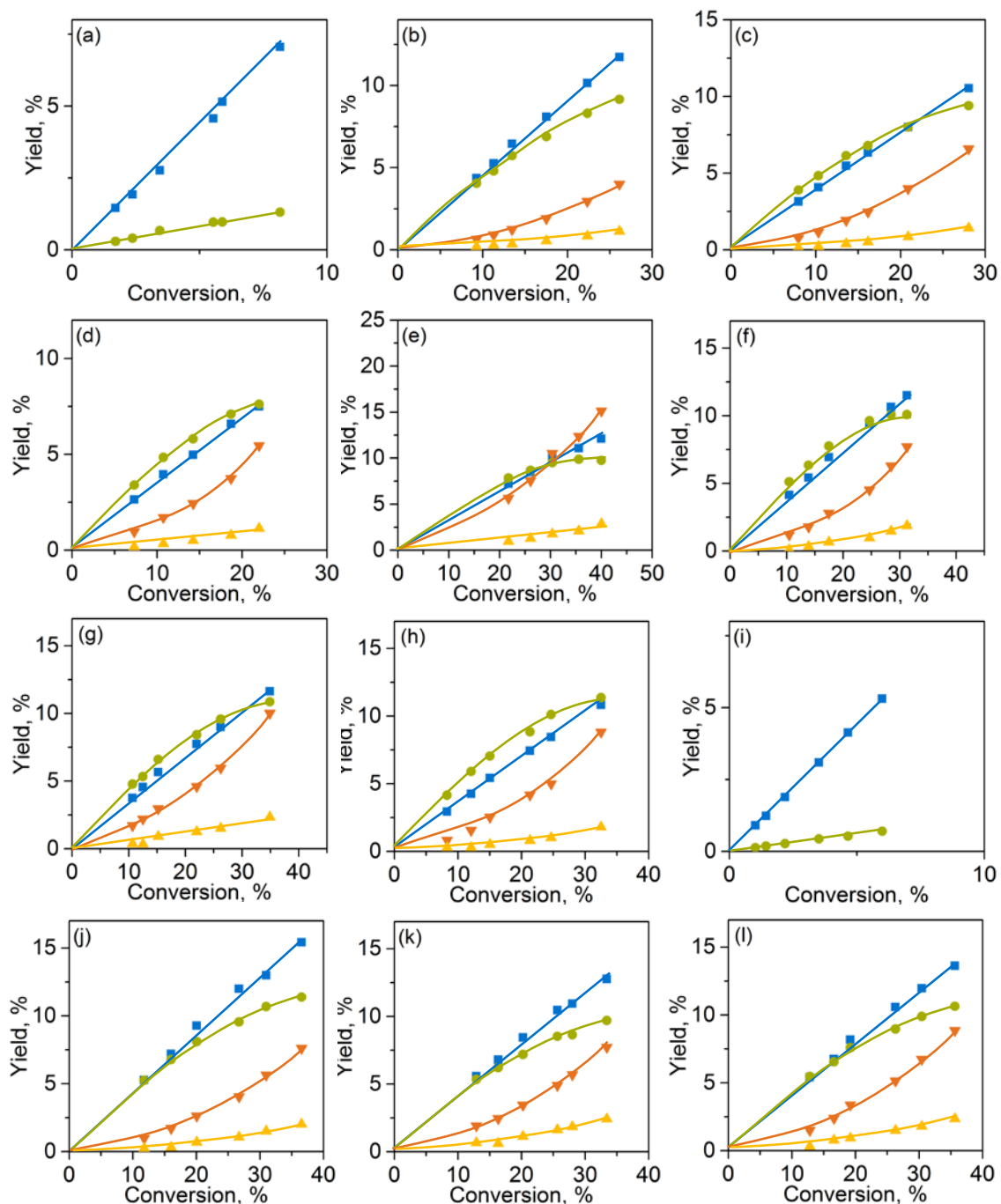


Figure 3.14. Yield of DiHPhe(■), TetHPhe(●), symOHPhe(▼), asymOHPhe(▲) from hydrogenation of PHE over catalysts WS₂/γ-Al₂O₃ (a), Ni(1)WS₂/γ-Al₂O₃ (b), Ni(3)WS₂/γ-Al₂O₃ (c), Ni(5)WS₂/γ-Al₂O₃ (d), Ni(11)WS₂/γ-Al₂O₃ (e), Ni(3)WS₂/γ-Al₂O₃-b (f), Ni(5)WS₂/γ-Al₂O₃-b (g), Ni(11)WS₂/γ-Al₂O₃-b (h), WS₂/Cl-Al₂O₃ (i), Ni(2)WS₂/Cl-Al₂O₃ (j), Ni(5)WS₂/Cl-Al₂O₃ (k), and Ni(11)WS₂/Cl-Al₂O₃ (l).

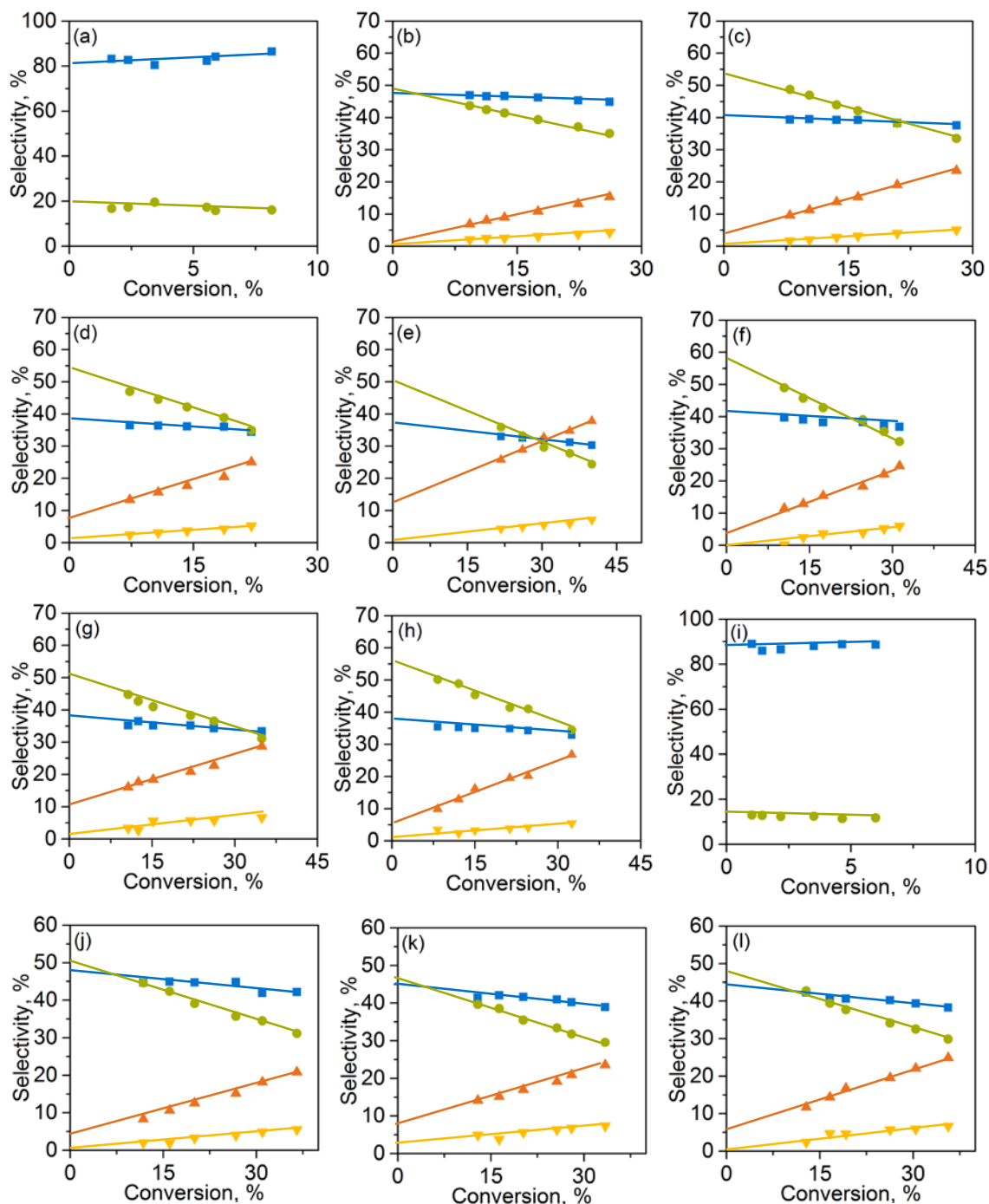


Figure 3.15. Selectivity-conversion plots of hydrogenation of PHE on WS₂/γ-Al₂O₃ (a), Ni(1)WS₂/γ-Al₂O₃ (b), Ni(3)WS₂/γ-Al₂O₃ (c), Ni(5)WS₂/γ-Al₂O₃ (d), Ni(11)WS₂/γ-Al₂O₃ (e), Ni(3)WS₂/γ-Al₂O₃-b (f), Ni(5)WS₂/γ-Al₂O₃-b (g), Ni(11)WS₂/γ-Al₂O₃-b (h), WS₂/Cl-Al₂O₃ (i), Ni(2)WS₂/Cl-Al₂O₃ (j), Ni(5)WS₂/Cl-Al₂O₃ (k), Ni(11)WS₂/Cl-Al₂O₃(l). The hydrogenation products are marked as DiHPhe(■), TetHPhe(●), symOHPhe(▲), asymOHPhe(▼).

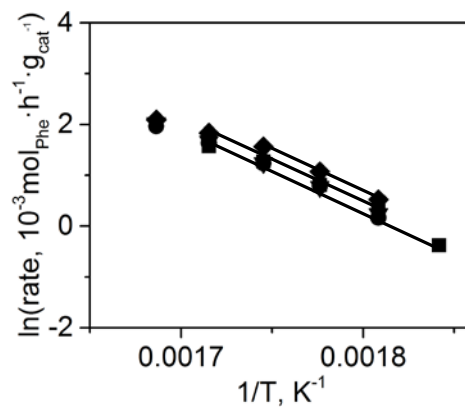


Figure 3.16. Arrhenius plots of hydrogenation of PHE over Ni(2.2)WS₂/γ-Al₂O₃ (■), Ni(2.2)WS₂/Ci-Al₂O₃ (◆), Ni(4.4)WS₂/Ci-Al₂O₃ (●), and Ni(9.2)WS₂/Ci-Al₂O₃ (▼). Hydrogenation rates were determined at temperatures from 543 to 583 K at a H₂ to hydrocarbon volumetric ratio of 300.

3.7 References for Supporting Information

- (1) Hensen, E. J. M.; Kooyman, P. J.; van der Meer, Y.; van der Kraan, a. M.; de Beer, V. H. J.; van Veen, J. a. R.; van Santen, R. a. *J. Catal.* **2001**, *199* (2), 224–235.
- (2) Kasztelan, S.; Toulhoat, H.; Grimblot, J.; Bonnelle, J. *Appl. Catal.* **1984**, *13*, 372–376.
- (3) Zuo, D.; Vrinat, M.; Nie, H.; Maugé, F.; Shi, Y.; Lacroix, M.; Li, D. *Catal. today* **2004**, *93*, 751–760.
- (4) Duchet, J.-C.; Lavalley, J.-C.; Housni, S.; Ouafi, D.; Bachelier, J.; Lakhdar, M.; Mennour, A.; Cornet, D. *Catal. Today* **1988**, *4* (1), 71–96.
- (5) Müller, B.; van Langeveld, a D.; Moulijn, J. a; Knözinger, H. *J. Phys. Chem.* **1993**, *97*, 9028–9033.
- (6) Maugé, F.; Lavalley, J. C. *J. Catal.* **1992**, *137* (1), 69–76.
- (7) Mueller, B.; van Langeveld, A. D.; Moulijn, J. A.; Knoezinger, H. *J. Phys. Chem.* **1993**, *97* (35), 9028–9033.
- (8) Ouafi, D.; Mauge, F.; Lavalley, J. C. *Bull. Soc. Chim. Fr.* **1989**, No. 3, 363–369.
- (9) Travert, A.; Dujardin, C.; Maugé, F.; Cristol, S.; Paul, J. F.; Payen, E.; Bougeard, D. *Catal. Today* **2001**, *70* (1–3), 255–269.
- (10) Travert, a.; Dujardin, C.; Maugé, F.; Veilly, E.; Cristol, S.; Paul, J. F.; Payen, E. *J. Phys. Chem. B* **2006**, *110* (3), 1261–1270.
- (11) Marceau, E.; Löfberg, A.; Giraudon, J.-M.; Négrier, F.; Che, M.; Leclercq, L. *Appl. Catal. A Gen.* **2009**, *362* (1–2), 34–39.
- (12) Poncelet, G.; Centeno, M. A.; Molina, R. *Appl. Catal. A Gen.* **2005**, *288* (1–2), 232–242.
- (13) Luo, W.; Shi, H.; Willnecker, E.; Gutiérrez, O. Y.; Lercher, J. *Angew. Chemie Int. Ed.* **2018**, *0* (ja).
- (14) Travert, A.; Maugé, F. *Stud. Surf. Sci. Catal.* **1999**, *127*, 269–277.
- (15) Oliviero, L.; Vimont, A.; Lavalley, J.-C.; Sarria, F. R.; Gaillard, M.; Maugé, F.

Phys. Chem. Chem. Phys. **2005**, 7 (8), 1861–1869.

(16) Schachtl, E.; Kondratieva, E.; Gutiérrez, O. Y.; Lercher, J. A. *J. Phys. Chem. Lett.* **2015**, 6 (15), 2929–2932.

(17) Schachtl, E.; Zhong, L.; Kondratieva, E.; Hein, J.; Gutiérrez, O. Y.; Jentys, A.; Lercher, J. A. *ChemCatChem* **2015**, 7 (24), 4118–4130.

3.8 Associated Content

Contributions: Dr. Hui Shi supervised this work. Dr. Eva Schachtl contributed with the design of the infrared spectrometer. Manuel Wagenhofer and Wanqiu Luo contributed with design of the experiments. Wanqiu Luo contributed with the design of the reactors, preparation of the samples, operation of setups, data analysis, and preparation of the draft. Prof. Dr. Johannes A. Lercher was responsible for data discussion, supervising and manuscript preparation. Dr. Hui Shi and Prof. Dr. Johannes A. Lercher are the principal investigators of this work.

Acknowledgement: This work was supported by the Chevron Energy Technology Company. The authors would like to specially thank Alexander Kuperman, Axel Brait, and Jinyi Han for fruitful discussions, and Prof. Roel Prins for the critical review of the results. We are also grateful to Dr. Marianne Hanzlik for TEM measurements, and Dipl.-Ing. Xaver Hecht for technical support.

Chapter 4

Summary and Conclusions

Heavy crude oil is becoming the dominating energy source for the next few decades, and hydrotreating is one of the most important industrial processes to convert heavy crude into commercial fuels. Meanwhile, the removal of S, N, O and aromatics from heavy crude is attracting more attention owing to the tightened legislation regarding the environmental impacts. Ni promoted MoS₂ and WS₂ catalysts provide promising hydrogenation activity in hydrotreating process, and therefore have been studied in detail for decades. Several reports attributed higher hydrogenation activity to Ni-WS₂ than to Ni-MoS₂, without elucidating the structure-activity relation in atomic scale. Besides, the formation of NiS_x crystals, which occurs at high Ni loading, has always hindered researchers to reveal the intrinsic activity of each Ni promoting site on MoS₂ and WS₂ catalysts. Hence, the aim of this thesis is to rationalize the origin of the outstanding hydrogenation activity of Ni-WS₂, and to study the intrinsic activity of Ni promoting sites without the hindrance from NiS_x crystallites.

The structure of Ni-WS₂ supported on γ -Al₂O₃ was investigated in Chapter 2. A series of γ -Al₂O₃-supported WO₃ precursors with varying concentrations of Ni (0-0.67 in Ni/Me molar ratio) were prepared and thoroughly characterized. Increasing concentrations of Ni²⁺ cations coordinating oligomeric octahedral tungstate species (probed by Raman, UV-vis spectroscopy and NO-IR) was observed in the oxide precursors containing Ni. The concentration of Ni-O-W species, however, reached a maximum at a Ni/Me molar ratio of 0.25. The incorporation of Ni to tungstates weakened the W-O bonds, easing O-S exchange and the reduction of W⁶⁺ to W⁴⁺ during sulfidation, which yielded an increasing dispersion (decreasing slab length) with increasing Ni content on the resulting Ni-WS₂.

Structural models of Ni-WS₂ were obtained on the basis of TEM results and the infrared spectra of NO adsorption. Upon Ni addition, the substitution degree of Ni at the WS₂ edges increased up to ca. 32 % (i.e., a third of edge atoms are Ni) at the bulk Ni/Me molar ratio of 0.25 (TEM and NO-IR), which coincided with the results obtained on Ni-MoS₂. Further Ni addition yielded NiS_x particles near the Ni-WS₂ edge, thus lowering the concentration of accessible Ni-W-S sites. In the low Ni loading range (i.e., Ni/Me molar ratios below 0.25) the concentration of Ni-W-S sites increased at the expense of not promoted WS₂ sites with increasing Ni content.

All the sulfide catalysts were tested for the hydrogenation of phenanthrene (PHE) in the absence of defunctionalization pathways. PHE was chosen as the model compound because it is representative for polycyclic aromatic hydrocarbons (PAH) with special electronic structure. The reaction network of PHE hydrogenation is composed of two parallel pathways, i.e., initial hydrogenation at the middle ring (PHE → DiHPHE → asymOHPHE) and initial hydrogenation at a lateral ring (PHE → TetHPhe → symOHPhe). In the range of Ni/(W+Ni) molar ratio below 0.25, the reaction rates of the two pathways increased with increasing Ni decoration until the maximum decoration degree, while the selectivity gradually shifted from the initial hydrogenation at the middle ring to the case that two pathways contributing equally. Beyond the optimum Ni decoration, the blocking of Ni-W-S sites caused a linear reduction of rates for the two pathways, while the selectivity remained equivalent. However, the same phenomena were demonstrated before for the same reaction catalyzed by Ni-MoS₂/γ-Al₂O₃.

The functional groups for hydrogenation, i.e. sulfhydryl groups (SH), at the active edges of Ni-WS₂ and Ni-MoS₂ were then characterized by infrared spectroscopy with an adsorption of a base, 2,6-dimethylpyridine, together with H₂S or H₂. The results showed that the SH groups vicinal to edge-decorated Ni are much more reactive than SH associated with non-promoted sites, on both MoS₂ and WS₂. This Ni promotion effect leads to higher hydrogen addition rates as well as an enhancement of the lateral rings hydrogenation in PHE. A linear correlation was obtained between the concentrations of SH groups on Ni-promoting sites and the activities for hydrogenation of PHE, i.e., the intrinsic activity per SH group in the vicinity of Ni-promoting sites was the same, regardless of the slab composition (MoS₂, WS₂ or mixed MoWS₂). The higher activity of Ni-WS₂ can be primarily explained by its higher concentration of SH groups than on Ni-MoS₂. Further, adsorption experiments with pyridine were conducted on infrared spectroscopy, in order to determine the concentration of strong Lewis acid sites (LAS). Ni-WS₂ inherently has higher concentration of strong LAS than Ni-MoS₂, which in turn pinpoints a higher tendency of the Ni-W-S phase to stabilize more SH groups at the edge.

This work rationalized the difference in hydrogenation activity between Ni-promoted WS₂ and MoS₂, and further enabled a more rigorous comparison of intrinsic activities among different supported transition metal sulfides.

A post-synthetic acid treatment with hydrochloric acid, i.e., named as “leaching”, was employed to Ni-WS₂/γ-Al₂O₃ to remove NiS_x particles on the active edge of Ni-WS₂ (Chapter 3). After leaching (at pH = -1 and 1), Ni concentration was 33-62% lower than in parent Ni-WS₂/γ-Al₂O₃, without appreciable losses of W, which indicates a selective removal of Ni by HCl at room temperature. This cleaned up the surface of the catalysts and maximized the concentration of exposed metal edges, for both WS₂ sites and Ni decorated sites. As a result, a higher decoration degree of Ni was obtained up to 59% at the highest Ni bulk loading, which exceeds the postulated optimum in the well-accepted “NiMoS” model. Besides, the surface roughening of WS₂, possibly caused by concentrated acid treatment, also contributed to the overall increase in the concentration of total metal atoms. This further benefits the concentration of S-H groups on the leached catalyst with up to 287% increment. The contribution of NiS_x removal was estimated to be 70%-80% to the overall rate enhancement for hydrogenation of phenanthrene.

Residue Cl brought by hydrochloric acid treatment has also positive impacts for the enhancement of the catalyst activity. It enhances the strength of acid sites on γ-Al₂O₃ and further leads to an electron deficiency on the WS₂ phase. It increases the concentration of S-H groups and activity by 20~30%, without noticeable changes in the selectivity or the apparent activation energy for hydrogenation of PHE. Therefore, in this leaching procedure, the effect of removing NiS_x took precedence over the electronic effect of Cl residues, contributing to the outstanding hydrogenation activity on the leached Ni-WS₂/γ-Al₂O₃.

Leaching treatment allows us to better understand the promotional effect of Ni on WS₂/γ-Al₂O₃. This work proved that the decoration degree of Ni on WS₂ edges can exceed the well-known maxima 33%, which had been often obscured by the formation of NiS_x on the edges reducing the accessibility of active sites.

List of Publications

Journal Articles

Luo, Wanqiu, Hui Shi, Eva Schachtl, Oliver Y. Gutiérrez, and Johannes A. Lercher. "Active Sites on Nickel-Promoted Transition-Metal Sulfides That Catalyze Hydrogenation of Aromatic Compounds." *Angewandte Chemie International Edition* (2018).

Grundner, Sebastian, Wanqiu Luo, Maricruz Sanchez-Sanchez, and Johannes A. Lercher. "Synthesis of single-site copper catalysts for methane partial oxidation." *Chemical Communications* 52, no. 12 (2016): 2553-2556.

Oral presentations

Wanqiu Luo, Eva Schachtl, Oliver Y. Gutiérrez, Johannes A. Lercher, "Understanding the High Activity of Ni-Promoted WS₂ for Hydrogenation of Polyaromatic Compounds", at 25th North American Catalysis Society Meeting, Denver (CO), USA, 2017

Wanqiu Luo, Eva Schachtl, Hui Shi, Oliver Y. Gutiérrez, Johannes A. Lercher, "Understanding the high activity of Ni-promoted WS₂ for hydrogenation of polyaromatic compounds", at 13th European Congress on Catalysis - A Bridge to the future, Florence, Italy, 2017

Poster presentations

Luo, Wanqiu, Eva Schachtl, Oliver Y. Gutiérrez, and Johannes A. Lercher, "Impact of Ni on the Structure of WS₂/γ-Al₂O₃ and its Activity for Phenanthrene Hydrogenation", at The 16th International Congress on Catalysis, Beijing, China, 2016

Luo, Wanqiu, Eva Schachtl, Oliver Y. Gutiérrez, and Johannes A. Lercher, "Impact of Ni on the Structure of WS₂/γ-Al₂O₃ and its Activity for Phenanthrene Hydrogenation", at International Symposium on Molecular Aspects of Catalysis By Sulfides (MACS2016), Utrecht, Netherland, 2016